Betrouwbare persoonsgerichte draadloze communicatie
aan hoog datadebiet

Reliable High-Data Rate Body-Centric Wireless Communication

Thijs Castel

Promotoren: prof. dr. ir. H. Rogier, dr. ing. P. Van Torre
Proefschrift ingediend tot het behalen van de graad van
Doctor in de Ingenieurswetenschappen: Elektrotechniek

Vakgroep Informatietechnologie
Voorzitter: prof. dr. ir. D. De Zutter
Faculteit Ingenieurswetenschappen en Architectuur
Academiejaar 2015 - 2016

UNIVERSITEIT
GENT

ISBN 978-90-8578-906-2
NUR 959, 975
Wettelijk depot: D/2016/10.500/38

Reliable high-data rate body-centric wireless communication

Thijs Castel

Dissertation submitted to obtain the academic degree of
Doctor of Electrical Engineering

Publicly defended at Ghent University on June 22, 2016

Supervisor:
prof. dr. ir. H. Rogier
dr. ing. P. Van Torre
Electromagnetics group
Department of Information Technology
Faculty of Engineering and Architecture
Ghent University
Technologiepark Zwijnaarde 15
B-9052 Ghent, Belgium
http://emweb.intec.ugent.be

INTEC

UNIVERSITEIT GENT

Dankwoord

Toen Lionel Messi de beslissende goal maakte in de finale van de UEFA Champions League in 2011, was dit niet enkel te danken aan zijn talent, motivatie en werklust maar in grote mate aan de samenwerking van een volledig team. Gebruikmakend van deze analogie, kan ik het best beschrijven hoe ik erin slaagde een doctoraat te behalen aan de vakgroep Informatietechnologie van de Universiteit Gent. Dit doctoraatsboek is namelijk niet enkel mijn verdienste maar de verdienste van meerdere personen waarmee ik vaak, of minder vaak, samenwerkte. Deze personen zou ik hieronder, één voor één, oprecht willen bedanken.

Eerst en vooral zou ik de vakgroepvoorzitter Daniël De Zutter willen bedanken om mij de kans te geven vier jaar in de Elektromagnetismegroep van de vakgroep Informatietechnologie van de UGent te werken. Vier jaar werken in deze multiculturele omgeving brachten me de nodige verantwoordelijkheid, zelfstandigheid en teamspirit bij.

Eveneens wil ik mijn promotor Hendrik Rogier oprecht bedanken. Gedurende het eerste jaar van mijn doctoraat, waarin ik 5 mastervakken van de opleiding burgerlijk ingenieur diende te volgen, stond hij telkens klaar om mij te motiveren, te helpen of een hart onder de riem te steken om de nodige studiepunten te behalen. Overigens was hij, gedurende mijn volledige doctoraat, altijd bereid om mijn werk grondig te evalueren en zorgvuldig na te lezen om het naar een hoger niveau te brengen.

Hetzelfde gaat op voor mijn co-promotor Patrick Van Torre. Als bureaugenoot was hij telkenmale mijn eerste aanspreekpunt om resultaten, Matlabcode of paragrafen uit mijn artikels of doctoraatsboek kritisch te evalueren. Ook de niet werkgerelateerde gesprekken in de koffiehoek, een drink in het Geuzehuis na het behalen van de Best Student Paper award of een simpele lunch zorgden steeds voor de nodige ontspanning. Eveneens zal de recente EUCAP conferentie in Davos, waar ik voor het eerst tussen de bergen vertoefde samen met Patrick en *dottore* Luigi Vallozzi, me steeds bijblijven. Mede door het unieke Zwitsers horloge die we onszelf cadeau deden na de geslaagde presentaties.

Hoewel Isabelle Van der Elstraeten nu niet meer voor onze vakgroep werkt, wil ik haar toch bedanken om altijd zonder verpinken de, soms toch wel ingewikkelde, administratieve verplichtingen in goede banen te leiden.

Ook dient hier een speciale vermelding gemaakt worden van de waardevolle samenwerking en vriendschap met Sam Lemey. De voorbije acht jaar die we samen gespendeerd hebben, valt uiteindelijk niet in woorden te vatten. Maar de bloeiende liefde tussen hem en zijn toekomstige vrouw tijdens ons thesisjaar, het ontwikkelen van een unieke mix tussen technische kennis en praktische vaardigheden

en het, naar verwachting, succesvol behalen van zijn doctoraatsdiploma zijn absoluut zaken van Sam die mij altijd zullen bijblijven. De vakgroep zal er alle baat bij hebben om hem aan boord te houden.

Verder wil ik natuurlijk ook alle andere collegas bedanken. De combinatie van de oudere en jongere garde creëerde een unieke en leuke omgeving om dagelijks in te werken. Bedankt prof. Vande Ginste, Sam Agneessens, Paolo, Luigi, (barista) Marco, Zdravko, Simon, Giorgios, Michiel, Gert-Jan, Arne, Martijn, Steven, (bureauchef) Niels, Thomas, Irven, Dries, Robbe, Olivier, Steven, Sofian, Marijn, Véronique, Katia en Abdul. Wie deel uitmaakt van de oude(re) of jonge(re) garde laat ik aan hen over. Eveneens zou ik ook oud-collega's Eline, Freek, Bart, Mykola, Frederick, Arnout, Alessandro, Peter, Thomas, ... willen bedanken. Mijn excuses als ik iemand vergeet.

Het behalen van de hoogste academische graad zou uiteraard niet mogelijk zijn zonder de steun van een hechte familie. Hierbij wil ik eerst en vooral mijn ouders bedanken. Ze lieten mij, tijdens mijn studies, steeds de vrijheid om mijn academisch werk te combineren met sociale activiteiten zoals de Chiro, voetbal, minivoetbal... wat toch wel een moeilijke, maar geslaagde, combinatie bleek. Eveneens stonden ze steeds klaar wanneer het even niet meer zo vlot ging, zowel op sociaal vlak als tijdens de studies. Ook nadat mijn oudste zus Lien en ikzelf op amper drie maanden tijd allebei het ouderlijk nest verlieten om onze vleugels uit te slaan in het wijde Nieuwenhove, of Waregem, zijn we nog ten alle tijde hartelijk welkom om een babbeltje te slaan, een verjaardag te vieren, van een gezellige barbecue te genieten... Voor mij is deze hechte familieband zeer waardevol en daarom hoop ik dit altijd zo te kunnen houden. Dus mama en papa, bedankt voor alles.

Ook mijn beide zussen Ella en Lien zou ik hier graag willen bedanken. Het volwassen leven en de tijd die we samen doorbrachten in dezelfde leidingsploeg van de Chiro, bracht ons dichter bij elkaar. Naast zussen kan ik ze eigelijk ook gewoon als zeer goede vriendinnen beschouwen. Ook bedankt aan hun partners, Laurent en Frederik, die ik beide heel erg apprecieer.

Verder wil ik zeker ook Fanny en Johan, de ouders van mijn vriendin, bedanken voor de steun en appreciatie die ik reeds voelde vanaf de eerste dag die ik met Laura samen was, nu toch al bijna 8 jaar geleden. Ook bij, en met, hen is het steeds aangenaam vertoeven, zoals in Parijs vorig jaar of tijdens de gezellige vrijdagavonden als we bij hen komen dineren. Ook een speciale vermelding voor Laura's zus Jana en haar vriend Jasper, waarmee ik steeds onnozel kan doen, wat voor mij toch een uitstekende en noodzakelijke vorm van ontspanning is.

Naast mijn familie zou ik ook graag mijn vriendengroep, samengevat als de oudleiding van de Chiro, bedanken. De meeste onder ons kennen elkaar al meer dan 10 jaar wat tot een unieke, zeer ruime vriendenbende leidt, die zo ongeveer alles voor elkaar zou doen. Zelfs een vakantie met 14 van hen, wat voor buitenstaanders gedoemd was om tot ruzie te leiden, bleek één van de mooiste vakanties te worden. Mede dankzij onze unieke humor, het lachen met elkaar, is dit een ideale omgeving om in te ontspannen en echt te genieten. Hierbij zou ik ook graag Jonathan David, in Nieuwenhove omgedoopt tot Suske, bedanken. Sinds onze studies in Kortrijk en master thesis in Gent, zijn we steeds contact blijven houden. Als hij eens zes, of meer, weken in Verenigde Arabische Emiraten of Zuid-Korea vertoeft, is het altijd geestig om hem terug te zien.

Last but not least zou ik ook mijn vriendin Laura Desmet oprecht willen bedanken. Tijdens de 4 jaar van mijn doctoraat hebben we veel veranderingen doorgemaakt, van een huis huren tot een huis kopen, wat onze band sterker dan ooit maakte. Ondanks haar lange werkdagen, in combinatie met haar bijberoep als schoonheidsspecialiste, slaagde ze er toch in om altijd positief, opgewekt en levendig te blijven, wat ik heel erg apprecieer. Overigens heeft ze mij, ondanks het feit dat ik er bijna nooit over vertelde, gedurende mijn studies en doctoraat iedere dag, zonder uitzondering, blijven steunen. Eenvoudigweg zou ik kunnen stellen dat ik geluk heb met een vriendin als haar waarbij ik gewoon mezelf kan zijn. Bedankt bollie.

Gent, Juni 2016
Thijs Castel

You should never be the smartest person in the room. There's always going to be somebody who's smarter to learn from – and that's a good thing

JESSICA ALBA

Inhoudsopgave

Samenvatting

Draadloze persoonsgerichte communicatie wordt gedefinieerd als communicatie tussen kleine apparaten en sensoren die zich in, op of rond het menselijk lichaam bevinden. Dit type communicatie geeft aanleiding tot een groot aantal toepassingen in, onder andere, de gezondheidszorg, sport, computerspellen, veiligheid en beveiliging. Voorbeelden hiervan zijn de communicatie van foto's of videobeelden, genomen via een endoscopie pil in de darm van een patient, naar een monitor die zich naast het ziekenbed bevindt. Verder kan ook communicatie van biometrische- en omgevingsgegevens tussen reddingswerkers onderling, of tussen reddingswerkers en een basisstation, op die manier gerealiseerd worden. Bij de ontwikkeling van deze persoonsgerichte communicatiesystemen dienen de specifieke, fysische eigenschappen van het draadloze kanaal in rekening te worden gebracht. Signalen die draadloze communicatie opzetten tussen het menselijk lichaam en de buitenwereld ondervinden een grote verzwakking wanneer de elektromagnetische golven zich voortplanten door spieren, botten, vezels en bloed. Bovendien is het maximaal zendvermogen in het menselijk lichaam beperkt omwille van gezondheidsredenen. Daarom is het essentieel om belangrijke ontwerpparameters, zoals frequentie, bandbreedte en zendvermogen, zorgvuldig te kiezen. Bovendien beïnvloeden deze parameters ook de maximale capaciteit van de draadloze links. Hetzelfde geldt voor communicatie tussen twee personen onderling. De kwaliteit van de verbinding is hier sterk afhankelijk van de variërende posities, oriëntatie, afstand en lichaamshouding, welke multipad fading en schaduweffecten, ten gevolge van het menselijk lichaam, introduceren. Natuurlijk is er niet enkel nood aan kleine, draagbare toestellen die persoonsgerelateerde gegevens verzamelen, maar ook aan compacte antennes die deze persoonlijke data verzenden en ontvangen. Dit impliceert dat ook de antenne-topologie, de antenneposities, en het aantal antennes zorgvuldig moeten worden gekozen om de betrouwbaarheid van persoonsgerichte communicatie aan een hoog datadebiet te garanderen. Bij voorkeur wordt gebruik gemaakt van lichte, flexibele textielantennas waarop eventueel actieve elektronica kan worden geïntegreerd, om zo een compact systeem te realiseren. Het verzenden en ontvangen van gevoelige, persoonlijke informatie gebeurt best op een versleutelde manier, zodat de privacy kan bewaard worden. Aangezien er steeds meer gevoelige gebruikersinformatie wordt verzameld, door de groei van het aantal draagbare apparaten, is een goede beveiliging van draadloze links tussen verschillende personen essentieel. Daarom focussen we in dit werk niet enkel op betrouwbare persoonsgerichte communicatie aan hoog datadebiet maar ook op de beveiliging van deze draadloze communicatiekanalen.

In het eerste deel van dit proefschrift concentreren we ons op communicatie tussen een draadloze endoscopie pil en een draagbaar multi-antennesysteem, geschikt voor integratie in een jas die wordt gedragen door de patiënt. De eerder besproken ontwerpparameters worden zorgvuldig gekozen of berekend om een betrouwbare link aan hoog datadebiet te garanderen, vanaf iedere locatie in de darm van de patiënt. Op die manier kunnen foto's of video's worden doorgestuurd naar een specialist, ter ondersteuning van een grondige analyse van de gastro-intestinale gezondheid van de patiënt. Het menselijk lichaam wordt nagebootst door middel van een speciaal ontworpen bad, gevuld met een vloeistof die het menselijk spierweefsel simuleert. Deze experimentele configuratie komt overeen met het slechtst mogelijke scenario aangezien de samenstelling van het spierweefsel de grootste elektromagnetische verzwakking veroorzaakt. Om antennediversiteit te realiseren worden acht textielantennes aan het bad bevestigd. Deze ontvangen elk afzonderlijk de signalen, afkomstig van een kleine dipoolantenne in het bad. Daarna worden de ontvangen antennesignalen gecombineerd, op een constructieve manier, wat tot een hogere totale signaalsterkte leidt. Vervolgens wordt het minimaal aantal ontvangsantennes bepaald welke samen een voldoende hoge signaalsterkte garanderen om een draadloze videoverbinding te kunnen opzetten van een endoscopie capsule naar de monitor.

Persoongerichte communicatie tussen bewegende personen wordt uitgebreid besproken in het tweede deel van dit werk. Twee bewegende brandweermannen, uitgerust met meerdere textielantennes geïntegreerd in hun brandweerjas, bootsen een realistische interventie na in een kantoorgebouw. Tijdens dergelijke interventie is er één brandweerman die, direct na het betreden van het gebouw, de kantoren verkent op zoek naar eventuele slachtoffers terwijl de andere brandweerman simultaan de gang doorzoekt. Typisch aan dit soort interventies is dat beide brandweermannen gedurende de volledige reddingsactie in elkaars buurt blijven. Gedurende deze reddingsoperaties is de veiligheid van de brandweermannen prioritair. Daarom streven we naar betrouwbare breedbandige persoonsgerichte communicatie aan hoog datadebiet. Om het datadebiet op te drijven werden de brandweermannen uitgerust met meerdere zend-en ontvangstantennes, welke samen een Multiple Input Multiple Output (MIMO) antennesysteem vormen. Op die manier kunnen meedere onafhankelijke datastromen simultaan, en zonder interferentie, worden verzonden. Deze techniek, bekend als spatiale multiplexing, verhoogt het totaal aantal bits dat per seconde kan worden doorgestuurd. Verder wordt het breedbandig frequentieselectief kanaal opgesplitst in meerdere vlakke deelbanden, wat de kans op Intersymbool Interferentie (ISI) drastisch verlaagt. Dit impliceert dat meedere, onafhankelijke datastromen trager kunnen worden doorgestuurd over de verschillende deelbanden zonder dat opeenvolgende symbolen met elkaar interfereren. Aangezien er meerdere deelbanden beschikbaar zijn, zal het totale datadebiet vergroten door het implementeren van deze methode, genaamd Orthognal Frequency Division Multiplexing (OFDM). In het tweede deel van dit werk, met name in de Hoofdstukken 4 tot en met 7, beschouwen we dus MIMO-OFDM communicatiekanalen tussen twee bewegende brandweermannen.

In eerste instantie onderzoekt Hoofdstuk 4 of de bestaande *Long Term Evolution* (LTE) en, bij uitbreiding, de *LTE-Device to Device* (LTE-D2D) standaarden, kunnen gebruikt worden in breedbandige lichaamsgecentraliseerde netwerken die focusen op publieke veiligheid, een toepassing waarvoor ze oorspronkelijk niet werden ontwikkeld. Hoofdstuk 5 analyseert of de capaciteit van breedbandige lichaamsgecentraliseerde MIMO-OFDM communicatiekanalen tussen twee brandweermannen voldoende hoog is om, naast biometrische- en omgevingsgevens, ook camerabeelden te verzenden. Hierbij wordt een vergelijking gemaakt tussen Single Input Single Output (SISO)-, Single Input Multiple Output (SIMO)-, Multiple Input Single Output (MISO)- en MIMO-OFDM kanalen, waarbij maximaal twee zend-en ontvangsantennes worden beschouwd. Naast een vergelijking tussen een statisch en dynamisch meetscenario worden twee technieken besproken die de totale MIMO-OFDM capaciteit verder kunnen verhogen. De eerste techniek verdeelt het beschikbaar zendvermogen per subcarrier over beide MIMO-OFDM kanalen. Dit impliceert dat, per subcarrier, het sterkste MIMO-OFDM kanaal meer vermogen toegekend krijgt terwijl het zwakkere MIMO-OFDM kanaal vermogen inlevert. Het totaal zendvermogen per OFDM subcarrier, berekend als de som van de vermogens in beide MIMO-OFDM kanalen, blijft echter constant. De tweede techniek verdeelt het totaal beschikbaar zendvermogen dan weer terzelfdertijd optimaal over beide MIMO-OFDM kanalen en over alle deelbanden. Dit impliceert dat de sterke deelbanden van het sterkste MIMO-OFDM kanaal het meeste vermogen toegekend krijgen. Hoofdstuk 6 beschijft een derde techniek om de MIMO-OFDM capaciteit te verhogen. De modulatie per subcarrier kan gewijzigd worden naar gelang de ontvangen signaalsterkte. Indien de signaalsterkte groot is, kan de modulatie-orde worden verhoogd terwijl het aantal fout ontvangen bits beneden een vooropgestelde waarde blijft. Een grote modulatie-orde per subcarrier impliceert dat meer bits/symbolen worden doorgestuurd in die bepaalde deelband, waardoor de totale MIMO-OFDM capaciteit verhoogt. Verder beschrijft Hoofdstuk 7 een nieuw ontworpen antennerooster, bestaande uit vier antenne-elementen, dat spatiale- en polarisatiediversiteit combineert. Om de werking van het rooster te valideren werd een 1×4 SIMO verbinding opgezet tussen twee bewegende brandweermannen, waarbij één brandweerman een enkelvoudige textilelantenne droeg terwijl de antennerooster werd geïntegreerd in de rugsectie van de jas van een tweede brandweerman. Het voordeel van dit nieuwe kruisrooster is tweevoudig: de betrouwbaarheid van de MIMO-OFDM communicatielink verhoogt in combinatie met een verhoogd datadebiet, wanneer adaptieve subcarrier modulatie wordt geïmplementeerd.

Door de verdere ontwikkeling van draagbare apparaten en sensoren, die op het lichaam kunnen worden geplaatst, kunnen steeds meer mensen verbonden worden met het internet en op die manier persoonlijke gegevens communiceren met gewenste ontvangers. Naast het stijgend gemak en comfort voor de mensen zelf, brengen deze nieuwe draadloze persoonsgerichte netwerken ook de noodzaak van sterke encryptie-algoritmes met zich mee. Niemand wil namelijk dat deze persoonlijke gegevens onderschept worden tijdens de draadloze overdracht en op die manier in handen komen van ongewenste personen of openbaar worden gemaakt. Eveneens mogen deze beveiligingsalgoritmes niet veel energie verbruiken om de batterijgevoede draagbare apparaten een zo groot mogelijke autonomie te bezorgen. In plaats van bestaande batterijverslindende technieken aan de hand van Pseudo-Noise sequenties kan het unieke, reciproke communicatiekanaal tussen twee legitieme personen, Alice en Bob, benut worden om gezamenlijke willekeur tussen beide te genereren. Als Alice een pakket stuurt naar Bob en Bob op zijn beurt een pakket terugstuurt naar Alice, binnen de coherentietijd van het draadloze kanaal, dan zal de ontvangen signaalsterkte aan beide zijden ongeveer gelijk zijn. Stel nu dat een indringer, Eve, het communicatiekanaal afluistert en dat zij op haar beurt de ontvangen signaalsterktes berekent van de door haar ontvangen pakketten, afkomstig van Alice of Bob. Dan zullen deze deze waardes totaal verschillend zijn van de ontvangen signaalsterktes bij Alice en Bob. De appendix beschrijft een praktische toepassing van dit nieuwe encryptie-algoritme. Autonome nodes werden op het menselijk lichaam geplaatst om geheime sleutels te genereren, op basis van de ontvangen signaalsterktes, tussen twee bewegende legitieme partijen bij aanwezigheid van een stationaire indringer. De sequenties van ontvangen signaalsterktes werden aan de hand van correlatie, mutuele informatie en entropie geanalyzeerd en geschikt bevonden om te gebruiken in indoor en outdoor draadloze persoonsgerichte netwerken.

Summary

Wireless body-centric communication is defined as communication between small devices and sensors located in, on or around the human body. This type of communication gives rise to a large number of applications in, among others, healthcare, sports, gaming, safety and security. For example, pictures or videos, taken by an endoscopy capsule in the patient's bowel, may be wirelessly transmitted to a monitor located near the hospital bed. Also the communication of biometrical- and environmental data between rescue workers, or between a rescue workers and a command post, is defined as body-centric communication. When developing this kind of communication systems, the specific physical characteristics of the body-centric radiowave channel should be taken into account. Signals setting up a wireless communication link from inside the human body to the outside world, or vice versa, experience a large attenuation when the electromagnetic waves propagate through muscles, bones, vessels and blood. Moreover, safety precautions impose stringent requirements on the maximum transmit power inside the human body. Therefore, it is essential to carefully choose important design parameters such as frequency, bandwidth and transmit power. Next to the channel quality, also the channel capacity of wireless links heavily depends on these design parameters. The same holds for person-to-person communication. In this body-to-body scenario, the quality of the wireless link heavily depends on varying positions and body postures and on mutual orientation and distance. In addition to the environment, the aforementioned parameters influence multipath fading and shadowing effects due to the human body. Next to the small, wearable, data-gathering devices, compact antennas are indispensable to transmit and receive these personal user data. This implies that also the antenna topology, the antenna positions and the number of antennas should be chosen carefully to guarantee reliable, high-data rate body-centric communication. Preferably, lightweight flexible textile antennas are used on which active electronics can be integrated, realizing a compact system. Because the user's privacy is a major concern in body-centric communication networks, sensitive, personal information should be encrypted when transmitted over the wireless channel. Given that more and more user data are gathered, due to the increasing number of wearable devices, the security of wireless links between multiple persons is essential. Therefore, in this work, we focus on reliable and possibly encrypted high-data rate body-centric wireless communication. ante In the first part of this dissertation, we concentrate on communication between a wireless endoscopy pill and a wearable multi-antenna system, suitable for integration inside a jacket, worn by the patient. The design parameters, as described earlier, are carefully chosen or calculated to guarantee a reliable, high-data rate communication link, from anywhere inside the patient's bowel towards the multi-antenna system. This enables wireless communication of photos, or videos, towards a specialist, enabling a thorough analysis of the gastro-intestinal condition of the patient. The human body is mimicked by a specially designed bath, filled with muscle-mimicking tissue. This experimental setup corresponds to the worst-case scenario since the composition of the muscle tissue causes the largest electromagnetic attenuation. By fixing eight textile antennas on the sidewalls or bottom of the bath, antenna diversity is realized. These antennas receive, each individually, the signals from a small dipole antenna inside the bath. Then, all received antenna signals are combined constructively, leading to a higher total signal strength. Subsequently, the minimum number of receive antennas is determined that still guarantees a sufficiently high signal strength to set up a video link from the wireless endoscopy capsule to a monitor.

Body-centric communication between moving persons is extensively described in the second part of the work. Two dynamic firefighters, equipped with multiple textile antennas integrated inside their jacket, replicate a realistic intervention in an indoor office environment. During such interventions, the first firefighter starts scanning the offices while the second firefighter simultaneously starts scanning the hallway. Typically, both firemen stay in each other's proximity during the entire rescue operation. During such interventions, the safety of the firemen is the top priority. Therefore, we strive for reliable, wideband, high-data rate body centric communication. To increase the data rate, the firemen were equipped with multiple transmit and receive antennas, creating a Multiple Input Multiple Output (MIMO) system. This allows simultaneous transmission of multiple, independent data streams without interference. This technique, widely known as spatial multiplexing, increases the total number of bits per seconds that can be transmitted. The wideband frequency-selective channel is divided into multiple frequency-flat subcarriers, drastically decreasing the probability of Inter Symbol Interference (ISI). This implies that multiple, independent data streams could be sent, at a lower transmit rate, over different subcarriers, without interference between consecutive symbols. Given that multiple subcarriers are available, this method, called Orthogonal Frequency Division Multiplexing (OFDM), increases the total data rate. Hence, in the second part of this dissertation, comprising Chapter 4 up to 7, we consider MIMO-OFDM communication channels between moving firefighters.

First, Chapter 4 describes, in general terms, whether the existing Long Term Evolution (LTE) and, by extension, the LTE-Device to Device (LTE-D2D) standards, are suitable for wideband body-centric communication networks, focusing on public safety, a purpose for which they were originally not designed. Chapter 5 analyzes whether the capacity of wideband body-centric MIMO-OFDM communication channels between two firefighters is sufficiently high to guarantee, next to the biometrical- and environmental data, reliable and efficient transmission of camera images. Therefore, we have compared Single Input Single Output (SISO)-, Single Input Multiple Output (SIMO)-, Multiple Input Single Output (MISO) and MIMO-OFDM channels, considering maximum two transmit and two receive antennas. In addition to comparing a static and dynamic measurement scenario, two capacity enhancement techniques are described that could further increase the total

MIMO-OFDM capacity. The first technique distributes the available transmit power per subcarrier over both MIMO-OFDM channels. This implies that, on a subcarrier basis, more power is allocated to the strongest MIMO-OFDM channel while the weaker MIMO-OFDM channel has to sacrifice some of its power. The total power of each OFDM subcarrier, calculated as the sum of the subcarrier power in both MIMO-OFDM channels, remains constant. In addition, the second technique distributes the total available transmit power optimally over both MIMO-OFDM channels and all subcarriers simultaneously. This implies that most power is allocated to the strongest subcarriers of the strongest MIMO-OFDM channels. Chapter 6 describes a third technique to further enhance the MIMO-OFDM throughput. The modulation per subcarrier can be adapted, depending on the received signal strength on that subcarrier. When the signal strength increases, the modulation order can be increased while the number of errors remains below a preset value. A higher modulation order per subcarrier ensures a higher throughput on the specific subcarrier, which increases the total MIMO-OFDM capacity. Chapter 7 further describes a novel, four-element antenna array, which combines spatial and polarization diversity. The antenna array's performance is validated by setting up a 1×4 SIMO link between dynamic firefighters, where one firefighter was equipped with a single textile antenna while the novel antenna array was integrated in the back section of the second firefighter's jacket. The benefit of the cross array is twofold: the reliability of the MIMO-OFDM communication channel is increased in combination with throughput gain, when applying adaptive subcarrier modulation.

Given the further development of wearable devices and sensors, which can be deployed on the human body, more people can be connected to the Internet and wirelessly transfer personal information between desired recipients. Besides increased users convenience and comfort, these new personalized wireless networks also introduce the need for strong encryption algorithms, since nobody wants that personal user data can be intercepted during wireless transmission and, hence, fall into hands of undesired recipients. Moreover, to guarantee sufficient autonomy, these encryption algorithms cannot consume a lot of energy of the battery-operating wearable devices. Instead of existing battery-draining techniques that rely on Pseudo-Noise sequences, the unique, reciprocal communication channel between the two legitimate parties, Alice and Bob, is used to generate joint randomness between them. If Alice sends a packet towards Bob and Bob retransmits a packet back to Alice, within the coherence time of the wireless channel, the received signal strength at both sides of the body-to-body channel will be approximately equal. Assume that an intruder, Eve, monitors the communication channel and is able to calculate the received signal strengths of the packets sent by Alice towards Bob, or vice versa. Then, the received signal strength values at Eve will be totally different from the received signal strengths at Alice and Bob. The appendix describes a practical application of this new encryption algorithm. Autonomous nodes were placed upon the human body to generate the secret keys, based on the received signal strengths between two dynamic legitimate parties in the presence of a stationary eavesdropper. The sequences of received signal strengths are

analyzed in terms of the correlation, mutual information and entropy. They are proven suitable for use in indoor and outdoor wireless boy-centric networks

List of Abbreviations

AWGN	Additive White Gaussian Noise
BER	Bit Error Rate
CDF	Cumulative Distribution Function
CIR	Channel Impulse Response
CMOS	Complementary Metal Oxide Semiconductor
CP	Cyclic Prefix
CSI	Channel State Information
D2D	Device to Device
EIRP	Equivalent Isotropically Radiated Power
ETSI	European Telecommunications Standards Institute
FBRT	Front to Back Ratio
FCC	Federal Communication Commission
FSPL	Free Space Path Loss
GI	Gastrointestinal
GPS	Global Positioning System
IC	Integrated Circuit
IEC	International Electrotechnical Commission
IEEE	Institute of Electrical and Electronics Engineers
IoP	Internet of People
IoT	Internet of Things
ISI	Intersymbol Interference
ISM	Industrial, Scientific and Medical Band
LCR	Level Crossing Rate
LoS	Line of Sight
LSB	Least Significant Bit
LTE	Long Term Evolution
MB	Multiband
MI	Mutual Information
MICS	Medical Implant Communication Service
MIMO	Multiple-Input Multiple-Output
MISO	Multiple-Input Single-Output
MRC	Maximal Ratio Combining
MSB	Most Significant Bit
NLoS	Non Line of Sight
OFDM	Orthogonal Frequency Division Multiplexing
PCB	Printed Circuit Bord
PDP	Power Delay Profile

PN	Pseudo-Random Noise
QAM	Quadrature Amplitude Modulation
RF	Radio Frequency
RIT	Rapid Intervention Team
RMS	Root Mean Square
RSS	Received Signal Stength
RX	Receiver
SAR	Specific Absorption Rate
SC	Selection Combining
SIMO	Single-Input Multiple-Output
SISO	Single-Input Single-Output
SIW	Substrate Integrated Waveguide
SNR	Signal to Noise Ratio
STC	Space-Time Codes
SVD	Singular Value Decomposition
TX	Transmitter
UE	User Equipment
UWB	Ultra-Wideband
WBAN	Wireless Body Area Networks
WCE	Wireless Capsule Endoscopy

List of Symbols

$\lvert \cdot \rvert$	Magnitude of a complex or real number
$.^{*}$	Complex conjugate
$.^{T}$	Transpose
$.^{H}$	Hermitian conjugate
$\mathrm{P}(\cdot)$	Probability
$\mathrm{E}(\cdot)$	Expected value
$\mathrm{H}(\cdot)$	Entropy
$\mathrm{MI}(\cdot\,,\cdot)$	Mutual Information
bps/Hz	Bits per second per Hertz
dB	Decibel
dBm	Decibel-milliwatt
dBi	Decibel-isotropic
Hz	Hertz
W	Watt
ϵ	Permittivity of a medium
ϵ_r	Relative permittivity
λ	Wavelength[1]
Ω	Ohm
σ	Conductivity
$tan\ \delta$	Loss tangent
f	Frequency
S_{11}	One-port S-parameter
$\boldsymbol{\Sigma}$	Singular matrix
σ	Singular value
γ	Instantaneous SNR
κ	Condition number
λ	Eigenvalue[2]
ρ	Envelope correlation
Δf	Subcarrier bandwidth
σ^2	Noise power
$\bar{\tau}$	Mean delay
τ_{RMS}	RMS delay spread
τ_{excess}	Excess delay
τ_{ℓ}	Delay of multipath ℓ
ν	Frequency variable of the low-pass channel trasfer function

B	Bandwidth
$B_{C,0.5}$	50% correlation bandwidth
C	Channel capacity
d_{min}	Mininal distance between constellation points
G	Capacity gain
h	Channel coefficients
$\mathbf{H}$	Channel matrix
M	Rank of the singular matrix[1]
M	Number of constellation points[2]
n	Additive White Gaussian Noise
N_{RX}	Number of receive antennas
N_{TX}	Number of transmit antennas
O_v	Overhead
$P_h(\tau)$	Power delay profile
P_ℓ	Power of multipath ℓ
PR	Power ratio
Q	Q-function
R_b	Bitrate
$R_T(\Delta f)$	Frequency correlation function
T_s	Symbol time

List of Publications

Articles in International Journals

- T. Castel, P. Van Torre, E. Tanghe, S. Agneessens, G. Vermeeren, W. Joseph and H. Rogier, “Improved Reception of In-Body Signals by Means of a Wearable Multi-Antenna System“, *International Journal of Antennas and Propagation*, vol. 2013, Article ID 328375, 9 pages, 2013.
- T. Castel, P. Van Torre, L. Vallozzi, M. Marinova, S. Lemey, W. Joseph, C. Oestges and H. Rogier, “Capacity of Broadband Body-to-Body Channels between Firefighters wearing Textile SIW Antennes“, *Accepted for IEEE Transactions on Antennas & Propagation (TAP)*, vol. 64, no. 05.
- T. Castel, S. Lemey, P. Van Torre, C. Oestges and H. Rogier, “Four-element Ultra-Wideband Textile Cross Array for Dual Spatial and Dual Polarization Diversity“, *Accepted for IEEE Antennas and Wireless Propagation Letters (AWPL)*.
- S. Lemey, T. Castel, P. Van Torre, T. Vervust, J. Vanfleteren, P. Demeester, D. Vande Ginste and H. Rogier, “Threefold Rotationally Symmetric SIW Antenna Array for Ultra-Short-Range MIMO Communication“, *Accepted for IEEE Transactions on Antennas & Propagation (TAP)*, vol. 64, no. 05.

Articles in Conference Proceedings

- T. Castel, S. Lemey, S. Agneessens, P. Van Torre, H. Rogier and C. Oestges, “Reliable communication between rescuers during interventions using textile antenna systems“, in *Computer Aided Modelling and Design of Communication Links and Networks (CAMAD), 2015 IEEE 20th International Workshop on*, Sept. 2015, pp. 135–139, Guildford, UK.
- T. Castel, S. Lemey, S. Agneessens, P. Van Torre, H. Rogier and C. Oestges, “LTE as a potential standard for public safety indoor body-to-body networks“, in *Communications and Vehicular Technology in the Benelux (SCVT), 2015 IEEE Symposium on*, Nov. 2015, pp. 1–6, Luxembourg City, Luxembourg.
- T. Castel, S. Lemey, S. Agneessens, P. Van Torre, H. Rogier and C. Oestges, “Adaptive Subcarrier Modulation for Indoor Public Safety Body-to-Body Networks“, Accepted for the *10th European Conference on Antennas and Propagation (EuCAP)*, Apr. 2016, Davos, Switzerland.

- T. Castel, P. Van Torre and H. Rogier, “RSS-Based Secret Key Generation for Indoor and Outdoor WBANs using On-Body Sensor Nodes“, Accepted for the *International Military Communications and Information Systems Conference (ICMCIS)*, May 2016, Brussels, Belgium.
- S. Agneessens, T. Castel, P. Van Torre, E. Tanghe, G. Vermeeren, W. Joseph and H. Rogier, “A wearable repeater relay system for interactive real-time wireless capsule endoscopy“, in *Antennas & Propagation (ISAP), 2013 Proceedings of the International Symposium on*, Oct. 2013, pp. 617–620, Nanjing, China.
- H. Rogier, S. Agneessens, T. Castel, S. Lemey, F. Declercq, P. Vanveerdeghem, P. Van Torre, L. Vallozzi and W. Joseph, “Novel wearable antenna systems for high datarate mobile communication in healthcare“, in *Wireless Mobile Communication and Healthcare (Mobihealth), 2014 EAI 4th International Conference on*, Nov. 2014, pp. 188–191, Athens, Greece.
- P. Van Torre, T. Castel and H. Rogier, “Realistic performance measurement for body-centric spatial modulation links“, in *9th European Conference on Antennas and Propagation (EuCAP)*, Apr. 2015, pp. 1–5. Lisbon, Portugal.
- P. Van Torre, T. Castel and H. Rogier, “Encrypted Body-to-Body Wireless Sensor Node Employing Channel-State-Based Key Generation“, Accepted for the *10^{th} European Conference on Antennas and Propagation (EuCAP)*, Apr. 2016, Davos, Switzerland.

Awards

- Best Student Paper Award at the 22nd IEEE Symposium on Communications and Vehicular Technology in The Benelux (IEEE SCVT 2015) with the paper “LTE as a potential standard for public safety indoor body-to-body networks“.

Reliable high-data rate body-centric wireless communication

1
Introduction

1.1 Context

Starting half a century ago, miniaturization of Integrated Circuits (IC's) and electronic components have recently led to the rise of wearables, being small, electronic devices and sensors, which are worn on the human body. Moreover, by further reducing the size of these data-collecting sensors, even smaller in-body devices were designed, such as a camera pill which can be swallowed by a patient or even injectable radios of only 10 cubic millimeters. Additionally, private, personal data can be effectively communicated through compact on-body antennas, potentially invisibly integrated into the user's clothing, or through in-body antennas, such as small dipoles for Wireless Capsule Endoscopy (WCE). With the emergence of all these body-centric devices and antennas, the term "body-centric communication" was introduced. Generally, body-centric communication is defined as communication in-and around the human body. This term combines four different communication scenarios. First, *in-body communication* involves communication from inside the body towards a base station, located in the close proximity of the human body, or vice versa. Applications for in-body communication are mainly in healthcare, such as wireless transmission of high-resolution pictures, taken by an in-body camera pill, towards a fixed monitor, observed by a doctor. Second, *off-body communication* comprises communication from on-body devices towards a fixed base station. For example, GPS data from football players, gathered using an on-body GPS tracker, is wirelessly sent towards a fixed computer at the side-line of the pitch. Third, *on-body communication* is defined as communication between wearable devices on the same person, such as a heart rate monitor and a wrist watch. The transmitter, worn on the chest, sends the heart rate data towards a sport watch, worn by the user. Finally, live video streaming between two on-duty firefighters is defined as *body-to-body communication*, since two on-body devices, worn by different persons, communicate. As body-centric communication introduces a large number of potential interesting applications, this dissertation focuses on two specific scenarios: in-body communication between an endoscopy capsule and a wearable multi-antenna system, and body-to-body communication between two on-duty rescue workers.

1.2 Motivation

In healthcare and rescue operations, reliable communication of personal user data can mean the difference between life and death. Imagine that communication with a disoriented firefighter is lost, while the firefighter is trapped in a burning building. Or assume that the blood pressure and blood glucose values of patients with diabetes are communicated incorrectly, misleading a doctor to detect dangerous patient conditions. These worst-case scenarios should be avoided anywhere, at any time, demonstrating the importance of reliability in body-centric communication. Additionally, by increasing the capacity and, hence, data rate of these body-centric wireless communication channels, patients' or rescue workers' conditions could be better interpreted and evaluated. For example, when combining low-data rate sensor data with high-data rate pictures and/or videos, the rescue workers' safety and situational awareness may be increased, which decreases the number of casualties or deaths. Furthermore, when wirelessly communicating biometrical data, gathered by wearable on-body devices, an encryption algorithm has to avoid that third parties intercept personal user data. Hence, a reliable, low-power and computationally simple encryption algorithm, programmed on the on-body hardware, is essential for future Wireless Body Area Networks (WBANs). In summary, body-centric communication has to be reliable, supporting high data rates, in combination with a low-power, simple encryption algorithm. Therefore, this dissertation focuses on reliable and possibly encrypted high data-rate body-centric wireless communication.

1.3 Current state of the art

The emergence of actively controlled wireless endoscopy capsules allows specialists to steer camera pills to the specific region of interest. To fully exploit the benefits of these camera pills, being the opportunity of live video streaming, in-body communication standards should not only support low-data rate communication but also high-data rate in-to-out body communication, or vice versa. Therefore, current channel modelling, characterization or simulations [1]–[7] should be supplemented with real-life measurement campaigns. The same holds for indoor safety networks. Current narrowband public safety networks, such as TETRA, allow voice communication between firefighters or between a firefighter and a base station. Of course, this is already a great improvement over analog radios, since encryption and diversity techniques may now be implemented. However, the next logical step is to evolve from low-data rate communication, such as voice or GPS, towards high-data rate communication. By guaranteeing a high-capacity body-to-body link, on-duty firefighters may communicate real-time information such as sensor and environmental data, or even pictures and/or videos. Yet, earlier work on body-to-body communication focused mainly on statistical characterization or receiver diversity [8]–[10]. Moreover, when calculating capacity in body-to-body networks [11], the users' stringent requirements in terms of wearability and comfort, should be a major design concern. Additionally, further research into capacity enhancement techniques for wideband body-to-body networks would be very useful. Up to now, the encryption of such body-to-body links is implemented based on a computationally complex setup using a Pseudo-Noise (PN) generator. By combining the personal data with this PN sequence, which is only known at the two legitimate parties, a secure link can be guaranteed. However, generating a high-entropy PN sequence, unknown to a potential eavesdropper, is computationally complex and, hence, power consuming when implemented on battery limited wearable devices. Therefore, a better alternative for encryption algorithms in WBANs should be developed, focusing on the combination of low power and low computational complexity, as theoretically described in [12]–[14]. However, practical measurements, with autonomous on-body devices, should be performed to verify if this low-power, low-computational complex algorithm would be suitable for the encryption in future WBANs.

1.4 Own contributions

In this thesis, we have focused on *practical implementations* of multi-antenna systems for body-centric communication networks. Moreover, we have carefully replicated *real-life scenarios* for both the *in-body* as *body-to-body* communication channels.

As we focus on reliable and high-data rate in-body communication, we propose the Industrial, Scientific and Medical (ISM) band as a better alternative to both the Medical Implant Communication Service (MICS) and Ultra-Wideband (UWB) band. On the one hand, the ISM band provides a higher bandwidth compared to the MICS band and, on the other hand, experiences less in-body signal attenuation than the transmit power restricted UWB band. Moreover, commonly used high-speed wireless communication standards are commonly implemented in IC's operating in this ISM band. Furthermore, we have determined the minimum number of wearable on-body textile antennas, in the worst case scenario, necessary for reliable and high-data rate in-body communication. The worst case scenario was replicated by filling a standardized phantom with muscle-tissue-simulating liquid, yielding the largest signal attenuation in the ISM band.

Our analysis of wideband, indoor body-to-body communications could be of great importance for the future development and standardization of indoor public safety networks. By means of channel sounder experiments, accurately replicating a real indoor firefighter intervention, detailed wideband body-to-body channel information is analyzed and interpreted. Four cavity-backed slot textile antennas, implemented in Substrate Integrated Waveguide (SIW) technology, were unobtrusively deployed in the firefighters' jackets, providing up to 2×2 Multiple Input Multiple Output (MIMO) communication. Additionally, Orthogonal Frequency Division Multiplexing (OFDM) is implemented, dividing the wideband channel into multiple narrowband subcarriers. The wideband body-to-body MIMO-OFDM channels, between two dynamic firefighters in each other's proximity, are analyzed into great detail in terms of standardization, capacity analysis, capacity enhancement techniques and receiver diversity gain.

Up to now, the main deficiency of wearables is the device's limited battery life. Since the autonomy of these on-body devices has to be maximized, unnecessary energy consumption should be avoided. This implies that, applied to the security of body-to-body link, wearables should contain a low-power Pseudo-Noise (PN) sequence generator with low computational complexity. Therefore, we propose to not implement existing, power draining PN generators on wearable devices but to use the unique body-to-body channel between two communicating parties to generate this PN sequence. The Received Signal Strengths (RSSs) at two legitimate parties are highly correlated, due to reciprocity, if the round-trip-time of the systems is much below the coherence time of the body-to-body channel. However, the RSS at an intruder/eavesdropper is expected to be virtually uncorrelated. Therefore, in the appendix, we propose an algorithm that extracts equal secret keys at Alice and Bob, based on their correlated RSS streams, but unknown to an eavesdropper Eve. This low-power, low-computational complex, RSS-based algorithm is validated for encryption of indoor and outdoor body-to-body links between two legitimate mobile users.

1.5 Outline

In Chapter 2, some typical phenomena of wideband indoor communication channels are explained. We briefly focus on three concepts that are frequently used in the remainder of this book: multipath propagation, receiver diversity and OFDM.

Part I describes a practical implementation of a narrowband in-to-out body communication link. The minimal number of on-body RX antennas is determined to guarantee a sufficiently high Signal to Noise Ratio (SNR) for live video streaming from anywhere in the patient's bowel. From a practical point of view, patients could be monitored by integrating the low-profile on-body textile antennas, coherently combining signals through Maximal Ratio Combining (MRC), into a comfortable jacket.

In Part II, comprising Chapters 4 up to 7, we focus on the standardization, capacity analysis, capacity enhancement techniques and receiver diversity gain of wideband, indoor body-to-body channels. In Chapter 4, the Long Term Evolution (LTE) standard is proven very suitable for indoor public safety networks, a purpose for which it was not originally designed. The first part of Chapter 5 presents the capacity of wideband, indoor body-to-body MIMO channels for static and dynamic measurement scenarios. Additionally, capacity enhancement techniques, such as one- and two-dimensional waterfilling or Adaptive Subcarrier modulation are presented in the second parts of Chapters 5 and 6, respectively. Furthermore, the design of an ultra-wideband dual spatial, dual polarization antenna array, developed for operation in the low duty-cycle restricted [3.4-4.8] GHz band is presented in Chapter 7. Additionally, the cross array is proven very suitable to further increase reliability, in combination with an increased throughput, of SIMO wideband body-to-body links.

Indoor and outdoor narrowband body-to-body measurements between two legitimate parties, in the presence of a static eavesdropper, are presented in the appendix. Autonomous on-body textile sensors nodes are placed on all three parties to collect the RSS values within the theoretic coherence time of the body-to-body channels. Based on mutual information, entropy and correlation of the collected RSS streams, a low-power, low-computational complex algorithm is validated for the encryption of future WBANs.

References

[1] A. Khaleghi and I. Balasingham, “Improving in-body ultra wideband communication using near-field coupling of the implanted antenna”, *Microwave and Optical Technology Letters*, vol. 51, no. 3, pp. 585–589, Mar. 2009.

[2] A. Khaleghi, R. Chavez-Santiago, X. Liang, I. Balasingham, V. C. M. Leung, and T. A. Ramstad, “On ultra wideband channel modeling for in-body communications”, in *Proceedings of the 5th International Symposium on Wireless Pervasive Computing*, Modena, Italy: IEEE, May 2010, pp. 140–145.

[3] S. Stoa, R. Chavez-Santiago, and I. Balasingham, “An ultra wideband communication channel model for capsule endoscopy”, in *Proceedings of the 3rd International Symposium on Applied Sciences in Biomedical and Communication Technologies (ISABEL)*, Rome, Italy: IEEE, Nov. 2010, pp. 1–5.

[4] J. Wang and Q. Wang, “Channel modeling and BER performance of an implant UWB body area link”, in *Proceedings of the 2nd International Symposium on Applied Sciences in Biomedical and Communication Technologies (ISABEL)*, Bratislava, Slovakia: IEEE, Nov. 2009, pp. 1–4.

[5] A. Ghildiyal, K. Amara, R. D. Molin, B. Godara, A. Amara, and R. K. Shevgaonkar, “UWB for in-body medical implants: A viable option”, in *Proceedings of the IEEE International Conference on Ultra-Wideband (ICUWB)*, vol. 2, Nanjing, China: IEEE, Sep. 2010, pp. 1–4.

[6] J. Shi and J. Wang, “Channel characterization and diversity feasibility for in-body to on-body communication using low-band UWB signals”, in *Proceedings of the 3rd International Symposium on Applied Sciences in Biomedical and Communication Technologies (ISABEL)*, Rome, Italy: IEEE, Nov. 2010, pp. 1–4.

[7] J. Shi, D. Anzai, and J. Wang, “Diversity performance of UWB low band communication over in-body to on-body propagation channel”, in *Proceedings of the 6th European Conference on Antennas and Propagation (EUCAP)*, Prague, Czech Republic: IEEE, Mar. 2012, pp. 535–539.

[8] Q. Abbasi, A. Sani, A. Alomainy, and Y. Hao, “On-body radio channel characterization and system-level modeling for multiband OFDM ultra-wideband body-centric wireless network”, *IEEE Transactions on Microwave Theory Techniques*, vol. 58, no. 12, pp. 3485–3492, Dec. 2010.

[9] R. Rosini, R. Verdone, and R. D’Errico, “Body-to-body indoor channel modeling at 2.45 GHz”, *IEEE Transactions on Antennas and Propagation*, vol. 62, no. 11, pp. 5807–5819, Nov. 2014.

[10] Q. Wang, K. Masami, and J. Wang, "Channel modeling and BER performance for wearable and implant UWB body area links on chest", in *Proceedings of the International Conference on Ultra-Wideband (ICUWB)*, Vancouver, Canada: IEEE, Sep. 2009, pp. 316–320.

[11] K. Ghanem, "Effect of channel correlation and path loss on average channel capacity of body-to-body systems", *IEEE Transactions on Antennas and Propagation*, vol. 61, no. 12, pp. 6260–6265, Dec. 2013.

[12] J. Miranda, N. Makitalo, J. Garcia-Alonso, J. Berrocal, T. Mikkonen, C. Canal, and J. Murillo, "From the internet of things to the internet of people", *Internet Computing, IEEE*, vol. 19, no. 2, pp. 40–47, Mar. 2015.

[13] T. Vilarinho, B. Farshchian, J. Floch, and B. Mathisen, "A communication framework for the internet of people and things based on the concept of activity feeds in social computing", in *9th International Conference on Intelligent Environments (IE)*, Jul. 2013, pp. 1–8.

[14] J. Wei, "How wearables intersect with the cloud and the internet of things : considerations for the developers of wearables", *Consumer Electronics Magazine, IEEE*, vol. 3, no. 3, pp. 53–56, Jul. 2014.

2

Body-centric communication

2.1 Multipath propagation

Indoor body-centric communication experiences a large influence from multiple delayed copies of the signal, travelling along different paths between transmitter and receiver, defined as multipath propagation [1]. This phenomenon is visualized in Fig. 2.1 for one direct and three reflected paths. The multiple copies of the transmitted pulse interfere constructively or destructively at the receiver and introduce fading effects. For further analysis, the (simplified) two-ray model is considered, involving one direct and one reflected path between transmitter and receiver.

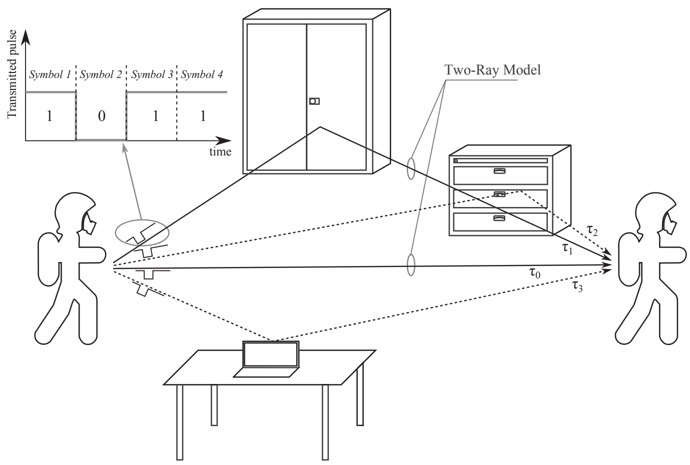

Figure 2.1: Multipath propagation in indoor environments

If the maximum delay of the reflected path, further defined as τ instead of τ_1, is much smaller than the symbol time T_S, copies of the same symbols received along multiple paths remain synchronized, as shown in Fig. 2.2.a. Yet, if $\tau > T_S$, symbol n of the reflected path could interfere with, for example, symbol n+1 of the direct path, introducing Inter Symbol Interference (ISI) [2].

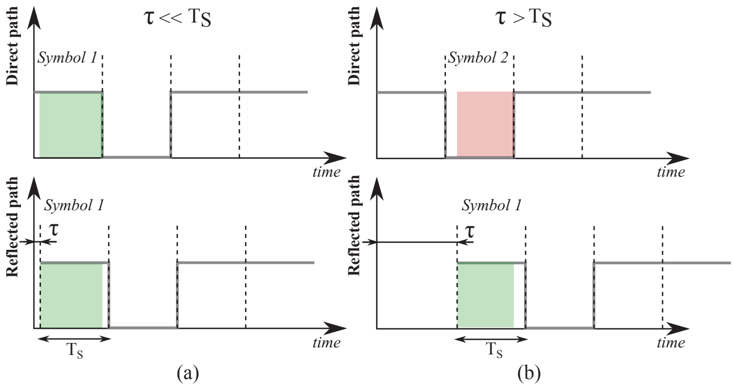

Figure 2.2: Analysis of the two-ray model for small and large delays

Even when $\tau << T_S$, being in case of flat fading, the quality of the wireless link may deteriorate due to the propagation conditions. When both symbols of the direct and reflected path add up destructively, because they are out of phase, the Received Signal Strength (RSS) drops drammaticaly, causing a (deep) fading dip. Additionally, shadowing can further degrade the average RSS strength if an object blocks the direct path between the transmitter and receiver. Moreover, when focusing on body-centric wireless communication, the human body can block the path between a transmitter and an on-body RX antenna, introducing body shadowing effects.

2.2 Diversity

When only considering one receive antenna and one transmit antenna, the combination of fading and (body) shadowing could cause temporary signal loss at the receiver, making reliable communication impossible. However, when employing multiple (on-body) receive antennas, it is likely that, when the signal at one RX antenna experiences deep fading, the signal strength at the other receive antenna remains sufficiently high for reliable communication, as seen in Fig. 2.3 at time instance t = 1s. Therefore, receiver diversity can drastically increase reliability, through diversity gain [3], if the signals at multiple receive antennas are sufficiently decorrelated. The envelope correlation coefficient ρ, preferably well below 0.7 to exploit diversity gain, is calculated as:

$$\rho = \frac{E(\mathbf{X}\cdot\mathbf{Y}) - E(\mathbf{X})E(\mathbf{Y})}{\sqrt{\left[E(\mathbf{X}^2) - (E(\mathbf{X}))^2\right]\left[E(\mathbf{Y}^2) - (E(\mathbf{Y}))^2\right]}}. \tag{2.1}$$

Decorrelation can be ensured by spatial and/or polarization diversity [4]–[6], as also described in Chapter 7. As an example, when implementing Selection Combining (SC) at the receiver, the total received Signal-to-Noise Ratio (SNR) is equal to the highest SNR selected from all receive antennas at any give time instance, as visualized on Fig. 2.3 for two receive antennas.

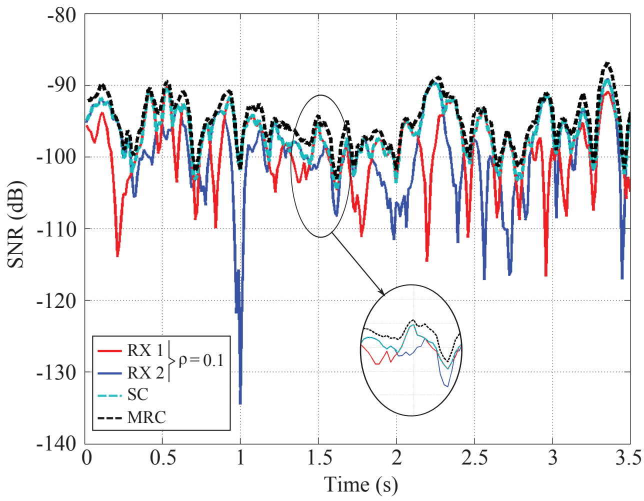

Figure 2.3: Selection Combining and Maximal Ratio Combining in a fading environment

Assuming that the received signals of multiple (on-body) receive antennas are coherently combined, the total received SNR could be increased through array gain [3]. For example, when implementing Maximal Ratio Combining (MRC) [7], the received SNR's on the multiple receive antennas are added up, which results in an increased total received SNR. As an example, assume two receive antennas as in Fig. 2.3. Define s the transmitted symbol with $E[|s|^2] = 1$, r_0 and r_1 the received symbols, h_0 and h_1 the channel coefficients and n_0 and n_1 as Additive White Gaussian Noise (AWGN) with $n_0 \sim (0, \sigma^2)$ and $n_1 \sim (0, \sigma^2)$, assuming equal noise powers, defined as σ^2, in both channels.

$$r_0 = h_0.s + n_0 \rightarrow SNR = \frac{|h_0|^2}{E\left[|n_0|^2\right]} = \frac{|h_0|^2}{\sigma^2} \tag{2.2}$$

$$r_1 = h_1.s + n_1 \rightarrow SNR = \frac{|h_1|^2}{E\left[|n_1|^2\right]} = \frac{|h_1|^2}{\sigma^2} \tag{2.3}$$

Above equations are simplified to:

$$\mathbf{r} = \mathbf{h}s + \mathbf{n} \tag{2.4}$$

with

$$\begin{aligned}
\mathbf{h} &= [h_0 \quad h_1]^T \\
\mathbf{n} &= [n_0 \quad n_1]^T \\
\mathbf{r} &= [r_0 \quad r_1]^T
\end{aligned}$$

The output signal, after MRC combining, is calculated as:

$$\begin{aligned}
r_{MRC} &= \mathbf{w}^H \mathbf{r} && (2.5)\\
&= \mathbf{w}^H \mathbf{h}s + \mathbf{w}^H \mathbf{n} && (2.6)
\end{aligned}$$

The instantaneous SNR is calculated as:

$$\begin{aligned}
\gamma &= \frac{|\mathbf{w}^H \mathbf{h}|^2}{E\left[|\mathbf{w}^H \mathbf{n}|^2\right]} && (2.7)\\
&= \frac{|\mathbf{w}^H \mathbf{h}|^2}{E\left[\mathbf{w}^H \mathbf{n}\mathbf{n}^H \mathbf{w}\right]} && (2.8)\\
&= \frac{|\mathbf{w}^H \mathbf{h}|^2}{\mathbf{w}^H E\left[\mathbf{n}\mathbf{n}^H\right]\mathbf{w}} && (2.9)\\
&= \frac{|\mathbf{w}^H \mathbf{h}|^2}{\sigma^2 \mathbf{w}^H I_N \mathbf{w}} && (2.10)\\
&= \frac{|\mathbf{w}^H \mathbf{h}|^2}{\sigma^2 \mathbf{w}^H \mathbf{w}} && (2.11)\\
&= \frac{\mathbf{w}^H \mathbf{h}\mathbf{h}^H \mathbf{w}}{\sigma^2 \mathbf{w}^H \mathbf{w}} && (2.12)
\end{aligned}$$

By choosing the weighting factors $\mathbf{w}$ equal to the channel coefficients $\mathbf{h}$, the instantaneous SNR is proven the sum of the SNR's of both channels.

$$\begin{aligned}
\gamma &= \frac{\cancel{\mathbf{h}^H \mathbf{h}}\mathbf{h}^H \mathbf{h}}{\sigma^2 \cancel{\mathbf{h}^H \mathbf{h}}} && (2.13)\\
&= \frac{\mathbf{h}^H \mathbf{h}}{\sigma^2} && (2.14)\\
&= \frac{|h_0|^2 + |h_1|^2}{\sigma^2} && (2.15)
\end{aligned}$$

Additionally, the increased SNR increases the maximum channel capacity, calculated using the Shannon-Hartley theorem [8] as:

$$C = B.\log_2\Big(1 + SNR\Big), \tag{2.16}$$

with C the capacity in bps, B the channel bandwidth in Hz and SNR the linear Signal-to-Noise Ratio.

As described before, receive diversity can increase both reliability and capacity through diversity and array gain, respectively. Additionally, when implementing transmit diversity and, hence, creating a (N_{TX}, N_{RX}) Multiple-In Multiple-Out (MIMO) channel, as shown in Fig. 2.4.a, the reliability and channel capacity can further be increased.

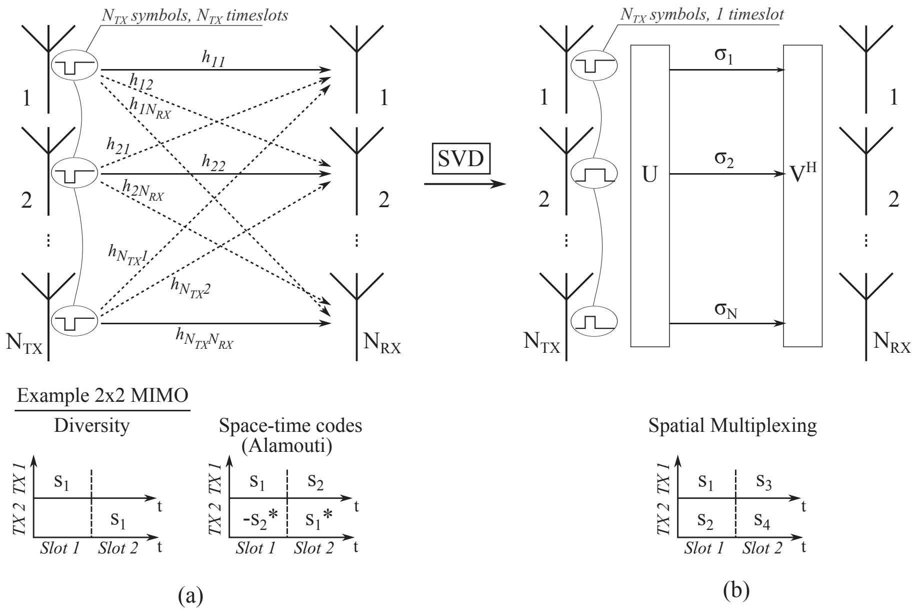

Figure 2.4: Spatial mulitplexing of a (N_{TX}, N_{RX}) MIMO channel by means of Singular Value Decomposition (SVD) and a comparison of diversity, space-time codes (Alamouti) and spatial multiplexing for 2×2 MIMO systems

When applying diversity or space-time codes (STC), a total of N_{TX} symbols are sent over N_{TX} time slots. However, when using space-time codes, redundancy is implemented and all the copies of the received received signal are combined in an optimal way, increasing reliability over simple transmit diversity. Alamouti presented an orthogonal 2×2 MIMO space-time code in [7], as shown in Fig. 2.4.

The MIMO channel capacity can be increased by spatial multiplexing, transmitting N_{TX} symbols in only one timeslot. The channel matrix **H** of a (N_{TX}, N_{RX}) MIMO channel is defined as:

$$\mathbf{H} = \begin{bmatrix} h_{11} & h_{12} & ... & h_{1N_{RX}} \\ h_{21} & h_{22} & ... & h_{2N_{RX}} \\ \vdots & \vdots & \ddots & \vdots \\ h_{N_{TX}1} & h_{N_{TX}2} & ... & h_{N_{TX}N_{RX}} \end{bmatrix}. \tag{2.17}$$

By now applying a Singular Value Decomposition (SVD) [9], the channel matrix **H** is decomposed into:

$$\mathbf{H} = \mathbf{U}\Sigma\mathbf{V}^H \tag{2.18}$$

with $\mathbf{\Sigma}$, defined as the Singular Matrix, a diogonal matrix containing the corresponding N singular values, with $N = \min(N_{TX}, N_{RX})$:

$$\Sigma = \begin{bmatrix} \sigma_1 & 0 & ... & 0 \\ 0 & \sigma_2 & ... & 0 \\ \vdots & \vdots & \ddots & \vdots \\ 0 & 0 & ... & \sigma_N \end{bmatrix}. \tag{2.19}$$

The rank M of the Singular Matrix, defined as the number of non-zero singular values, indicates the possibility to replace the (N_{TX}, N_{RX}) MIMO channel, transmitting one symbol in one timeslot, by M independent symbols in one timeslot. This increases the total throughput and capacity of the MIMO system. In order to properly estimate the performance of spatial multiplexing, the condition number κ is defined as

$$\kappa(\mathbf{H}) = \frac{\sigma_{max}}{\sigma_{min}}. \tag{2.20}$$

If κ equals 1, all singular values are equal, which indicates an optimal scenario for spatial multiplexing since M independent spatial streams can be transmitted without interference at the receiver. Adversely, if κ increases, the MIMO channel conditions become worse for applying spatial multiplexing because of power imbalance in the MIMO channel.

Moreover, the calculated eigenvalues $[\lambda_1, \lambda_2 ... \lambda_N]$, equal to $[\sigma_1^2, \sigma_2^2 ... \sigma_N^2]$, are very useful to optimize the power allocation on the different transmit antennas as described in Chapter 5.

Equivalently, by performing the eigenvalue decomposition on $\mathbf{H}.\mathbf{H}^H$, the same set of eigenvalues is found:

$$\left(\mathbf{H}.\mathbf{H}^H\right).\mathbf{V} = \boldsymbol{\lambda}.\mathbf{V} \tag{2.21}$$

with **V** a full matrix whose columns are the corresponding eigenvectors and $\boldsymbol{\lambda}$ a diagonal matrix containing the eigenvalues $[\lambda_1, \lambda_2 ... \lambda_N]$, similar to the eigenvalues found by means of the singular value decomposition.

2.3 Wideband channel characterization

As stated in Fig. 2.2, to avoid Inter Symbol Interference (ISI) in wireless communication systems, the symbol duration T_S should be chosen sufficiently large. As a rule of thumb, T_S should be larger than the RMS delay spread τ_{RMS}, which is extracted from the power delay profile, as visualized on Fig. 2.5.a for the multipath scenario in Fig. 2.1.

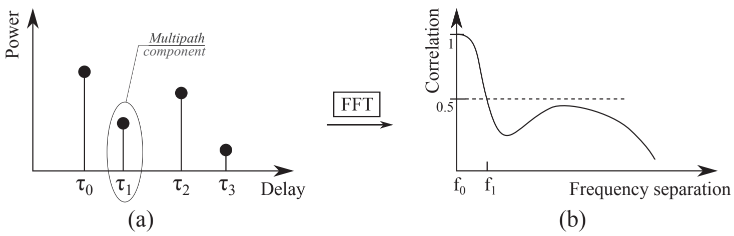

Figure 2.5: Power Delay Profile (a) and Frequency Correlation Function (b)

For L multipath components, the RMS delay spread τ_{RMS} [10] is calculated based on $P_h(\tau)$ using the mean delay $\bar{\tau}$ as:

$$\bar{\tau} = \frac{\sum_{l=1}^{L} P_l \, \tau_l}{\sum_{l=1}^{L} P_l}, \tag{2.22}$$

$$\tau_{RMS} = \sqrt{\frac{\sum_{l=1}^{L} P_l \, (\tau_l - \bar{\tau})^2}{\sum_{l=1}^{L} P_l}}. \tag{2.23}$$

If the calculated τ_{RMS} is not significantly smaller than the symbol duration T_S, strong multipath components of symbol n could influence symbol $n+1$, leading to ISI. Moreover, delayed multipaths, arriving at the RX firefighter, introduce frequency selective fading, which is analyzed by observing the correlation between received signals at two different frequencies [2]. The frequency-selective of the wideband channel is calculated by means of the frequency correlation function $R_T(\nu)$:

$$R_T(\nu) = \int_{-\infty}^{+\infty} P_h(\tau)\, e^{-j2\pi\nu\tau}\, d\tau, \tag{2.24}$$

The 50% correlation bandwith, as indentified on Fig. 2.5.b by the dashed line, indicates that the signal received at frequency f_0 is 50% decorrelated from signals received at frequency f_1. As a rule of thumb, the channel is considered frequency-flat if the bandwidth is one-tenth of the 50% correlation bandwidth [10].

Chapter 4 presents a more detailed, practical example of calculating both wide-band channel parameters.

2.4 OFDM

As described above, multipath propagation has a large influence on the performance of indoor body-centric communication networks. Especially when $\tau > T_S$, Intersymbol Interference introduces frequency-selective fading, meaning that the channel frequency response is not flat but frequency dependent. At first sight, simply increasing the symbol time T_S looks a simple solution to combat ISI. However, an increased symbol time decreases the data rate, which is a major drawback for high-data rate indoor body-centric communication systems.

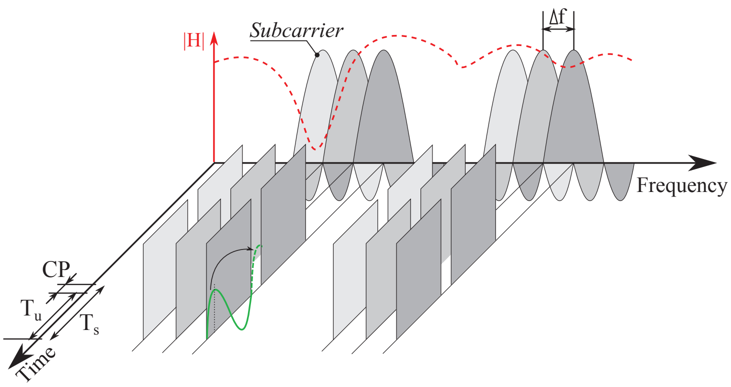

Figure 2.6: Principle of OFDM

Therefore, Orthogonal Frequency Division Multiplexing was introduced as a modulation scheme which is excellent in combatting frequency-selective fading [11], [12]. When applying OFDM, the wideband frequency-selective channel is subdivided into smaller orthogonal subcarriers, each transmitting data at a lower data rate, as shown in Fig. 2.6. However, the combination of all lower data rate subcarriers will dramatically increase the overall data rate and capacity. Moreover, a fading dip in the frequency-selective wideband channel, marked by the red dashed line on Fig. 2.6 a limited number of subcarriers while transmission on the other subcarriers remains reliable.

In the time domain, it is important that two consecutive symbols on one subcarrier do not interefere with each other. Therefore, a Cyclic Prefix (CP) is added at the beginning of a symbol to create a so-called *buffer against late echos* in between two consecutive symbols. This cyclic prefix is in fact a copy of the end of the next symbol, as shown in green on Fig. 2.6. The minimal length of the cyclic prefix is estimated as three times the RMS delay spread τ_{RMS} [10].

To ensure orthogonality of all subcarriers, the OFDM symbol duration T_u should be a whole number of periods for each subcarrier. Defining Δf as the subcarrier spacing, the shortest duration that meets this requirement is [13]:

$$T_u = \frac{1}{\Delta f}. \tag{2.25}$$

The total OFDM duration is then calculated as:

$$T_s = CP + T_u. \tag{2.26}$$

References

[1] A. Molisch, "Technical challenges of wireless communications", in *Wireless Communications*. Wiley-IEEE Press, 2011, pp. 27–36.

[2] R. Janaswamy, *Radiowave Propagation and Smart Antennas for Wireless Communications (The Springer International Series in Engineering and Computer Science)*. Springer, 2000, ISBN: 978-0-30-646990-9.

[3] L. Ordonez, D. Palomar, and J. Fonollosa, "On the diversity, multiplexing, and array gain tradeoff in MIMO channels", in *Information Theory Proceedings (ISIT), 2010 IEEE International Symposium on*, Jun. 2010, pp. 2183–2187.

[4] R. Nabar, H. Bolcskei, V. Erceg, D. Gesbert, and A. Paulraj, "Performance of multiantenna signaling techniques in the presence of polarization diversity", *Signal Processing, IEEE Transactions on*, vol. 50, no. 10, pp. 2553–2562, Oct. 2002.

[5] J. Dietrich C.B., K. Dietze, J. Nealy, and W. Stutzman, "Spatial, polarization, and pattern diversity for wireless handheld terminals", *Antennas and Propagation, IEEE Transactions on*, vol. 49, no. 9, pp. 1271–1281, Sep. 2001.

[6] P. Van Torre, L. Vallozzi, C. Hertleer, H. Rogier, M. Moeneclaey, and J. Verhaevert, "Indoor off-body wireless MIMO communication with dual polarized textile antennas", *IEEE Transactions on Antennas and Propagation*, vol. 59, no. 2, pp. 631–642, Feb. 2011.

[7] S. Alamouti, "A simple transmit diversity technique for wireless communications", *Selected Areas in Communications, IEEE Journal on*, vol. 16, no. 8, pp. 1451–1458, Oct. 1998.

[8] C. Shannon, "A mathematical theory of communication", *Bell System Technical Journal, The*, vol. 27, no. 4, pp. 623–656, Oct. 1948.

[9] A. Paulraj, R. Nabar, and D. Gore, *Introduction to Space-Time Wireless Communications*. Cambridge University Press, 2003, ch. 3, ISBN: 978-0-52-182615-0.

[10] A. Goldsmith, *Wireless Communications*. Cambridge University Press, 2005, ISBN: 978-0-52-183716-3.

[11] R. Prasad, *OFDM for Wireless Communications Systems*. Artech House, Inc, 2004, ISBN: 978-0-52-183716-3.

[12] H. Bolcskei, "MIMO-OFDM wireless systems: Basics, perspectives, and challenges", *Wireless Communications, IEEE*, vol. 13, no. 4, pp. 31–37, Aug. 2006.

[13] N. Marchetti, M. I. Rahman, S. Kumar, and R. Prasad, “New directions in wireless communications research”, in, V. Tarokh, Ed. Boston, MA: Springer US, 2009, ch. OFDM: Principles and Challenges, pp. 29–62.

Part I

In-body communication

About a decade ago, gastro-intestinal (GI) monitoring was equivalent to pushing wide cables, connected to the monitoring device, into the bowel of patients. Next to the limited monitoring area, due to the limited cable length, this was a significantly traumatic and poorly tolerated experience for patients. By the rise of CMOS technology and IC's, swallowable camera pills were developed, heavily increasing the patient's comfort. However, since these camera pills were passive devices, the practical use was somewhat limited. Therefore, research into actively controlled camera pills increased exponentially, introducing concepts such as remote patient-monitoring and real-time tele-operation. In an ideal scenario, low power, active controlled swallowable camera pills ensure bidirectional in-to-out communication, allowing improved locomotion, vision, telemetry, localization and tissue manipulation tools. Therefore, this part focuses on the telemetry, presenting an on-body multi-antenna system that guarantees increased data rate for in-to-out body communication links. This allows, among others, live video streaming from an in-body swallowable camera pill to a remote base station.

3

Improved Reception of In-Body Signals by Means of a Wearable Multi-Antenna System

Thijs Castel, Patrick Van Torre, Emmeric Tanghe, Sam Agneessens, Günter Vermeeren, Wout Joseph, Hendrik Rogier

Published in International Journal of Antennas and Propagation

★ ★ ★

High-data rate wireless communication for in-body human implants is mainly performed in the 402-405 MHz Medical Implant Communication System band and the 2.45 GHz Industrial, Scientific and Medical band. The latter band offers larger bandwidth, enabling high-resolution live video transmission. Although in-body signal attenuation is larger, at least 29 dB more power may be transmitted in this band and the antenna efficiency for compact antennas at 2.45 GHz is also up to 10 times higher. Moreover, at the receive side, one can exploit the large surface provided by a garment by deploying multiple compact highly efficient wearable antennas, capturing the signals transmitted by the implant directly at the body surface, yielding stronger signals and reducing interference. In this chapter, we implement a reliable 3.5 Mbps wearable textile multi-antenna system suitable for integration into a jacket worn by a patient, and evaluate its potential to improve the in-to-out body wireless link reliability by means of spatial receive diversity in a standardized measurement setup. We derive the optimal distribution and the minimum number of on-body antennas required to ensure signal levels that are large enough for real-time wireless endoscopy capsule applications, at varying positions and orientations of the implant in the human body.

3.1 Introduction

Many studies about global aging show an increasing life expectancy in about every continent [1], [2]. This trend is expected to continue in the near future, necessitating a renewed vision on medical healthcare. By enabling wireless communication from inside the body towards the outside world (In-to-Out Body Communication), a whole range of new possibilities arise. In particular, Wireless Capsule Endoscopy (WCE) [3] is an important but technically demanding application. Current commercial WCE systems (Given Imaging, Olympus EndoCapsule) propagate passively through the intestine, and operate at low frame rates [4], [5]. Uncontrolled orientation and movement as well as low resolution are considered a major drawback of passive systems [6]–[8]. This resulted in research towards actively controlled capsules, requiring higher frame rates and resolution to provide real-time video feedback to the physician steering the capsule movement to interactively focus on diagnostically important features [9], [10].

Frequency bands commonly used for wireless implant links are the 402-405 Medical Implant Communication System (MICS) band (or the 401-406 MedRadio band [11]) as well as the 2.45 GHz Industrial, Scientific and Medical (ISM) band. The maximum available bandwidth per channel in the MICS Band is 300 kHz [12], in contrast to the much larger channel bandwidth of 20 MHz in the ISM band [13]. Therefore, the 2.45 GHz band is more suitable for WCE with high-resolution live video transmission [14], [15]. The use of Ultra-Wideband (UWB) technology is proposed for an in-to-out Body link suggesting high data rates, low power consumption and simple electronics [16]–[20]. However, only channel modeling and characterization are described. To our knowledge, no measurements were performed. UWB with diversity is proposed in [21] and [22], documenting a theoretical approach based on simulations. Practically, UWB applications are mostly limited to implants requiring low signal penetration depth, such as cortical implants [23], due to the very high signal attenuation and the limited available transmit power [24]. As the in-body attenuation at 2.45 GHz is smaller than for the 3.4-4.8 GHz low-UWB band [25], the ISM band combines sufficient bandwidth with acceptable attenuation.

We propose a novel reliable high-data rate wearable higher-order diversity in-to-out body communication system to fully compensate for the higher in-body attenuation at 2.45 GHz by mitigating this attenuation using multiple wearable antennas around the body. Diversity systems are realistic in the ISM band, thanks to the much shorter wavelength and smaller dimensions of electrically full-size antennas, compared to the MICS band. Hence, there is enough space for a wearable multi-antenna system on the human body or in a garment. The proposed diversity system enables the use of reliable wide-bandwidth/high-data rate wireless implant links in the 2.45 GHz ISM band. The effect of 4th, 6th and 8th order spatial diversity is examined for an x, y and z-oriented dipole and for different positions of the wearable antennas capturing the signals transmitted by the implant at the surface of a human body phantom.

In addition to applying diversity, the larger in-body attenuation present at 2.45 GHz is partially compensated for by a three orders of magnitude higher allowed transmit power in the ISM band. Regulatory standards limit the (in-body) radiation to 25μW (-16 dBm EIRP) in the MICS band [26]. In the 2.45 GHz ISM band, the European Telecommunications Standards Institute (ETSI) limits transmit power to 100mW (20 dBm EIRP). In addition, for the same ISM band a SAR limit of 2 W/kg averaged over 10g tissue is specified by IEC 62209 [27]. Even if all RF-energy would be absorbed by the 10g tissue directly surrounding the antenna, 20 mW (13 dBm EIRP) is allowed, resulting in at least 29 dB more available transmit power in the 2.45 GHz ISM band, compared to the MICS band. Specifically for steerable endoscopy capsules, the ISM band is a good candidate thanks to the larger bandwidth for the high-data rate video downlink, combined with a possible MICS band uplink for controlling the capsule without mutual interference.

Additionally, thanks to the shorter wavelength, compact yet electrically full-size in-body antennas yield up to 10 dB additional antenna gain for the 2.45 GHz ISM band [28], [29]. Multiple compact on-body antennas allow receive diversity. Moreover, high-speed wireless communication standards are commonly implemented in integrated circuits for this band, resulting in readily available system components. These two advantages allow the design of compact low-power as well as low-cost WCE devices.

In-to-out body communication is an active research topic and important previous work was performed by many research groups. A detailed analysis of wave propagation and radiation efficiency in different human tissues (such as lungs, stomach, liver, heart, skin and muscle), at different frequencies (402 MHz, 868 MHz and 2.45 GHz) is presented in [30]–[33]. A number of advantages of using the 2.45 GHz ISM band instead of the 402-405 MHz MICS band are described in [31]. In [34], a comparison between the body worn antenna efficiency and pattern fragmentation at 418 MHz and 916.5 MHz is presented. Moreover, research on an in-to-out body communication link through human muscle tissue in the 2.45 GHz ISM band is presented in [35] and [36], where path-loss models are derived, with and without inclusion of the antenna gain, respectively. Transceiver development for implantable devices (MICS band) and medical endoscopy applications (ISM band) is presented in [15] and [37], respectively, focusing on low power and high data rates.

To evaluate the performance of our system, we rely on a standardized phantom, compatible with the IEC 62209 standard within the frequency range 30MHz-6GHz, as a means to assess system performance for a person of average size and weight. It is well known that different types of body tissue have varying conductance and permittivity. Yet, muscle tissue ($\sigma_m = 1.7388$ S/m [38]) causes the largest signal attenuation at 2.45GHz. Therefore, the phantom was filled with muscle-simulating liquid to validate the channel in worst-case propagation conditions in an average body size. Recommendations of [29] were followed for human body modeling by using muscle-like dielectric properties, providing standard and easy to reproduce measurement conditions.

This chapter is further organized as follows. Section 3.2 describes the wearable antenna system and the measurement setup. Section 3.3 details the results of the different experiments, examining the performance of different diversity schemes. Finally, the conclusions are presented in Section 3.4.

3.2 Materials and methods

3.2.1 Construction of the wearable antenna system

A wearable multi-antenna system for integration into a jacket was developed, as presented in Fig. 3.1. It consists of a set of wearable on-body textile patch antennas, distributed such that they cover different areas of the body and oriented towards the body to capture the signals transmitted by an in-body implant.

The on-body receiving textile patch antennas are designed to be matched to and radiate into the human body, instead of radiating in free space away from the human body [39]. These antennas exhibit a stable performance for changing parameters such as different body morphologies, movement of the patient, and varying electrical parameters of different organs. The rectangular ring antenna topology with probe feed is shown in Fig. 3.2. Its dimensions are described in the caption of this

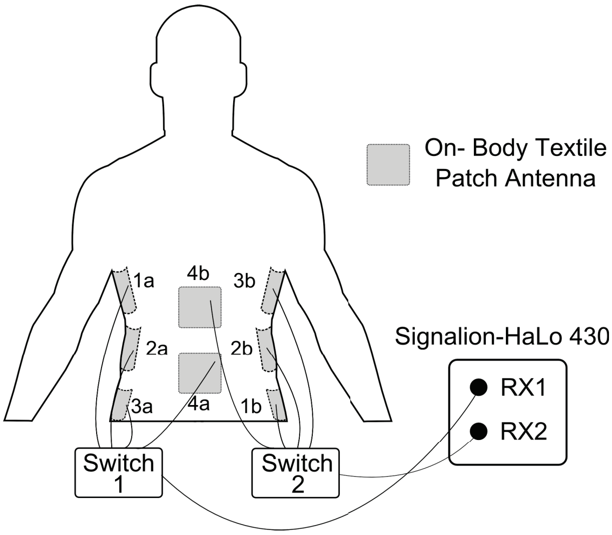

Figure 3.1: Wearable multi-antenna system, with 6 side (1a, 2a, 3a, 1b, 2b, 3b) and 2 back (4a, 4b) antennas, deployed on a patient and connected to the Signalion-HaLo 430 by means of two switches

figure. The antenna substrate consists of very flexible closed-cell expanded protective foam ($\epsilon_r = 1.485$, tan $\delta = 0.0243$), and the ground plane and the patch are fabricated using the 80 μm-thick e-textile Flectron (sheet resistivity 0.18Ω/sq at 2.45GHz). The foam spacer, used to physically separate the body from the conductive part of the antenna and ensuring 50Ω matching in all conditions, is fabricated by means of a foam layer with thickness $h_2 = 7.92$ mm.

By integrating several such on-body receive antennas at suitable locations into a jacket, we obtain a multi-antenna system enabling highly reliable broadband data communication with compact low-power implants. We set the critical level required for highly reliable live wireless video streaming to 10 dB received signal-to-noise ratio (SNR). Given the Shannon-Hartley theorem (2.16), this critical level corresponds to a minimal bitrate of 3.5 Mbit/s within a bandwidth of 1 MHz, which is sufficient for live wireless video streaming, for example, in wireless endoscopy-capsule applications [40], this without the necessity of data buffering and thereby data retransmission, still ensuring correct reception of the inbody signals for all potential positions and orientations of the implant in the human body.

3.2.2 Measurement Setup

Fig. 3.3 depicts the measurement setup and Table 3.1 lists the dimensions of the human body phantom (in cm). The coordinates of the points P1 to P8 are indicated as (x, y).

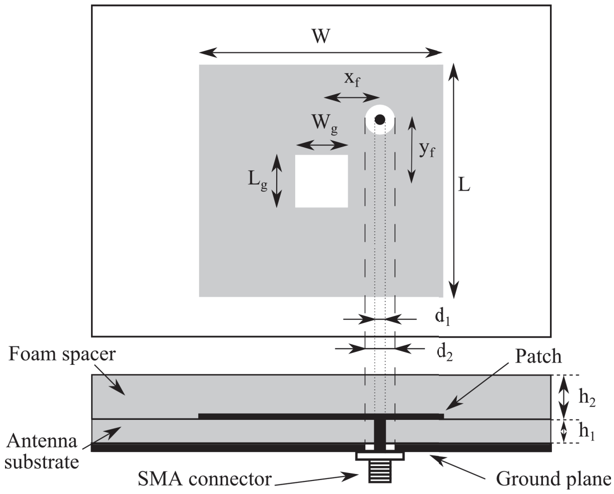

Figure 3.2: Patch Antenna Topology (W=40.9mm, L=48.7mm, W_g=8.8mm, L_g=13.2mm, X_f=7.8mm, Y_f=18.5mm, h_1=3.94mm, h_2=7.92mm, d_1=1.3mm, d_2=5.5mm)

Table 3.1: Human body phantom dimensions

Human body phantom dimensions (cm)						Scan points (x,y)	
W_1	65	A	8.5	A'	31	P1	(0,0)
W_2	59	B	5.2	B'	17.6	P2	(385,0)
L_1	41.5	C	5.1	C'	14.9	P1	(0,215)
L_2	39	D	6.5	D'	13.8	P1	(385,215)
h	18.7	E	9.3	E'	31	P1	(192,105)
h_{vl}	10.2	F	7.5	F'	19.9	P1	(385,105)
S_W	11	G	9.5	G'	17.2	P1	(192,150)
S_{b1}	15	H	13.8	H'	13.8	P1	(385,150)
S_{b2}	13						

In the measurement setup, the implant is represented by an insulated half- wavelength dipole [35], resonating at 2.457 GHz as transmit antenna. The dipole is coated by an insulation of polytetrafluorethylene (ϵ_r=2.07 and σ=0 S/m), as shown in Fig. 3.4. The human body is simulated by an oval ELI flat phantom, fabricated by Speag (Zürich, Switzerland), compatible with the IEC 62209 standard within the frequency range 30MHz-6GHz. This flat phantom is filled with (MSL2450) human muscle tissue mimicking liquid (relative permittivity ϵ_r=50.8, conductivity σ_m=2.01 S/m). Two 50Ω SP4T pin-diode switches (Mini-Circuits ZSDR-425) select the signals, received from the different patch antennas, to be forwarded to the Signalion-HaLo 430 measurement test bed, interfacing to Matlab. A loopback connection is provided to guarantee reliable timing synchronization during post-processing. Details of the transmitted signals and post-processing are described in [41]. Measurements were then performed for varying polarizations of the insulated dipole antenna: an x-oriented horizontal polarization, a y-oriented horizontal polarization and a vertical polarization as also used in [39]. For the x and y orientation, area A was scanned, whereas for the vertical polarization, area B was scanned, both with a step size of 5 mm. Each time, the depth (z-direction) corresponds to a dipole-center position 4.3 cm underneath the liquid surface and at 5.9 cm away from the bottom of the phantom. From the measurements along these 3 axes, we determine the minimum SNR received from an implant with constantly varying orientation, as occurring in WCE applications. The transmit power is 10 mW, corresponding to half the allowed Specific Absorption Rate (SAR) limit of 2 W/kg averaged over 10g tissue [IEC 62209].

3.3 Results and discussion

3.3.1 x-Oriented Dipole

The statistical parameters of the antennas, as viewed in Table 3.2, exhibit deep dips in the SNR for every single on-body receive antenna. These signal dips are much lower than the proposed 10 dB level, so, for a single wearable receive antenna, no optimal position can be determined on the surface of the human body phantom. By using multiple receive antennas, the probability that all antennas simultaneously receive weak signals, strongly decreases. The maxima of the side-wall antennas 2a and 2b are clearly below the maxima of the other six antennas. This is caused by the rectangular scan area in the oval phantom, where, due to the curvature of the ELI phantom, the middle antennas 2a and 2b are located further away from the edges of the scan area, as shown in Fig. 3.3.

Table 3.2: Statistical parameters of the stand-alone antennas (for an x-oriented dipole)

	Max (dB)	Min (dB)	Mean (dB)	Median (dB)
1a	46.68	-1.85	13.32	12.93
2a	24.96	-1.22	12.84	13.32
3a	49.83	-0.30	11.83	12.43
4a	41.87	-1.83	12.46	9.04
1b	40.87	-0.67	12.37	13.44
2b	24.57	-0.32	12.88	12.33
3b	38.80	-2.81	10.81	11.05
4b	38.91	-1.25	11.12	6.98

The envelope correlation matrix for the signal levels, as presented in Table 3.3, demonstrates that all envelope correlation coefficients are far below 0.7, which indicates that the signals, received on the multiple antennas, are strongly uncorrelated, leading to a significant gain when employing spatial diversity [42]. The

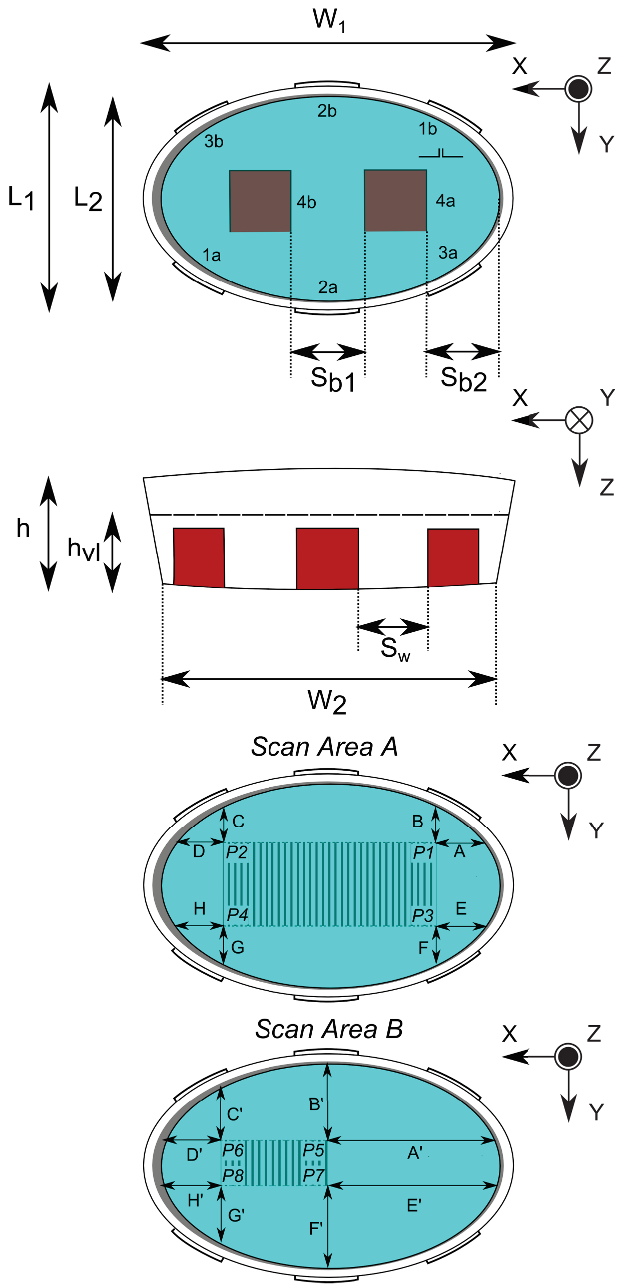

Figure 3.3: Human body phantom (top view, front view, scan area A for an x-and y-oriented dipole and scan area B for a z-oriented dipole)

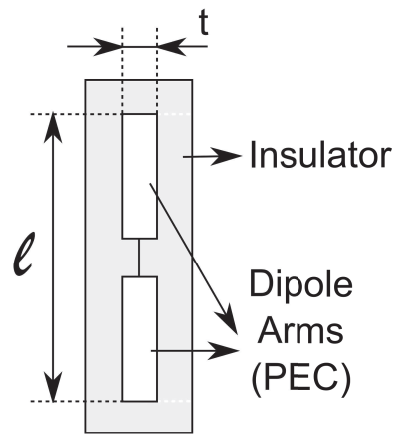

Figure 3.4: Transmitting insulated dipole (t=1mm, l=3.9cm)

negative correlation coefficient between the bottom antennas 4a and 4b, equal to -0.04, indicates that these two antennas are complementary. However, they only cover small non-overlapping parts of the complete scan area. Hence, if 2nd-order spatial diversity is applied based only on these two bottom antennas, the critical 10 dB SNR level will not be guaranteed for the complete area, as further described in Table 3.4. In contrast to the bottom antennas 4a and 4b, the side-wall antennas 2a and 2b have a significantly larger correlation coefficient, equal to 0.47. As these two antennas are deployed at opposite sides, this means that these two side-wall antennas cover a significantly larger area of the oval phantom, with overlap of the covered regions. The correlation between, on the one hand, the side-wall antennas 2a and 2b and, on the other hand, the four other side-wall antennas 1a, 3a, 1b, 3b, is almost negligible. This indicates that by going from 4th-order spatial diversity, only considering corner side antennas 1a, 3a, 1b, 3b, towards 6th-order diversity, where the center side antennas 2a and 2b are added to the diversity scheme, a significant gain will be obtained, as proven further. Since most correlation coefficients are low, mutual coupling between neighboring antennas is small.

By now evaluating an 8th-order receive diversity scheme and verifying if the design requirement of a minimal SNR larger than or equal to 10 dB is fulfilled, some conclusions can already be drawn. Fig. 3.5 shows the SNR (dB) as a function of position, for an x-oriented transmit dipole, applying 8th-order diversity reception using Maximal Ratio Combining (MRC).

Because of the fixed depth of the dipole, the perpendicular distance $d_{bottom-dipole}$ is equal to 5.9 cm, leading to a large SNR received by the bottom antennas (4a and 4b) when the dipole is directly overhead. Note, however, that these antennas only cover a small region of the total scan area. Moreover, the SNR never drops below the critical 10 dB level, enabling live wireless video streaming. Hence, the setup with diversity order 8 and an x-oriented dipole leads to a system that always

Table 3.3: Envelope correlation matrix for the received signals (with x-oriented transmitting dipole)

	1a	3b	2a	2b	3a	1b	4a	4b
1a	1.00	0.16	0.00	-0.03	-0.02	-0.04	-0.02	0.01
3b	0.16	1.00	0.01	-0.01	-0.01	-0.04	-0.03	0.03
2a	0.00	0.01	1.00	0.47	0.01	-0.03	-0.01	-0.03
2b	-0.03	-0.01	0.47	1.00	-0.01	-0.03	-0.04	0.02
3a	-0.02	-0.01	0.01	-0.01	1.00	0.14	0.01	-0.03
1b	-0.04	-0.04	-0.03	-0.03	0.14	1.00	0.07	-0.05
4a	-0.02	-0.03	-0.01	-0.04	0.01	0.07	1.00	-0.04
4b	0.01	0.03	-0.03	0.02	-0.03	-0.05	-0.04	1.00

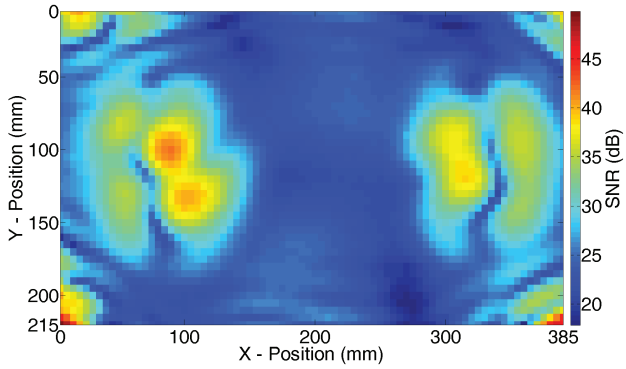

Figure 3.5: SNR (dB) as a function of the position for an x-oriented dipole (8th-order diversity, all antennas included, scan area A)

ensures a sufficiently large SNR. Table 3.4 shows the relevant statistical figures of merit for this setup. By reducing the diversity order from 8 to 6, two main advantages arise. First, the patient comfort increases by removing the antennas on the back (antennas 4a and 4b) and, second, the cost of the wearable antenna system decreases. Figure 3.6 shows the SNR (dB) as a function of the position for 6th order diversity with an x-oriented dipole.

As expected, by removing the bottom antennas that contribute only in a small area, the 6th-order diversity system still satisfies the important 10 dB SNR design requirement. Table 3.4 shows the relevant statistical figures of merit for 8th-, 6th-, 4th- and 2nd-order diversity systems. For 8th-order diversity, all antennas were considered, whereas for 6th-order diversity antennas 4a and 4b were excluded. For 4th order diversity only antennas 1a, 3a, 1b and 3b were considered and for 2nd-order diversity, only bottom antennas 4a and 4b were taken into account. By analyzing Table 3.4 for the x-oriented dipole, it is clear that a 2nd-order diversity system does not result in a reliable multi-antenna system, as the minimal SNR

Table 3.4: Statistical parameters for all dipole orientations and varying diversity orders, where the gain is based on the 10% outage probability level of the CDF. Note the different scan area size for the z-orientation, due to physical constraints (Figure 3)

Dipole orientation	Diversity order	Max. (dB)	Min. (dB)	Mean (dB)	Median (dB)	Gain (dB)
X	8	49.84	17.80	26.44	25.24	13.8
	6	49.84	16.30	23.00	25.24	12.5
	4	49.83	11.85	20.90	20.04	9.5
	2	41.87	4.30	18.91	20.48	2.1
Y	8	47.16	18.34	26.77	25.30	14.2
	6	44.27	17.96	24.46	24.37	13.2
	4	44.26	13.69	22.24	21.71	9.7
	2	47.12	3.88	17.70	18.09	0.5
Z	8	27.99	10.85	16.89	17.32	9.25
	6	11.83	8.74	10.25	10.16	7.65
	4	10.97	6.87	8.69	8.56	6.15
	2	27.92	3.34	14.40	16.34	2.45

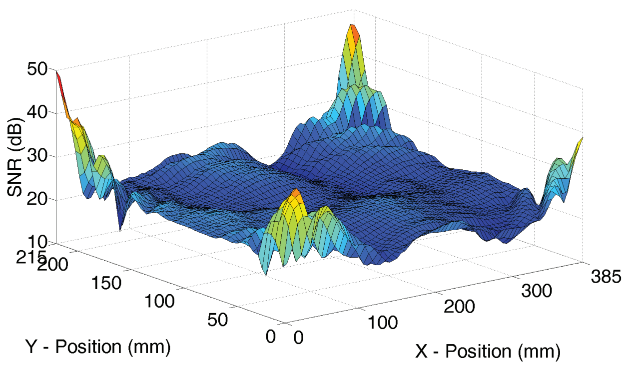

Figure 3.6: SNR (dB) as a function of the position for an x-oriented dipole (6th order diversity, bottom antennas 4a and 4b excluded, scan area A)

equals 4.30 dB, which is far below the 10 dB limit. By focusing further on the minimal SNR, some tendencies can be extracted from Table 3.4. When increasing the diversity order from 4 towards 6, the minimal SNR increases by 4.45 dB. This significant gain is obtained thanks to the inclusion of antennas 2a and 2b, which cover a large area. When further increasing the diversity order from 6 to 8, the minimal SNR increases only by an extra 1.50 dB. Including the bottom antennas 4a and 4b in the 8th-order diversity scheme only results in marginal improvements in diversity gain, as they only partly cover the scan area. The Cumulative Distribution Function (CDF) of the obtained SNR gives an indication about the gain obtained by applying different orders of diversity. This CDF, corresponding to P[X ≤ SNR(dB)], is shown in Fig. 3.7.

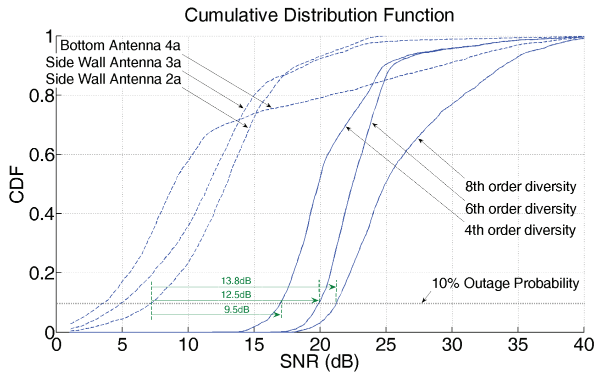

Figure 3.7: Cumulative Distribution Function (for an x-oriented dipole)

Fig. 3.7 shows the CDFs for different orders of diversity. In order not to overload the plot, for the cases without diversity, realized by the single antennas, we only display the results for the bottom-antenna with the highest SNR (4a), for the best middle side-wall antenna (2a) and for the best corner side-wall antenna (3a). The CDFs for the other five remaining antennas are shaped similar to their counterparts located at equivalent positions. By focusing on the best-case scenario, the minimal gain provided by implementing diversity is calculated.

Setting the criterion of an absolute minimum SNR of 10 dB guarantees continuous live video transmissions at an acceptable data rate without missing packets and without the need for a feedback link. However, the 10% outage probability level indicates the minimal SNR level and corresponding data rate that may be frequently obtained. On the condition that a channel feedback link is present, an endoscopy capsule can always use the currently available maximum data rate, which is controlled through feedback from the receiver. The in-body implant then needs to have memory to temporally buffer the recorded data and provisions should be made to request retransmissions of potentially missed data packets. At the expense of higher power consumption and more complex hardware at both sides of the links, such a scheme enables transmissions of higher quality video signals, compared to a system without a feedback link.

The gains, obtained for different orders of diversity, are clearly visible as a shift to the right in the CDFs of different orders. Focusing on the 10% outage probability level, the 6th-order diversity performs 3 dB better than 4th-order diversity and 8th-order diversity performs 1.3 dB better than the 6th-order diversity system. The minimal gain in terms of 10% outage probability, when comparing antenna 2a (which has the best single-antenna signal behavior) to 4th-, 6th- and 8th-order diversity, is 9.5 dB, 12.5 dB and 13.8 dB, respectively.

As seen on Fig. 3.7, antennas 3a and 2a have an equally shaped CDF. However, the median of antenna 3a is 2 dB less than the median of antenna 2a, which illustrates the larger coverage of the middle side-wall antennas 2a and 2b. The CDF of the bottom antenna 4a exhibits a high SNR for only a small part of the scanned area. The influence of these bottom antennas is clearly visible in the CDF of the 8th-order diversity system, especially for the higher SNR values. It is clear that, for an x-oriented dipole, the 4th-order multi-antenna system still satisfies the proposed design requirement of the minimal SNR $\geq$ 10dB. Next, the results for a y and z-oriented dipole are presented and compared with the previous results. From this, the minimal diversity order, guaranteeing high-reliability data communication for all potential dipole orientations, is derived.

3.3.2 y-Oriented Dipole

In the remainder, we focus on 8th-, 6th- and 4th-order diversity. To make a comparison with the x-oriented dipole, Figure 3.8 shows the SNR (dB) as a function of the position, for a y-oriented transmitting dipole, with 6th order diversity reception applied.

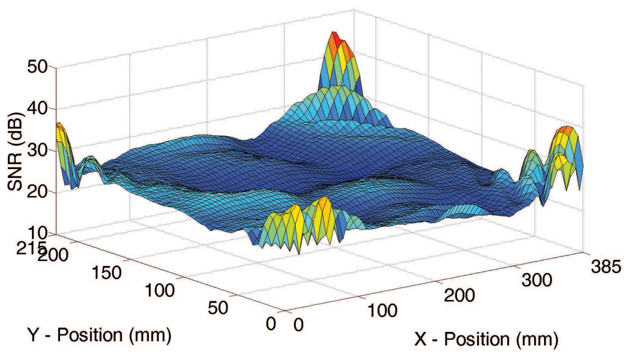

Figure 3.8: SNR (dB) as a function of the position for a y-oriented dipole (6th order diversity, bottom antennas 4a and 4b excluded, scan area A)

Again, a 6th order multi-antenna diversity system satisfies the requirement of a minimal SNR $\geq$ 10 dB. Table 3.4 shows the statistical figures of merit, for an 8th-, 6th- and 4th-order diversity system in case of a y-oriented dipole. Again, a 4th-order diversity system provides a sufficiently large minimum SNR, more than 3 dB higher than the critical 10 dB limit. The CDFs, as well as the correlation matrix, show the same tendencies as in the case of an x-oriented dipole. When focusing on the 10% outage probability for the CDF, the minimal gain, when comparing reception by antenna 2a (which has again the best single-antenna behavior) to 4th-, 6th- and 8th-order diversity, is equal to 9.7 dB, 13.2 dB and 14.2 dB, respectively.

Hence, the minimal gain for each diversity order is slightly higher than for an x-oriented dipole. As in the previous situation for an x-oriented dipole, a diversity order of 6 seems to be optimal considering a balance between simplicity and/or cost, on the one hand, and highly reliable data links, on the other hand.

3.3.3 z-Oriented Dipole

Due to the small dimensions of the phantom, and the lengthy feeding part of the dipole, only a limited area B could be scanned for a vertically oriented dipole. This scan area B was also shown in Fig. 3.3. The most important region is in the middle because of the critical low SNR's that could occur when excluding the bottom antennas. Given the x and y-symmetry of the phantom, conclusions can be extended to the complete phantom. Table 3.4 presents the statistical figures of merit for 8th-, 6th- and 4th-order diversity in the case of a z-oriented dipole scanning the left-middle area of the bath (scan area B). The gain is again calculated for the 10% outage probability level but now compared to reception by antenna 3b, which has the best single antenna behavior for the z-oriented dipole. Table 3.4 shows that 6th-order diversity doesn't ensure a sufficiently large SNR, due to the minimal SNR equal to 8.74 dB, which indicates that, for a z-oriented dipole, 8th-order diversity is necessary to guarantee a minimal SNR $\geq$ 10 dB. Because of the large influence of bottom antenna 4b in scan area B, the bottom antennas are excluded in Fig. 3.9, allowing more insight into the performance of the side-wall antennas. Fig. 3.9 shows the SNR (dB) as a function of the position, for a z-oriented transmitting dipole, with 6th-order diversity reception applied.

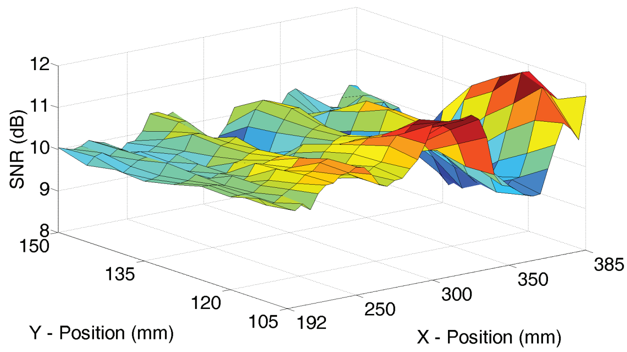

Figure 3.9: SNR (dB) as a function of position for a z-oriented dipole (6th-order diversity, bottom antennas excluded, scan area B)

As Table 3.4 already indicated, the statistical values are below those of an x and y-oriented dipole for the same diversity order. This is because of the limited scan area B, where the distance to the side wall antennas is large compared to scan area A. For 6th order diversity, as presented in Fig. 3.9, 34.2% of the scan points are below the critical 10 dB SNR limit. However, the applied TX power at the implant is only half the allowed SAR limit [IEC 62209] hence when doubling the TX power to 20 mW, the SNRs obtained with 6th order diversity increase by 3 dB. In that case, the SNRs for the complete scan area would be above 10 dB, with a minimum of 11.74 dB.

3.4 Conclusion

A multi-antenna system was developed for capturing high-data rate signals transmitted by implants. All antennas in this wearable system are flexible and fully fabricated using textile materials. Hence, the complete system can be easily and unobtrusively integrated into a jacket or another type of garment. The system is fully tested experimentally, by distributing the different antennas over the surface of a human body phantom, in order to determine the optimal antenna positions and the required diversity order for reliable high data rate communication with the implant. When limiting the TX power to 10 mW, which is half the allowed SAR limit, 8th-order spatial diversity is needed to allow live wireless video streaming with a bandwidth of 1 MHz and a bit rate of 3.5 Mbit/s. When doubling the TX power to 20 mW, 6th-order spatial diversity is sufficient to meet the imposed design requirements in all cases. This improves patient comfort and allows the use of the multi-antenna system even when a patient is lying in a (hospital) bed, which could prove uncomfortable if two 'back'-antennas are deployed in the patient's garment, as in case of 8th-order diversity. An important conclusion is that spatial diversity for an in-to-out body communication scenario allows the use of a simple transmit antenna in the implant, such as a single dipole antenna. The on-body wearable multi-antenna system then ensures a high-quality wireless link for any arbitrary orientation and position of the implant. In the perspective of wireless-endoscopy applications, the use of a simple antenna, operating at low power levels in the implanted capsule, decreases costs, size and complexity of wireless camera capsule and increase its battery life.

References

[1] K. Kinsella and D. R. Philips, “Global aging: The challenge of success”, *Population Bulletin*, vol. 60, no. 1, pp. 1–40, Mar. 2005.

[2] M. E. Pollack, “Intelligent technology for an aging population: the use of ai to assist elders with cognitive impairment”, *AI Magazine*, vol. 26, no. 2, pp. 9–24, 2005.

[3] G. Iddan, G. Meron, A. Glukhovsky, and P. Swain, “Wireless capsule endoscopy”, *Nature*, vol. 405, no. 6785, pp. 417–418, May 2000.

[4] Z. Wang, E. Gee, T. Tillo, and F. Yu, “Review of the wireless capsule transmitting and receiving antennas”, *Wireless Communications and Networks - Recent Advances*, Mar. 2012.

[5] A. Karargyris and N. Bourbakis, “Three-dimensional reconstruction of the digestive wall in capsule endoscopy videos using elastic video interpolation”, *IEEE Transactions on Medical Imaging*, vol. 30, no. 4, pp. 957–971, Apr. 2011.

[6] J. Hou, Y. Zhu, L. Zhang, Y. Fu, F. Zhao, L. Yang, and G. Rong, “Design and implementation of a high resolution localization system for in-vivo capsule endoscopy”, in *Proceedings of the 8th International Conference on Dependable, Autonomic and Secure Computing (DASC)*, Chengdu, China: IEEE, Dec. 2009, pp. 209–214.

[7] Y. Fan and M. Q.-H. Meng, “3D reconstruction of the WCE images by affine SIFT method”, in *Proceedings of the 9th World Congress on Intelligent Control and Automation*, Tapei, Japan: IEEE, Jun. 2011, pp. 943–947.

[8] J. Thoné, S. Radiom, D. Turgis, R. Carta, G. Gielen, and R. Puers, “Design of a 2Mbps FSK near-field transmitter for wireless capsule endoscopy”, *Sensors and Actuators A: Physical*, vol. 156, no. 1, pp. 43–48, Nov. 2009.

[9] G.-S. Lien, C.-W. Liu, J.-A. Jiang, C.-L. Chuang, and M.-T. Teng, “Magnetic control system targeted for capsule endoscopic operations in the stomach - design, fabrication, and in vitro and ex vivo evaluations”, *IEEE Transactions on Biomedical Engineering*, vol. 59, no. 7, pp. 2068–2079, Jul. 2012.

[10] F Carpi, N Kastelein, M Talcott, and C Pappone, “Magnetically controllable gastrointestinal steering of video capsules”, *IEEE Transactions on Biomedical Engineering*, vol. 58, no. 2, pp. 231–234, Feb. 2011.

[11] E. Chow, M. Morris, and P. Irazoqui, “Implantable RF medical devices: The benefits of high-speed communication and much greater communication distances in biomedical applications”, *IEEE Microwave Magazine*, vol. 14, no. 4, pp. 64–73, Jun. 2013.

[12] “95.627 medradio transmitters in the 401-406 mhz band,"in "code of federal regulations, title 47-telecommunications, chapter 1-fcc, subchapter d-safety and special radio services, part 95-personal radio services, subpart e-technical regulations”, Federal Communications Commission, Tech. Rep., 2012.

[13] “Electromagnetic compatibility and radio spectrum matters (erm); wideband transmission systems; data transmission equipment operating in the 2,4 ghz ism band and using wide band modulation techniques”, European Telecommunications Standards Institute, Tech. Rep. EN 300 328 V1.8.1, 2012.

[14] X. Xie, G. Li, X. Chen, X. Li, and Z. Wang, “A low-power digital ic design inside the wireless endoscopic capsule”, *IEEE Journal of Solid-State Circuits*, vol. 41, no. 11, pp. 2390–2400, Nov. 2006.

[15] B Chi, J Yao, Han, X Xie, G Li, and Z. Wang, “Low-power transceiver analog front-end circuits for bidirectional high data rate wireless telemetry in medical endoscopy applications”, *IEEE Transactions on Biomedical Engineering*, vol. 54, no. 7, pp. 1291–1299, Jul. 2007.

[16] A. Khaleghi, R. Chavez-Santiago, X. Liang, I. Balasingham, V. C. M. Leung, and T. A. Ramstad, “On ultra wideband channel modeling for in-body communications”, in *Proceedings of the 5th International Symposium on Wireless Pervasive Computing*, Modena, Italy: IEEE, May 2010, pp. 140–145.

[17] A. Khaleghi and I. Balasingham, “Improving in-body ultra wideband communication using near-field coupling of the implanted antenna”, *Microwave and Optical Technology Letters*, vol. 51, no. 3, pp. 585–589, Mar. 2009.

[18] S. Stoa, R. Chavez-Santiago, and I. Balasingham, “An ultra wideband communication channel model for capsule endoscopy”, in *Proceedings of the 3rd International Symposium on Applied Sciences in Biomedical and Communication Technologies (ISABEL)*, Rome, Italy: IEEE, Nov. 2010, pp. 1–5.

[19] Q. Wang, K. Masami, and J. Wang, “Channel modeling and BER performance for wearable and implant UWB body area links on chest”, in *Proceedings of the International Conference on Ultra-Wideband (ICUWB)*, Vancouver, Canada: IEEE, Sep. 2009, pp. 316–320.

[20] A. Ghildiyal, K. Amara, R. D. Molin, B. Godara, A. Amara, and R. K. Shevgaonkar, “UWB for in-body medical implants: A viable option”, in *Proceedings of the IEEE International Conference on Ultra-Wideband (ICUWB)*, vol. 2, Nanjing, China: IEEE, Sep. 2010, pp. 1–4.

[21] J. Shi and J. Wang, “Channel characterization and diversity feasibility for in-body to on-body communication using low-band UWB signals”, in *Proceedings of the 3rd International Symposium on Applied Sciences in Biomedical and Communication Technologies (ISABEL)*, Rome, Italy: IEEE, Nov. 2010, pp. 1–4.

[22] J. Shi, D. Anzai, and J. Wang, "Diversity performance of UWB low band communication over in-body to on-body propagation channel", in *Proceedings of the 6th European Conference on Antennas and Propagation (EUCAP)*, Prague, Czech Republic: IEEE, Mar. 2012, pp. 535–539.

[23] Y. Luo, C. Winstead, and P. Chiang, "125Mbps ultra-wideband system evaluation for cortical implant devices", in *Proceedings of the 34th Annual International Conference of the IEEE Engineering in Medicine and Biology Society (EMBC)*, San Diego, CA, USA: IEEE, Aug. 2012, pp. 779–782.

[24] A. Ghildiyal, B. Godara, K. Amara, R. Dal Molin, and A. Amara, "Ultra wideband for in and on-body medical implants: A study of the limits and new opportunities", in *Proceedings of the 5th European Conference on Antennas and Propagation (EUCAP)*, Rome, Italy: IEEE, Apr. 2011, pp. 3778–3782.

[25] J. Wang and Q. Wang, "Channel modeling and BER performance of an implant UWB body area link", in *Proceedings of the 2nd International Symposium on Applied Sciences in Biomedical and Communication Technologies (ISABEL)*, Bratislava, Slovakia: IEEE, Nov. 2009, pp. 1–4.

[26] "Electromagnetic compatibility and radio spectrum matters (erm); ultra low power active medical implants (ulp-ami) operating in the 401 mhz to 402 mhz and 405 mhz to 406 mhz bands", European Telecommunications Standards Institute (ETSI), System Reference Document 102 343 v1.1.1, 2004-07.

[27] "Human exposure to radio frequency fields from hand-held and body-mounted wireless communication devices-human body models", International Electrotechnical Commission, Instrumentation and Procedures IEC62209 Standard, 2010.

[28] T. Karacolak, A. Hood, and E. Topsakal, "Design of a dual-band implantable antenna and development of skin mimicking gels for continuous glucose monitoring", *IEEE Transactions on Microwave Theory and Techniques*, vol. 56, no. 4, pp. 1001–1008, Apr. 2008.

[29] F. Merli, L. Bolomey, J. Zurcher, G. Corradini, E. Meurville, and A. Skrivervik, "Design, realization and measurements of a miniature antenna for implantable wireless communication systems", *IEEE Transactions on Antennas and Propagation*, vol. 59, no. 10, pp. 3544–3555, Aug. 2011.

[30] A. Alomainy and Y. Hao, "Modeling and characterization of biotelemetric radio channel from ingested implants considering organ contents", *IEEE Transactions on Antennas and Propagation*, vol. 57, no. 4, pp. 999–1005, Apr. 2009.

[31] Y. Chan, M H. Meng, L. W. K., and X. Wang, "Experimental study of radiation efficiency from an ingested source inside a human body model", in *Proceedings of the 27th Annual International Conference of the Engineering in Medicine and Biology Society (EMBS)*, Shanghai, China: IEEE, Sep. 2005, pp. 7754–7757.

[32] A. Alomainy, Y. Hao, Y. Yuan, and Y. Liu, “Modelling and characterisation of radio propagation from wireless implants at different frequencies”, in *Proceedings of the 9th European Conference on Wireless Technologies (ECWT)*, Manchester, UK: IEEE, Sep. 2006, pp. 119–122.

[33] A. Sani, A. Alomainy, and Y. Hao, “The effect of various human body tissue models on radiowave propagation from a bladder implanted wireless source”, in *Proceedings of the IEEE Antennas and Propagation Society International Symposium (APSURSI)*, Charleston, South Carolina, USA: IEEE, Jun. 2009, pp. 1–4.

[34] W. Scanlon, B. Burns, and N. Evans, “Radiowave propagation from a tissue-implanted source at 418MHz and 916.5MHz”, *IEEE Transactions on Biomedical Engineering*, vol. 47, no. 4, pp. 527–534, Apr. 2000.

[35] D. Kurup, W. Joseph, G. Vermeeren, and L. Martens, “In-body path loss model for homogeneous human tissues”, *IEEE Transactions on Electromagnetic Compatibility*, vol. 54, no. 3, pp. 556–564, Jun. 2012.

[36] D. Kurup, W. Joseph, E. Tanghe, G. Vermeeren, and L. Martens, “Extraction of antenna gain from path loss model for in-body communication”, *Electronics Letters*, vol. 47, no. 23, pp. 1262–1263, Nov. 2011.

[37] P. D. Bradley, “An ultra low power, high performance medical implant communication system (mics) transceiver for implantable devices”, in *Proceedings of the IEEE Biomedical Circuits and Systems Conference*, London, UK: IEEE, Nov. 2006, pp. 158–161.

[38] Calculation of the dielectric properties of body tissues in the frequency range 10Hz - 100GHz, *Italian national research council - institute for applied physics, daniele andreuccetti, roberto fossi and caterina petrucci*, 1997.

[39] S. Agneessens, P. Van Torre, E. Tanghe, G. Vermeeren, W. Joseph, and H. Rogier, “On-body wearable repeater as a data link relay for in-body wireless implants”, *IEEE Antennas and Wireless Propagation Letters*, vol. 11, pp. 1714–1717, Jan. 2012.

[40] G. Ciuti, A. Menciassi, and P. Dario, “Capsule endoscopy: From current achievements to open challenges”, *IEEE Reviews in Biomedical Engineering*, vol. 4, pp. 59–72, Oct. 2011.

[41] L. Vallozzi, P. Van Torre, C. Hertleer, H. Rogier, M. Moeneclaey, and J. Verhaevert, “Wireless communication for firefighters using dual-polarized textile antennas integrated in their garment”, *IEEE Transactions on Antennas and Propagation*, vol. 58, no. 4, pp. 1357–1368, Apr. 2010.

[42] S. Alamouti, “A simple transmit diversity technique for wireless communications”, *Selected Areas in Communications, IEEE Journal on*, vol. 16, no. 8, pp. 1451–1458, Oct. 1998.

PART II

Body-to-body communication

Our analysis of indoor body-to-body communication is threefold. First, we analyze whether the widely used Long Term Evolution (LTE) standard is suitable for indoor public safety networks. As this LTE standard applies Orthogonal Frequency Division Multiplexing (OFDM), we verify whether the LTE's Cyclic Prefix length (CP) and subcarrier bandwidth (Δf), as briefly introduced in Chapter 2, are compatible with an indoor body-to-body communication channel, as presented in Chapter 4. Second, since we are focusing on high-data rate body-to-body communication, allowing live video streaming between on-duty firefighters, we analyze the potential capacity of SISO, SIMO, MISO and MIMO-OFDM channels. Moreover, we study capacity enhancement techniques as one-and two dimensional waterfilling, presented in Chapter 5, and adaptive modulation per OFDM subcarrier, as described in Chapter 6. Finally, in Chapter 7, the design of an ultra-wideband dual-spatial, dual-polarization antenna array is proven very suitable to further increase reliability, in combination with increased throughput, of SIMO wideband body-to-body links.

4

LTE as a Potential Standard for Indoor Public Safety Networks

Thijs Castel, Sam Lemey, Sam Agneessens, Patrick Van Torre, Hendrik Rogier and Claude Oestges

Published in the proceedings of the 22nd IEEE Symposium on Communications and Vehicular Technology in the Benelux

★ ★ ★

In this chapter, a wideband indoor body-to-body communication channel is characterized and analyzed into detail by means of the RMS delay spread and the 50% correlation bandwidth. These body-to-body channel parameters are calculated based on high-resolution power delay profiles, directly provided by the Elektrobit channel sounder, and are further analyzed using a ray tracing algorithm. We have replicated a real-life rescue operation, performed by two firefighters as part of the Rapid Intervention Team searching for potential victims, operating at the same floor of an office block. Both firefighters, who were simultaneously moving around in the vicinity of each other, were equipped with two cavity-backed Substrate Integrated Waveguide textile antennas unobtrusively integrated in the front and back section of their jackets, allowing us to analyze four independent body-to-body links. Furthermore, we prove that the Long Term Evolution (LTE) and, by extension, the LTE - Device to Device (LTE-D2D) standard is compatible with this indoor body-to-body channel. This could provide high-data rate indoor communication between rescuers, enabling multimedia broadcast and real-time communication of on-body sensor data in public safety networks.

4.1 Introduction

State-of the art narrowband public safety networks, such as TETRA [1], provide a wide variety of applications which help rescue workers to perform their jobs in an efficient manner and, hence, decrease the number of casualties. However, broadband networks could further improve life-critical communication by allowing high data rates, low latency and high spectral efficiency [2], [3], enabling multimedia broadcast and efficient communication of on-body sensor data. By providing real-time information to on-duty rescuers, their situational awareness increases, which strengthens their decision-making process and, hence, decreases the response time of operations. This can be of great importance when minutes, or even seconds, count.

Long Term Evolution (LTE) [4] is seen as the future mainstream cellular based network solution for public safety networks used by first responders. However, since highly reliable communication between the rescuers is required at any time, even when the cellular coverage fails or is not available, the LTE Device-to-Device (LTE-D2D) standard could be more suitable for indoor body-to-body communication between rescuers. This extension of the general LTE standard is defined as low-latency, energy-saving communication between two (on-body) User Equipment (UE) devices, in the proximity of each other, using an LTE air interface to set up a direct link without routing via an Evolved Node B (eNB) [5]. In this chapter, we analyze if an indoor body-to-body network is compatible with LTE and, by extension, the LTE-D2D standard. Therefore, we performed wideband, indoor, body-to-body channel sounder measurements between two simultaneously moving firefighters, equipped with two integrated textile antennas, providing a sufficiently large set of reliable channel measurements to determine the wideband channel parameters, being the RMS delay spread and the 50% correlation bandwidth. These wideband channel parameters are then used to determine the pertinent Orthogonal Frequency Division Multiplexing (OFDM) parameters to verify the compatibility of the indoor environment with LTE, and, by extension, LTE-D2D.

When focusing on body-to-body communication, [6] and [7] present channel characterization for *narrowband* dynamic body-to-body communication channels at 2.45 GHz. Channel characterization of the *wideband* body-to-body transmissions by means of static and dynamic measurements, not replicating real-life rescue scenarios, is described in [8]. Moreover, directional stacked patch antennas were mounted on the human body instead of the antennas being unobtrusively integrated into the clothing. To the authors' best knowledge, this is the first work which presents a detailed analysis of an indoor wideband body-to-body communication channel using high-resolution channel sounding measurements supplemented with ray-tracing results. Moreover, for the first time in literature, the chapter validates, by means of real channel sounder measurements, that the LTE standard is very suitable for indoor body-to-body links between on-duty rescuers.

4.2 Measurement setup

Two Ultra-Wideband cavity-backed slot antennas in Substrate Integrated Waveguide (SIW) technology [9] were unobtrusively integrated inside the front and back sections of rescuer workers' garments, as shown in Fig 4.1. The fabricated antenna is matched for the frequency band ranging from 3.33 GHz to 4.66 GHz, with a -10 dB bandwidth of 1.33 GHz and a fractional bandwidth of 33%. Moreover, this topology provides stable radiation characteristics when placed on different on-body locations or even when the antenna is bent, which typically occurs in real-life rescue operations. Furthermore, owing to the use of a groundplane, the antenna radiates away from the firefighter while minimizing the backside radiation towards the firefighter's body which guarantees safe and energy-efficient operation and, hence, makes this antenna topology very suitable for on-body usage. Additionally, the fabricated SIW textile antenna is small, low-profile, lightweight and flexible. This enables easy deployment inside a rescuer's jacket.

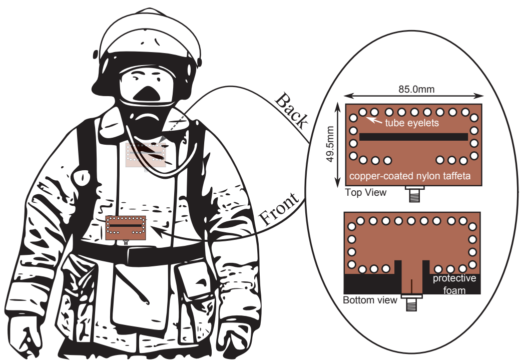

Figure 4.1: Front and back locations of the two integrated UWB SIW textile antennas, for both the TX and RX firefighter.

A real-life rescue operation, performed by the Rapid Intervention Team looking for potential victims, was replicated by mobile measurements during which both firefighters were simultaneously moving around on the same floor of an office block. When both firefighters enter a building, according to the commonly employed ”two in - two out” principle, the RX firefighter, whose trajectory is marked by the short dashed line on Fig. 4.2, starts scanning the offices whereas the TX firefighter, whose trajectory is marked by the long dashed line, is simultaneously scanning the hallway, while he remains in the vicinity of the RX firefighter. The markers A, B and C, placed along both firefighter trajectories, indicate where the firefighters are located at the same time instance during the one minute long measurement, gathering 4650 measurement cycles. Measurements were performed using the ULB-UCL Elektrobit channel sounder at 3.6 GHz center frequency with 120 MHz useful bandwidth. The TX power was chosen equal to 20 dBm to obtain reliable wideband channel measurements.

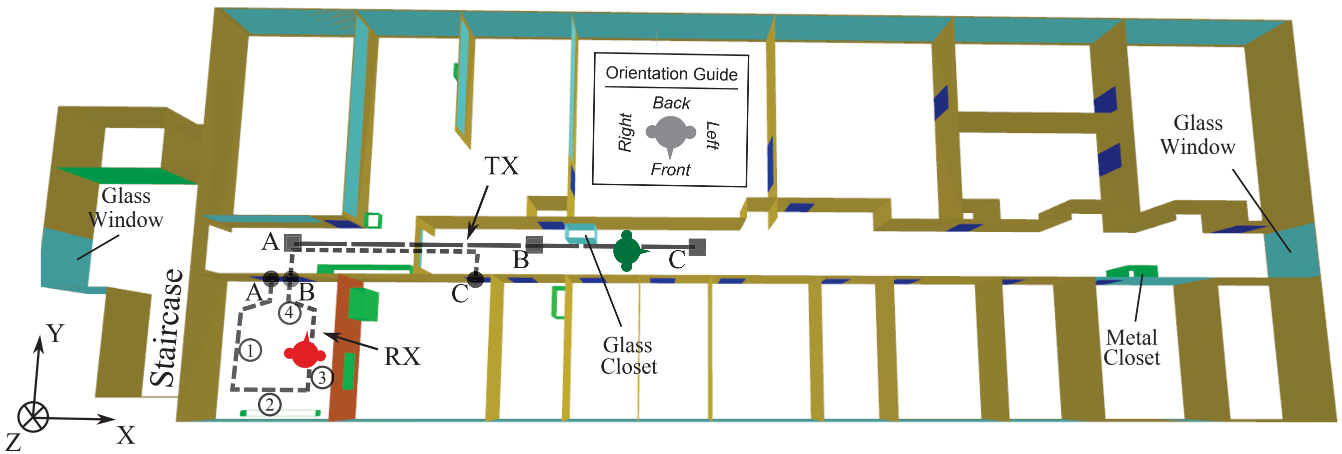

Figure 4.2: Simplified indoor office model with the wideband body-to-body measurement scenario

4.3 Wideband channel characterization

Indoor body-to-body communication is heavily influenced by multiple delayed paths arriving at the RX firefighter, caused by several reflectors and scatterers in the office environment. The time-varying power delay profiles $P_h(\tau)$, showing the power and the corresponding delays of these multipath components together with the power and the delay of the dominant, strongest path, are visualized in Fig. 4.3 for all four body-to-body links.

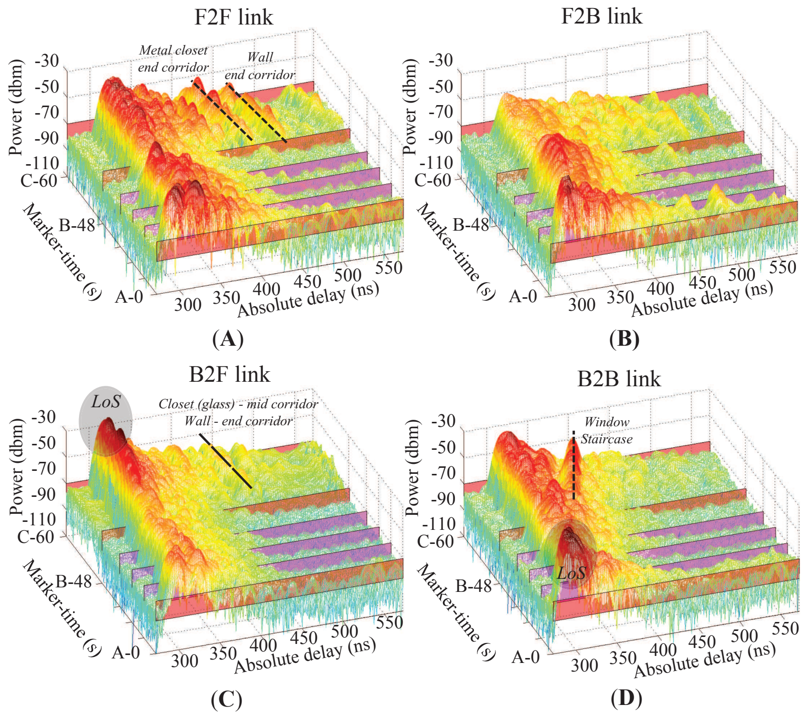

Figure 4.3: Time-varying power delay profiles $P_h(\tau)$ for all four body-to-body links

A number of interesting features are observed for the Front to Front (F2F) link when both firefighters are walking in the corridor (interval BC on Fig. 4.2) along the same positive X direction towards the end of the corridor. The last arriving multipath components, originating from the TX front antenna and impinging on the RX front antenna, decrease in delay, as seen on Fig. 4.3A. The opposite holds for the *B2B* link, as seen on Fig. 4.3D, in the same interval BC, where again, both firefighters are walking in the corridor (interval BC) along the same positive X direction towards the end of the corridor. Here, the dominant multipath component, transmitted by the TX back antenna and impinging on the RX back antenna, increases in delay and path length.

By modelling the indoor environment using the AWE Communication - Winprop ray tracing algorithm [10], we try to calculate the propagation paths of each multipath component in $P_h(\tau)$. Despite the fact that the office environment cannot be modelled into great detail because of the large number of potential reflectors and absorbers, such as computers, desks, people . . . , which cannot all be included inside our model, a correlation coefficient of 0.91 is obtained between the power delay profile of the last measurement cycle in interval BC and by the ray tracing algorithm for the *F2F* as shown in Fig. 4.4. This good agreement is obtained by incoperating the most important scatterers on the simplied indoor office model, such as the metal and glass closets, windows, doors and walls, as also visible in Fig. 4.2. Because of diffuse multipath component, which cannot be calculated by high-resolution ray tracing algorithms, the normalized power of the ray tracer is smaller than for the real-life measurements. Moreover, the dielectric parameters of the materials are estimated and may differ in real environments.

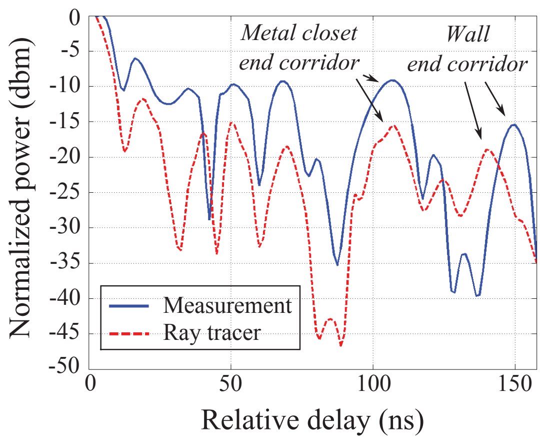

Figure 4.4: Comparison of $P_h(\tau)$ obtained by the channel sounder measurement and calculated using the ray tracing algorithm for one cycle in interval BC for the F2F link

The ray tracing algorithm shows that the last two dominant peaks for the *F2F* link are caused by multipath components that reflect on the metal closet and on the walls at the end of the corridor, as shown in Fig. 4.2, leading to decreasing delays when both firefighters are moving towards these reflectors, as in interval BC. For the *B2B* link, the ray tracing algorithm indicates that the last dominant multipath component corresponds to reflections on the window in the staircase leading to increasing delay and path loss when both firefighters are walking away from these reflectors, in the positive X-direction. For the *F2B* link, $P_h(\tau)$ changes dramatically over time due to multiple reflections, diffractions and scattering. In contrast, for the *B2F* link, one multipath component remains constant over time as shown in Fig. 4.3C. The latter multipath component has a fairly constant delay because both firefighters are walking in the positive X-direction (as indicated in Fig. 4.2) at equal speeds, in a situation where the signal propagation occurs via double reflection on objects situated behind and in front of of the TX firefighter in the floor plan. Note that the power and delay of both the dominant path and multipath components vary over time, depending on the constantly changing mutual orientation and relative distance between the RX and the TX firefighters.

RMS delay spread

The RMS delay spread τ_{RMS} indicates the time domain spread of multiple delayed copies of the transmitted pulse arriving at the RX firefighter. It is calculated for every of the 4650 measurement cycles, for all four body-to-body links separately. Define L the number of distinct multipath components, P_l the (linear) power of a multipath component and τ_l the corresponding delay of that multipath component, such that the RMS delay spread τ_{RMS} is calculated via the mean delay $\bar{\tau}$ as [11]:

$$\bar{\tau} = \frac{\sum_{l=1}^{L} P_l.\tau_l}{\sum_{l=1}^{L} P_l}, \tag{4.1}$$

$$\tau_{RMS} = \sqrt{\frac{\sum_{l=1}^{L} P_l.(\tau_l - \bar{\tau})^2}{\sum_{l=1}^{L} P_l}}. \tag{4.2}$$

The excess delay τ_{excess} is defined as the difference in delay between the first and last arriving multipath of $P_h(\tau)$. It is calculated as:

$$\tau_{excess} = \tau_L - \tau_1. \tag{4.3}$$

Since τ_{RMS} not only depends on the delay but also on the power of the multipath components, it is important to define the power ratio, in dB, as the ratio of the direct path power P_1 to the power summed over the other multipath components P_l, extracted from $P_h(\tau)$.

$$PR = 10.\log_{10}\left(\frac{P_1}{\sum_{l=2}^{L} P_l}\right) \tag{4.4}$$

By considering the power ratio, it is possible to distinguish indoor scenarios that lead to high and low τ_{RMS} values, such as in the interval BC for the F2B and the

B2F link. As shown on Fig. 4.3B, for the F2B link, where the TX front and RX back antenna are pointing away from each other, a lot of multipath components are present in interval BC. The powers of these multipath components are only slightly smaller than the power of the dominant path, leading to a small power ratio and a large excess delay, which causes a high RMS delay spread, as shown in Fig. 4.5 and numerically described in Table 4.1. In the same interval BC, the opposite holds for the B2F link, where the TX back antenna is directly pointing towards the RX front antenna. Now, the dominant, direct path is clearly stronger than the power in the multipaths, corresponding to a high mean power ratio. Together with the smaller excess delay, this leads to a smaller τ_{RMS} in interval BC. When comparing the F2F and F2B link, we clearly notice the influence of the power ratio on τ_{RMS}. Despite the fact that the excess delay is approximately equal, the lower PR for the F2B link leads to a RMS delay spread that is 62% higher than for the F2F link, as described in Table 4.1.

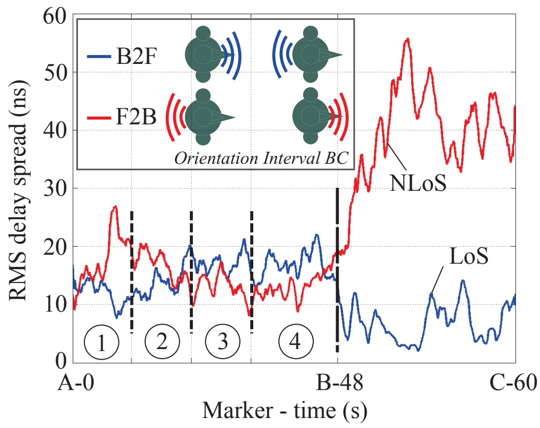

Figure 4.5: RMS delay spread over time for the B2F and F2B link

Fig. 4.5 also shows that, in interval AB, τ_{RMS} is low and approximately constant due to the lack of strong multipath components. Also note that τ_{RMS}, in Fig. 4.5, is obtained by using a running average filter over 77 consecutive samples, corresponding to one second of measurement, in order to prevent a heavily varying τ_{RMS} and to ensure that the trends are clearly visualized for all intervals.

Table 4.1: Mean power ratio, mean excess delay and mean RMS delay spread for interval BC

	$\overline{PR}(dB)$	$\overline{\tau}_{excess}(ns)$	$\overline{\tau}_{RMS}(ns)$
F2F	1.94	204	24.09
F2B	-5.51	201	39.18
B2F	14.61	115	6.85
B2B	2.32	159	18.11

Previous extensive wideband indoor channel measurements, described in [12], show that τ_{RMS} is environment- and frequency dependent with values generally below 30 ns, except for very large rooms with large distances between potential reflectors, as is the case in our indoor environment. A more general rule of thumb indicates that τ_{RMS} is above 10 ns and under 50 ns [11] which largely matches the results presented in Fig. 4.6, presenting the CDFs of τ_{RMS} for all four body-to-body links, over the complete measurement duration.

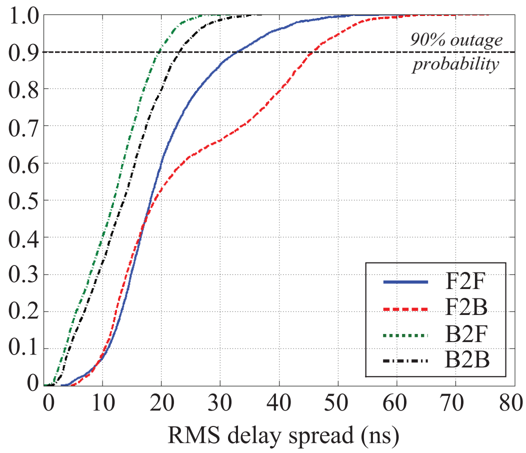

Figure 4.6: CDF of τ_{RMS} over the compelete measurement for all four body-to-body links

For this indoor scenario, τ_{RMS} is above 1.71 ns and below 58.02 ns during 98% of all measurement cycles. Large variations in τ_{RMS} occur due to the constantly changing mutual orientations and the relative positions of both firefighters, as well as the varying distance between the two firefighters. The small τ_{RMS} values are caused by sporadic high values of the power ratio (> 15dB), for example at the starting point (marker A) where the back antennas of both firefighter are close to each other, or by extremely low values of the excess delay (< 50 ns). Low values for the excess delay sometimes occur when the received signal is very weak, leading to a dominant peak power only few dB above the noise floor. This leads to only a few multipath components exceeding the noise floor and hence to a small excess delay and a small τ_{RMS}. For further calculations in Section 4.4, we make use of the 90% outage probability level, $\tau_{RMS,90}$, defined as the maximum RMS delay spread during 90% of the time and these values are numerically described in Table 4.2.

50% correlation bandwidth

If the calculated τ_{RMS} is not significantly smaller than the symbol duration T_S, strong multipath components of symbol X_n could influence symbol X_{n+1}, leading to Inter Symbol Interference (ISI). Moreover, delayed multipaths, arriving at the

RX firefighter, introduce frequency-selective fading, which is analyzed by observing the correlation between received signals at two different frequencies [11]. In this case, the frequency correlation function is given by the Fourier Transform of $P_h(\tau)$:

$$R_T(\nu) = \int_0^{\tau_{max}} P_h(\tau).e^{-j2\pi\nu f\tau}.d\tau. \tag{4.5}$$

In this chapter, the 50% correlation bandwidth $B_{C,0.5}$ is defined as the minimal bandwidth separation, resulting in 50% decorrelated signals. Note that, since the useful channel sounder bandwidth is equal to 120 MHz and the 50% correlation bandwidth is defined single-sided, the maximum computable bandwidth separation is limited to 60 MHz in our measurement setup.

If the indoor body-to-body channel only exhibits few weak multipath components, the wideband channel is almost frequency-flat and the frequency separation is large ($>$ 60MHz). This is happening in the dashed red line in Fig. 4.7. In contrast, if the indoor body-to-body channel is composed of a lot of strong multipath components, corresponding to low power ratios, the frequency selectivity of the wideband channel increases because the delayed multipaths interfere with each other. This leads to smaller frequency separation to ensure 50% decorrelation, as happening for the solid blue line shown in Fig. 4.7, corresponding to to 13.81 MHz frequency separation for a Power Ratio equal to -6.89 dB.

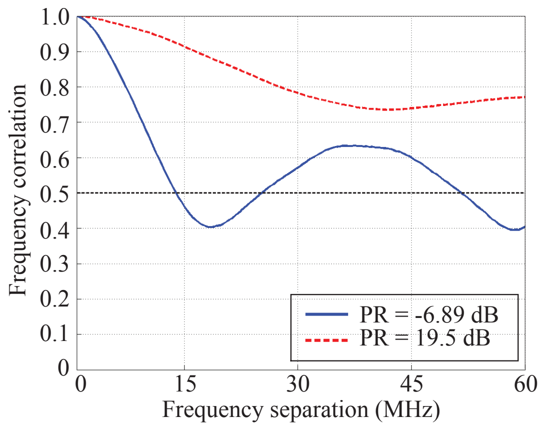

Figure 4.7: Frequency correlation for two measurement cycles from the F2F link leading to a high and low Power Ratio (PR)

Fig. 4.8 shows the CDFs of $B_{C,0.5}$ for all four body-to-body links over the complete measurement. As stated before, the maximum computable $B_{C,0.5}$ is limited to 60 MHz because the useful Elektrobit channel sounder bandwidth is equal to 120 MHz. For further calculations in Section 4.4, we define the 10% outage probability level, $B_{C,0.5,10}$ as the minimum 50% correlation bandwidth during 90% of the time. These values are numerically described in Table 4.2.

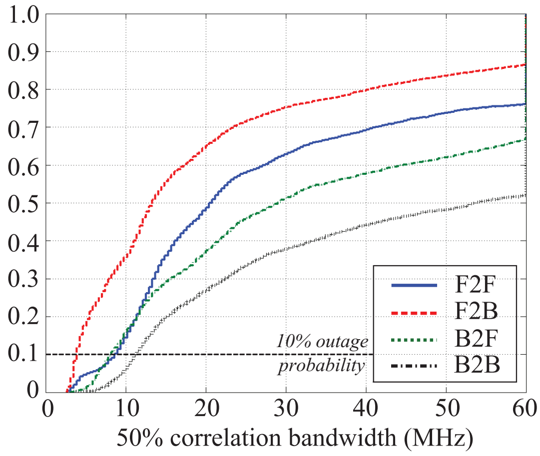

Figure 4.8: CDF is $B_{C,0.5}$ over the complete measurement for all four body-to-body links

Table 4.2: 90% outage probability of the RMS delay spread ($\tau_{RMS,90}$), 10% outage probability of the 50% correlation bandwidth ($B_{C,0.5,10}$) and mean α

	F2F	F2B	B2F	B2B
$\tau_{RMS,90}(ns)$	33.07	45.80	19.69	23.18
$B_{C,0.5,10}(MHz)$	8.62	3.92	11.37	8.24
$\bar{\alpha}$	3.28	4.30	3.56	4.55

As a final step of the wideband body-to-body channel characterization, we calculate the parameter α which describes the inverse relationship between τ_{RMS} and $B_{C,0.5}$. Its value depends on the environment as well as on the power ratio:

$$\alpha = \frac{1}{\tau_{RMS}.B_{C,0.5}}. \tag{4.6}$$

Table 4.2 presents the mean α over all 4650 measurement cycles. Since α is generally between 1 and 10 for indoor environments [12], these values indicate that the wideband, indoor body-to-body channel parameters are within the normal range.

4.4 Long Term Evolution (LTE)

In this section, we analyze whether the LTE standard, and, by extension, the LTE-D2D standard, would be suitable for an indoor body-to-body communication channel. As explained in Section 4.3, the symbol duration T_s should be sufficiently larger than the RMS delay spread to avoid ISI. However, increasing the symbol duration T_s results in a lower data rate, which limits the possibility to transmit multimedia or real-time on-body sensor data. Therefore, the frequency-selective wideband channel is subdivided into N orthogonal and low-data rate subcarriers, which enlarges the total data rate and avoids ISI by inserting a cyclic prefix between two succesive OFDM symbols on one subcarrier.

Define CP_{min} to be the minimum cyclic prefix length that prevents ISI on all subcarriers for all four body-to-body link during (at least) 90% of the time. Based on the maximum RMS delay spread, the minimal cyclic prefix length is generally calculated as [13]:

$$CP_{min} = 3.\tau_{RMS,max} = 137.4ns. \tag{4.7}$$

This cyclic prefix length is compatible with the LTE standard, which sets the cyclic prefix length equal to 4.69 μs [14], being larger than the CP_{min}.

4.5 Conclusion

This chapter presents a detailed wideband indoor body-to-body channel characterization by means of channel sounder measurements and a ray tracing algorithm. The ray tracing results show good agreement with the actual measurement results which indicates that our simplified indoor office model is reliable and, hence, useful to further investigate indoor body-to-body propagation. The results of the measurement campaign show that, the LTE, and, by extension, the LTE-D2D standard is a potential standard for public safety indoor body-to-body networks, a purpose for which it was originally not designed.

In contrast to a cellular based network, an indoor body-to-body link is subject to fading and body shadowing at both ends of the link with additional highly variable signal fluctuations due to the constant reorientation of both members of the Rapid Intervention Team. It is of great interest to see that the LTE standard, designed for communication with a fixed access point, is also suitable for indoor communication between two simultaneously moving firefighters, experiencing these difficult radio propagation conditions.

Acknowledgment

The authors would like to thank IAP BESTCOM and UCL for providing the Elektrobit channel sounder and measurement locations.

References

[1] “ITU-R”, Digital Land Mobile Systems for Dispatch Traffic, Tech. Rep., 2012.

[2] “LTE-Advanced Evolution in Releases 12 - 14”, Nokia Solutions and Networks white paper, Tech. Rep., 2015.

[3] “Public safety mobile broadband”, Ericsson white paper, Tech. Rep., 2014.

[4] T. Doumi, M. Dolan, S. Tatesh, A. Casati, G. Tsirtsis, K. Anchan, and D. Flore, “LTE for public safety networks”, *Communications Magazine, IEEE*, vol. 51, no. 2, pp. 106–112, Feb. 2013.

[5] X. Lin, J. G. Andrews, A. Ghosh, and R. Ratasuk, “An overview on 3gpp device-to-device proximity services”, *Communications Magazine, IEEE*, vol. 51, no. 2, pp. 106–112, Apr. 2014.

[6] S. Cotton and W. Scanlon, “Channel characterization for single- and multiple-antenna wearable systems used for indoor body-to-body communications”, *IEEE Transactions on Antennas and Propagation*, vol. 57, no. 4, pp. 980–990, Apr. 2009.

[7] K. Ghanem, “Effect of channel correlation and path loss on average channel capacity of body-to-body systems”, *IEEE Transactions on Antennas and Propagation*, vol. 61, no. 12, pp. 6260–6265, Dec. 2013.

[8] Q. Wang, K. Masami, and J. Wang, “Channel modeling and BER performance for wearable and implant UWB body area links on chest”, in *Proceedings of the International Conference on Ultra-Wideband (ICUWB)*, Vancouver, Canada: IEEE, Sep. 2009, pp. 316–320.

[9] S. Lemey and H. Rogier, “SIW textile antennas as a novel technology for UWB RFID tags”, in *Proceedings of RFID Technology and Applications Conference (RFID-TA)*, Tampere, Finland: IEEE, Sep. 2014, pp. 256–260.

[10] (). AWE Communications: Wave propagation and radio network planning, [Online]. Available: `http://www.awe-communications.com/`.

[11] R. Janaswamy, *Radiowave Propagation and Smart Antennas for Wireless Communications (The Springer International Series in Engineering and Computer Science)*. Springer, 2000, ISBN: 978-0-30-646990-9.

[12] G. Janssen, P. Stigter, and R. Prasad, “Wideband indoor channel measurements and ber analysis of frequency selective multipath channels at 2.4, 4.75, and 11.5 ghz”, *IEEE Transactions on Communications*, vol. 44, no. 10, pp. 1272–1288, Oct. 1996.

[13] A. Goldsmith, *Wireless Communications*. Cambridge University Press, 2005.

[14] "3GPP LTE: Introducing Single-Carrier FDMA", Agilent Technologies, M. Rumney, Tech. Rep., 2008.

5

Capacity of Broadband Body-to-Body Channels between Firefighters wearing Textile SIW Antennas

Thijs Castel, Patrick Van Torre, Luigi Vallozzi, Marina Marinova, Sam Lemey, Wout Joseph, Claude Oestges and Hendrik Rogier

Accepted for publication in IEEE Transactions on Antennas and Propagation,
Vol. 64, No. 05

★ ★ ★

Reliable, high-data rate indoor communication is essential to transfer crucial information between firefighters for improving their safety and decreasing the number of casualties caused by indoor fires. Since electronic monitoring systems, including antennas implemented inside the firefighter jacket, should provide high data rates, communication over a wideband channel is required. We study an 80 MHz-wide body-to-body channel at 3.6 GHz between two firefighters of a Rapid Intervention Team performing the primary search for victims, by static and dynamic channel sounder measurements. Two Ultra-Wideband Substrate Integrated Waveguide cavity-backed slot textile antennas were unobtrusively deployed in the front and the back sections of the firefighters' jackets, providing up to 2×2 *MIMO communication. We calculate the achievable SISO-, SIMO-, MISO- and MIMO-OFDM capacities for realistic indoor broadband body-to-body communication channels between two firefighters. Furthermore, we analyze implementations of one-dimensional spatial waterfilling and two-dimensional space-frequency waterfilling, studying their ability to further enhance transmission of live sensor data, pictures or videos between mobile firefighters.*

5.1 Introduction

In 2012, according to the International Association of Fire and Rescue Services [1], residential, indoor fires are the major origin of fire, both country-wide (49.5%) and restricted to cities (50.9%). Additionally, in the year 2012 alone, thirteen US firefighters died in an indoor environment [2]. Previous numbers demonstrate the necessity of reliable indoor communication between rescue workers, at high data rates, in potentially life-threatening situations. Such a wireless communication system increases the rescue workers' safety by providing efficient communication of crucial information, such as sensor data, pictures or videos. Moreover, state-of-the-art off-body communication has the potential to reduce costs, damage, time of operation and the number of injured or deaths. Furthermore, a body-to-body MIMO scenario is expected to be of great importance, especially from the practical point of view, for next generation communication systems that will see an integration of antennas and devices into fabrics.

In this chapter, the first detailed analysis of the wideband body-to-body wireless channel is presented between high-performance Ultra-Wideband (UWB) cavity-backed Substrate Integrated Waveguide (SIW) textile antennas integrated in the rescue workers' garments. Based on these channel sounding measurements, detailed wideband channel information, such as high-resolution power delay profiles, is analyzed and interpreted for the first time. The channel sounding experiment was performed during the accurate replication of a real firefighter intervention, corresponding to the primary search of a Rapid Intervention Team (RIT) [3]. During the measurements, all procedures and techniques performed during a real intervention were carefully reproduced in real-time, such that the effect of body postures, relative orientation and distance between the two members of the RIT are reflected in the channel data. The specific contributions are:

1. The relevant Orthogonal Frequency Division Multiplexing (OFDM) parameters are determined for both the static and dynamic body-to-body wireless channel between 2×2 on-body UWB-SIW antennas.

2. Next, the achievable SISO-, SIMO-, MISO- and MIMO-OFDM capacities are evaluated for the first time for realistic broadband body-to-body communication channels with 80 MHz bandwidth.

3. The scenario where channel feedback is available is analyzed in detail, enabling one-dimensional spatial and two-dimensional space-frequency waterfilling. It is proven that, for the considered scenario, both the one- and two-dimensional waterfilling capacity gains are relatively small compared to the capacity obtained by simple, uniform MIMO.

From the measurement campaign and subsequent channel characterization, we conclude that 2×2 MIMO is largely sufficient for efficient communication of live sensor data, pictures or videos between two firefighters during an intervention, and that channel feedback and MIMO waterfilling schemes are not needed to achieve the necessary data throughput and channel reliability. Although the measurements are performed using an Elektrobit channel sounder operating at 3.6 GHz center frequency with 80 MHz bandwidth, the results can be extended to both the lower 2.45 GHz Industrial, Scientific and Medical (ISM) band [4] and the higher 5 GHz Wi-Fi band [5], making them applicable to wideband channels in the IEEE 802.11ac [6] and IEEE 802.11n [7] standards. In addition, they provide insight into the performance of other networks that occupy less bandwidth, such as WiMax [8]. First, a static Non-Line-of-Sight (NLoS) corridor-to-office measurement was performed, followed by a dynamic measurement with both firefighters moving simultaneously in the office environment, replicating a real-life rescue operation. For both measurements, two wearable UWB-SIW antennas are unobtrusively and invisibly deployed inside each firefighter's jacket, implementing up to 2×2 MIMO communication.

A lot of work has been performed to improve the reliability and to increase the channel capacity for body centric communication [9],[10] in Wireless Body Area Networks (WBAN's) [11]–[14]. MIMO channels may provide significant capacity and diversity gain in narrowband *on-body* communication channels [15]–[17]. For narrowband *off-body* links, MISO provides diversity gain when the two off-body channels are sufficiently decorrelated [18]. Moreover, SIMO [19],[20] and MIMO [21],[22] increase reliability and performance. In wideband personal area networks, the potential use of MIMO to enhance performance is revealed in [23]. Also for static wideband channels, MIMO-OFDM has been extensively studied, for several orders of MIMO systems in [24]–[30]. Yet, applied to WBANs, only [31] simulates performance gain when improving from SISO Multiband (MB)-OFDM over MISO- to MIMO MB-OFDM from a body-surface node to an external node. In [32], the optimum on-body locations for static and pseudo dynamic scenarios are determined for an MB-OFDM UWB body-centric wireless network. Yet, no research on MIMO capacity gain was performed. When focusing on *body-to-body* communication, [33] presents a comprehensive statistical characterization for narrowband dynamic body-to-body communication channels at 2.45 GHz. Furthermore, receive diversity, yielding 8.69 dB diversity gain, is successfully implemented by combining four receiver branches using Maximal Ratio Combining (MRC). Also in [34], channel gains, small-scale fading and large-scale fading are statistically described for narrowband, indoor body-to-body communication channels at 2.45 GHz. Channel characterization of the wideband body-to-body transmissions by means of static and dynamic measurements, not replicating real life rescue scenarios, is described in [35]. In contrast to this chapter, no MIMO-OFDM capacity calculations were performed and the directional stacked patch antennas were mounted on the human body instead of unobtrusively integrated into the clothing. Ref. [36] calculated the average channel capacity of body-to-body systems, with different printed PCB antenna systems placed on the human body. However, due to the user's stringent requirements in terms of wearability and comfort, the rigid PCB antennas should be compact when placed on the human body. In contrast, flexible textile antennas exploit the large surface provided by the clothing to optimize the antenna dimensions, without affecting user's comfort, to maximize both the isolation from the human body and the Front to Back Ratio (FBRT). Moreover, since this design strategy ensures that power is radiated away from the human body, flexible textile antennas are safer and more energy efficient, making them more suitable for body-centric communication. Additionally, [36] only investigated the narrowband MIMO channel at 2.45 GHz, which does not allow to evaluate OFDM and its specific wideband parameters in the specific rescue workers scenario under study.

To our knowledge, this is the first MIMO-OFDM capacity analysis for realistic indoor broadband body-to-body communication channels between two simultaneously moving firefighters in an office environment. The chapter is structured as follows. Section 5.2 details the measurement setup while Section 5.3 describes the calculated OFDM parameters and the theoretic OFDM capacity calculations. Section 5.4 presents the results and, finally, the conclusions are drawn in Section 5.5.

5.2 Measurement setup

Let us first describe the implemented UWB-SIW textile antennas, followed by the outline of both the static and dynamic measurement scenarios. Finally, the Elektrobit channel sounder settings are discussed.

5.2.1 Ultra-Wideband SIW textile antenna

Both the TX and RX firefighters are equipped with two UWB-SIW textile antennas, unobtrusively integrated inside their firefighter jacket in the front and back sections, as shown in Fig. 5.1. The antenna locations were chosen to guarantee minimal influence on antenna characteristics caused by movement and equipment worn by the firefighter during interventions, such as the oxygen bottle and buckles. Moreover, the rear antenna is vital for transmitting and receiving signals when the firefighter lies, face down, on the floor and his body is completely blocking the front antenna [37].

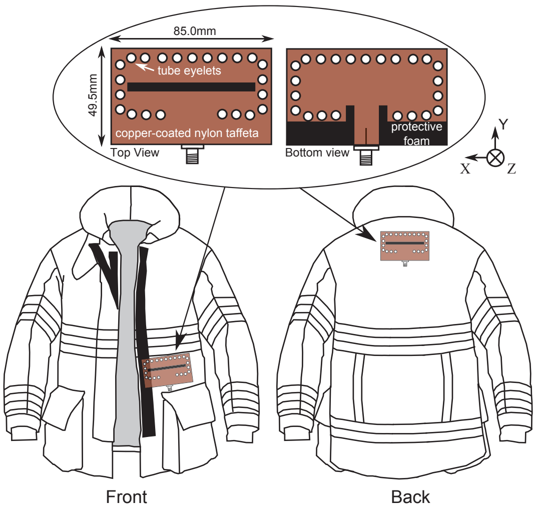

Figure 5.1: Front and back locations of the integrated UWB-SIW textile antenna, for both the TX and RX firefighter, applied for the broadband indoor body-to-body measurements. In the actual measurements, the UWB-SIW textile antennas are effectively integrated inside the firefighter jackets, between the inner liner and the thermal/moisture barrier.

UWB-SIW cavity backed slot antennas [38] provide excellent antenna-to-human body isolation as they mainly radiate in the hemisphere pointing away from the human body, whereas radiation towards the human body is minimized. This leads to a higher radiation efficiency, on the one hand, and stable antenna characteristics at different on-body locations, on the other hand. In addition, [38] also proves that the antenna maintains its excellent performance under bending, as could be the case in harsh environments, such as during rescue operations. Furthermore, they guarantee a stable and high radiation efficiency over a very large -10 dB impedance bandwidth. Additionally, next to the low-cost production process, the material inside the firefighter jackets is reused as antenna substrate, limiting the cost of such an integrated textile cavity-backed slot antenna to the cost of the copper-coated nylon taffeta electro-textile and the copper eyelets, which act as an effective electric wall in the antenna design. Finally, they are low-profile, lightweight and flexible, and, therefore easily deployable inside the firefighter jacket.

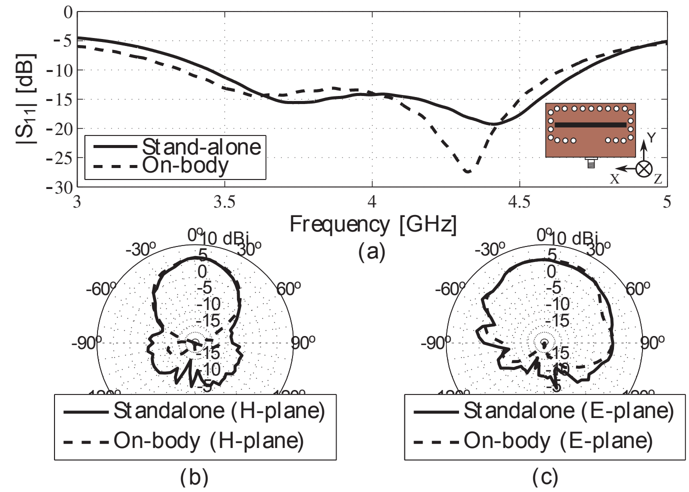

Figure 5.2: (a) Measured free space and on-body |S11|, with respect to 50 Ω, (b) Measured stand-alone and on-body radiation patterns in the H-plane (XZ-plane), (c) Measured stand-alone and on-body radiation patterns in the E-plane (YZ-plane), at 3.6 GHz

First, we assess the antenna's stand-alone and on-body performance in free-space conditions in an anechoic room using an Agilent N5242A PNA-X Network analyzer. For the on-body scenario, the real-life scenario was emulated where the SIW antenna is deployed inside the front section of the firefighter jacket, worn by a 1.80 meter high male test person.

Fig. 5.2(a) depicts both the return loss characteristics of the stand-alone antenna and the on-body setup, indicating that the human body is 'invisible' to the antenna, leading to stable and reliable performance for different on-body positions, as also shown in [38]. The stand-alone antenna is matched in the frequency band ranging from 3.35 GHz to 4.64 GHz, corresponding to a -10 dB bandwidth of 1.29 GHz. For the on-body scenario, the antenna is matched from 3.45 GHz to 4.72 GHz, corresponding to a similar -10 dB bandwidth of 1.27 GHz. The same measurement setups, combined with an Orbit/FR positioning system, were replicated to measure both the stand-alone and on-body radiation pattern at 3.6 GHz. Figs. 5.2(b) and 5.2(c) depict both the measured stand-alone and on-body radiation patterns in the H- and E-plane, respectively. Note that, the stand-alone and on-body radiation patterns are in good agreement because the SIW antenna minimizes backside radiation while strongly radiating in the opposite hemisphere. This leads to similar gains along broadside, equal to 6.11 dBi and 5.94 dBi for the stand-alone and on-body scenario, respectively. The backside radiation for the on-body SIW antenna is reduced due to the presence of the human body, which absorbs radiation. However, since backward radiation is already very small in both setups, the difference is only marginal. Due to the larger slot dimensions in the XZ-direction compared to the YZ-direction, as visible in Fig. 5.1, the SIW antenna is more directive in the H-plane, leading to 3 dB beamwidth equal to 53° and 103° in the H-plane and E-plane, respectively. More measurement results and detailed antenna dimensions are extensively described in [38].

5.2.2 Scenarios

Static scenario

In real-life rescue operations, one firefighter is scanning the corridor while the other firefighter is scanning the offices, looking for potential victims. This implies that, most of the time, the firefighters have to deal with a Non Line of Sight (NLoS) scenario such as a corridor-to-office scenario. Therefore, first, a static NLoS measurement, as shown in Fig. 5.3, was performed in which the TX firefighter was standing at the beginning of the corridor with his front antenna pointing along the positive X direction and the RX firefighter was standing in office 2 with an open door and his front antenna pointing along the positive Y direction towards the office entrance.

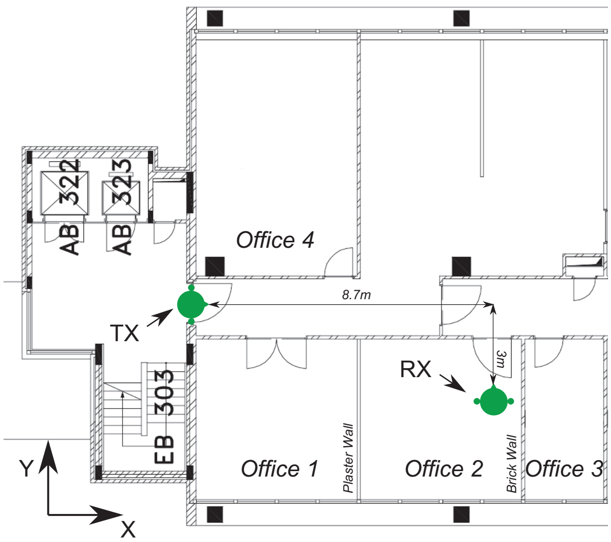

Figure 5.3: Static corridor-to-office NLoS scenario

Dynamic scenario

Second, mobile measurements were performed with both firefighters simultaneously moving around as part of a Rapid Intervention Team (RIT) performing the primary search, looking for victims, in an office floor of a building [3]. We focus on the communication between the members of this RIT team, typically composed of two to four firefighters, operating on the same floor, in each other's vicinity. The replicated real-life primary search operation, according to the ”two-in, two-out” principle, involves an intervention where two firefighters are entering a building in which the first firefighter immediately starts scanning the hallway, using the hand-search technique described in [39], while the second firefighter starts scanning the offices using the same technique. For this dynamic measurement scenario, the simplified floor plan and the TX and RX firefighter trajectories are shown in Fig. 5.4. Applied to a real-life rescue operation, the TX firefighter, whose path is marked by the long dashed line, is scanning the hallway while the RX firefighter, whose path is marked by the short dashed line, is simultaneously scanning the offices. The markers A to H, placed along the TX firefighter path as well as on the RX firefighter trajectory, show where both firefighters are located at the same time instance during the measurement.

For example, at marker B, the RX firefighter leaves office 1 while the TX firefighter is approximately in the middle of the hallway. The subintervals ① to ④, further used to indicate specific scenarios of the dynamic measurements, correspond to different propagation phenomena depending on the mutual position and orientation of both firefighters. Practically, the RX channel sounder is positioned in a fixed location and is connected to the RX firefighter, providing sufficient cable length to cover the complete path. The TX channel sounder is also connected by means of cables to the TX firefighter but the equipment is moving along with the walking TX firefighter by means of a third person pushing the cart. Special care was taken that this third person is located sufficiently far away from both the TX and RX firefighter during the complete measurement, such that he is not influencing the measurements.

5.2.3 Channel sounder settings

The measurements are performed by the UCL-ULB Elektrobit channel sounder, connected to multiple TX and RX antennas, as used in [40]. The channel sounder is based on a switched-array and uses an up-converted and phase-modulated pseudonoise sequence to probe the channel. At the receiver side, after down conversion and demodulation, Channel Impulse Responses (CIRs) are obtained [41]. The Rubidium standard stabilized local oscillators inside both multi-antenna units are synchronized by first minimizing the phase rotation and then performing a time-tag synchronization during which a common absolute time reference is given to both units. Table 5.1 lists the applied channel sounder settings.

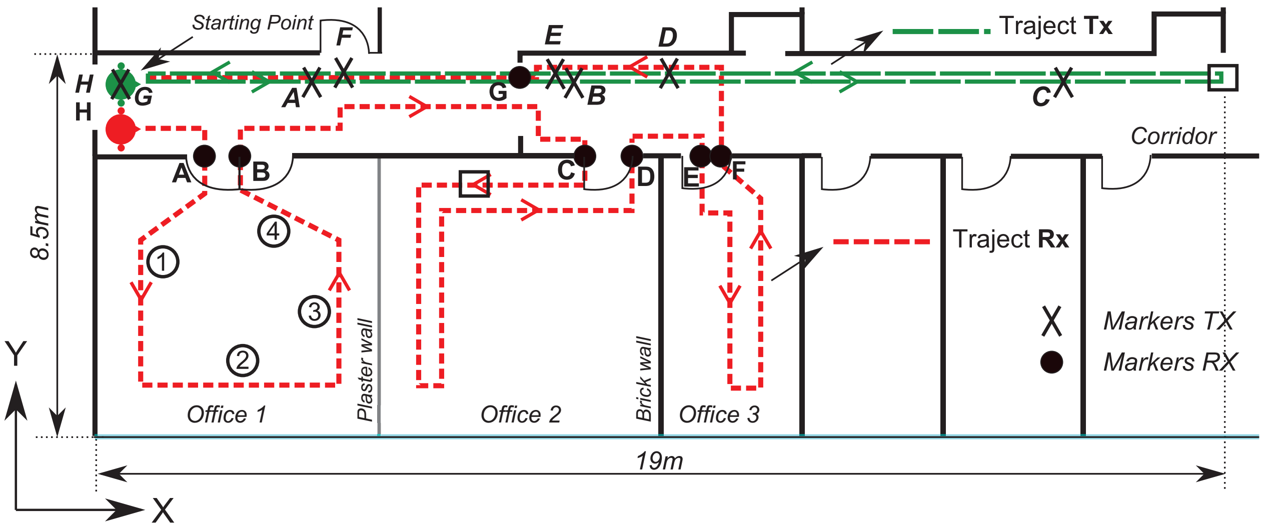

Figure 5.4: Simplified floor plan with the dynamic measurement scenario

Table 5.1: Channel sounder settings

Center frequency	3.6 GHz
Bandwidth	200 MHz
Useful bandwidth	120 MHz
Delay resolution	2.5 ns
Code length	255 chips
# Samples/chip	4
# Samples/code	1020
Maximum delay	2.550 μs
# TX Antennas	2
# RX Antennas	2
Scan array time	102 μs
Channel sample rate	75.75 Hz
Transmit power	100 mW

Unfortunately, our channel sounder can only be tuned to a carrier frequency between 3.6 GHz and 4.2 GHz. Therefore, we have fixed the center frequency to 3.6 GHz, which is, on the one hand, an operating frequency for (indoor) WiMax [42], and, on the other hand, approximately in the middle of the 2.45 GHz ISM band, supporting the 802.11n standard, and the 5G Wi-Fi band, supporting both the 802.11n and 802.11ac standard. Moreover, the Federal Communication Commission (FCC) has recently proposed the 3.5 GHz for both licensed and unlicensed Broadband Radio services with 150 MHz bandwidth, Priority Access and interference protection [43]. The specific characteristics, which enable increased speed, capacity and adaptability, make this ”3.5 GHz band of Innovation” also a potential candidate for future Indoor Public Safety Networks. During measurements, the transmit power was chosen equal to 100 mW to obtain reliable channel measurements. However, for all calculations, the measurement results are rescaled for a transmit power of 1.5 mW, as this corresponds to the required power to ensure that the received Signal to Noise Ratio (SNR) on all four SISO links exceeds 5 dB during 90% of the time, guaranteeing reliable timing synchronization and frequency offset estimation in the MIMO-OFDM system [44]. Moreover, this critical SNR level allows reliable demodulation and detection on a practical receiver.

5.3 Calculations

5.3.1 OFDM parameters

In wireless communication, to avoid Inter Symbol Interference (ISI), the symbol duration T_S should be chosen sufficiently larger than the RMS delay spread τ_{RMS}, which is extracted from high-resolution power delay profiles. One such profile is shown in Fig. 5.5, for the back-to-back link in the dynamic measurement scenario (interval AC).

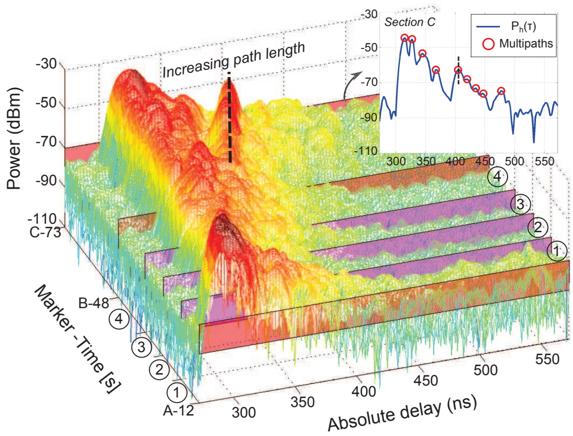

Figure 5.5: Time-varying power delay profile $P_h(\tau)$ for the back-to-back link in the dynamic measurement scenario (interval AC), together with $P_h(\tau)$ at position C.

However, increasing T_S leads to a decreasing data rate, which is a major drawback when firefighters need to transmit live sensor data, pictures or video. Therefore, to increase capacity while still preventing ISI, the wideband body-to-body channel, which experiences frequency-selective fading, can be subdivided into N subcarriers. The spacing between these orthogonal subcarriers is further defined as Δf.

To ensure that consecutive symbols on one subcarrier do not interfere, the cyclic prefix CP should be chosen larger than three times τ_{RMS}, calculated using the mean delay $\bar{\tau}$ as [45]:

$$\bar{\tau} = \frac{\sum_{l=1}^{L} P_l \, \tau_l}{\sum_{l=1}^{L} P_l}, \tag{5.1}$$

$$\tau_{RMS} = \sqrt{\frac{\sum_{l=1}^{L} P_l \, (\tau_l - \bar{\tau})^2}{\sum_{l=1}^{L} P_l}}. \tag{5.2}$$

Yet, inserting a cyclic prefix in an OFDM symbol causes overhead, given by

$$O_v = \frac{CP}{T_s}, \tag{5.3}$$

with the total OFDM symbol time determined as

$$T_s = CP + \frac{1}{\Delta f}. \tag{5.4}$$

For both the static measurement, based on 5000 measurement cycles over 65 seconds, and the dynamic measurement, relying on 15000 measurement cycles over 197 seconds, τ_{RMS} is calculated for the four SISO body-to-body communication links: front-to-front (F2F), front-to-back (F2B), back-to-front (B2F) and back-to-back (B2B). However, for a practical implementation, only one value for the cyclic prefix can be chosen, in the static or dynamic scenario. The selected value prevent ISI, during 99% of the time, in all four SISO links. Therefore, a stringent limit, being the largest CP of the four SISO links, results in the OFDM parameters described in Table 5.2.

Table 5.2: Calculated OFDM parameters for the static and dynamic scenario

	CP	T_S	O_v
Static	84.93 ns	1.680 μs	5.06%
Dynamic	150.03 ns	3.335 μs	4.50%

Note that, since the indoor scattering mechanisms for 2.4 GHz and 5.2 GHz are proven very similar [46], the calculated channel parameters may be extrapolated to the lower ISM band and the higher Wi-Fi band, as also proven in [47] for a wide range of frequencies. Moreover, taking into account the limited mutual distance between both firefighters, the Free Space Path Loss (FSPL) only slightly increases when operating in the higher Wi-Fi band, compared to the channel sounder measurements at 3.6 GHz. This implies that the MIMO-OFDM channel capacity will be similar, although a slight decrease in range is possible when extending the results to the higher 5G Wi-Fi band, supporting both the 802.11n and 802.11ac standard. Logically, the results can also be extrapolated to the IEEE 802.11n standard, operating in the 2.45 GHz ISM band, given the decreased FSPL.

5.3.2 IEEE 802.11n/ac

In both the wideband 802.11n and 802.11ac standard, the OFDM subcarrier bandwidth is equal to 312.5 kHz and the smallest OFDM cyclic prefix length is equal to 400 ns, which is sufficient for this indoor office scenario. The length of the cyclic prefix is fixed, and not changed in an adaptive manner, because no channel delay information is available via common, simple channel feedback techniques. The 802.11n/ac OFDM parameters fulfill the requirements resulting from our channel sounding campaign, indicating the possibility to successfully implement the 802.11ac standard for broadband body-to-body links in a typical indoor environment. To assess the performance in a practical implementation, the OFDM capacity is calculated using the 802.11n/ac subcarrier bandwidth and cyclic prefix, leading to an OFDM symbol time T_s equal to 3.6 μs and an overhead O_v equal to 11%. The dynamic range of the channel sounder limits the useful OFDM bandwidth to 120 MHz. Therefore, we calculate the OFDM capacities for an OFDM bandwidth equal to 80 MHz, which is the highest achievable bandwidth compatible with the 802.11ac standard.

5.3.3 OFDM Capacity

In this chapter, the wideband indoor body-to-body channel is subdivided into 256 frequency-flat subcarriers having different capacities, depending on the Signal to Noise Ratio (SNR) at the receiver. The number of subcarriers depends on the OFDM bandwidth and on the subcarrier bandwidth Δf. It is found to be:

$$N = \left\lceil \frac{B}{\Delta f} \right\rceil = \left\lceil \frac{80MHz}{312.5kHz} \right\rceil = 256. \tag{5.5}$$

Let P_k define the transmit power allocated to subcarrier k, σ^2 the noise power, $\mathbf{H_k}$ the channel matrix of subcarrier k, N_{TX} the number of transmit antennas, N_{RX} the number of receive antennas and O_v the overhead. Assuming constant TX power with constant power spectral density and assuming that the channel is unknown at the transmitter but perfectly known at the receiver, and therefore employing uniform power allocation, the SISO-, SIMO-, MISO- and MIMO-OFDM capacity per subcarrier k, in bps/Hz, is calculated as:

$$C_k = \log_2\Big(\det\Big[\mathbf{I}_{N_{RX}} + \frac{P_k}{N_{TX}.\sigma^2}.\mathbf{H_k}.\mathbf{H_k}^H\Big]\Big). \tag{5.6}$$

Equivalently, since the MIMO channel can be subdivided into r equivalent SISO spatial subchannels, with $r = \min(N_{TX}, N_{RX})$, the MIMO-OFDM subcarrier capacity C_k is also calculated as the sum of r equivalent SISO spatial subchannel capacities. These SISO spatial subchannel capacities are determined via eigenvalue decomposition of $\mathbf{H_k}.\mathbf{H_k}^H$, leading to a column vector of eigenvalues $\boldsymbol{\lambda}_\mathbf{k} = [\lambda_{1,k}\,\lambda_{2,k} \ldots \lambda_{r,k}]^T$. The equivalent MIMO-OFDM subcarrier capacity C_k, for uniform power allocation of P_k over the r equivalent SISO spatial subchannels, in bps/Hz, is calculated as:

$$C_k = \sum_{i=1}^{r} \log_2\Big(1 + \frac{P_k}{N_{TX}.\sigma^2}.\lambda_{i,k}\Big), \tag{5.7}$$

leading to exactly the same MIMO-OFDM subcarrier capacity C_k as (5.6). The eigenvalue decomposition, determined by the spatial correlation between the links from any transmit to any receive antenna, gives an indication of the possible multiplexing gain, per subcarrier, when applying MIMO-OFDM. This implies that the spatial multiplexing gain per subcarrier, when applying 2 × 2 MIMO, is largest if the two eigenvalues are equal, corresponding to fully uncorrelated spatial channels [48], and hence fully exploiting parallelism.

When the channel state information (CSI) is known at both receiver and transmitter, via channel feedback, the MIMO-OFDM capacity can be increased by applying waterfilling, allocating more power to the stronger subchannels [49], [50]. In case of one-dimensional spatial waterfilling, the power per subcarrier P_k is spread over r equivalent SISO spatial subchannels, with $r = \min(N_{TX}, N_{RX})$, allocating more power to the strongest spatial subchannel. As a first step, eigenvalue decomposition is performed on $\mathbf{H_k}.\mathbf{H_k}^H$, leading to a column vector of eigenvalues $\boldsymbol{\lambda}_{\mathbf{1D,k}} = [\lambda_{1,k}\ \lambda_{2,k}\ ...\ \lambda_{r,k}]^T$ with $\lambda_{1,k} > \lambda_{2,k} > ... > \lambda_{r,k}$. Then, the following algorithm is implemented for every subcarrier k [49]:

1. Set the iteration count p = 1
2. Calculate the water level as:

$$\mu = \frac{N_{TX}}{r-p+1}\Big[1 + \frac{1}{\sigma^2}\sum_{i=1}^{r-p+1}\frac{1}{\lambda_{i,k}}\Big] \tag{5.8}$$

3. Calculate the power allocated to the i^{th} spatial subchannel of subcarrier k, defined as:

$$\gamma_{i,k} = \Big(\mu - \frac{N_{TX}.\sigma^2}{P_k.\lambda_{i,k}}\Big) \tag{5.9}$$

   If now, $\min(\gamma_{i,k}) < 0$, set p = p +1 and go to step 2 in the algorithm.

When the algorithm ends, the power on each spatial subchannel of subband k is nonnegative, and the optimal power allocation, per subband, is found. The one-dimensional spatial waterfilling MIMO-OFDM capacity for subcarrier k, in bps/Hz, is calculated as:

$$C_{k,1\mathrm{D}} = \sum_{i=1}^{r}\log_2\Big(1 + \frac{P_k}{N_{TX}.\sigma^2}\gamma_{i,k}.\lambda_{i,k}\Big). \tag{5.10}$$

For two-dimensional space-frequency waterfilling, the total transmit power P_{TX} is spread over the r equivalent spatial subchannels for all N subcarriers at once, such that the power is optimally allocated over rN virtual parallel channels. Therefore, the total channel matrix $\mathbf{H}$ is calculated as a diagonal matrix of all subcarrier channel matrices $\mathbf{H_k}$:

$$\mathbf{H} = \begin{bmatrix} \mathbf{H_1} & 0 & 0 \\ 0 & \ddots & 0 \\ 0 & 0 & \mathbf{H_N} \end{bmatrix}. \tag{5.11}$$

Next, eigenvalue decomposition is performed on $\mathbf{H}.\mathbf{H}^H$, leading to a column vector of eigenvalues $\boldsymbol{\lambda}_{\mathbf{2D}} = [\lambda_1 \lambda_2 ... \lambda_{rN}]^T$ with $\lambda_1 > \lambda_2 > ... > \lambda_{rN}$. Subsequently, power is allocated to all rN virtual channels whereby the power of the virtual channel i is calculated as [51],[52]

$$p_i = \max\Big(0, \epsilon - \frac{\sigma^2}{\lambda_i}\Big). \tag{5.12}$$

The starting value of ϵ is equal to P_{TX}. Next, ϵ is iteratively decreased until the power constraint is met, indicating that the power

$$P_{TX} = \sum_{i=1}^{rN} p_i \tag{5.13}$$

is optimally distributed over the rN virtual channels. The capacity per virtual channel i, in bps/Hz, is calculated as

$$C_i = \log_2\Big[1 + \frac{p_i.\lambda_i}{\sigma^2}\Big]. \tag{5.14}$$

The OFDM capacity $\bar{C}_{\text{OFDM}}$, in bps/Hz, for uniform and one-dimensional MIMO, is calculated as the average over all N subcarrier capacities [24], [53], [54], corrected with the overhead O_v, caused by the cyclic prefix, yielding

$$\bar{C}_{\text{OFDM}} = \Bigg(\frac{1}{N}\sum_{k=1}^{N} C_k\Bigg)\Big(1 - O_v\Big). \tag{5.15}$$

Note that the one-dimensional spatial waterfilling MIMO-OFDM capacity is calculated in the same way by replacing C_k, derived from (5.6) or (5.7), by $C_{k,\text{1D}}$, derived from (5.10). Moreover, the overhead is also taken into account for the calculations of the SISO-, SIMO- and MISO-OFDM capacities. For two-dimensional waterfilling, the total OFDM capacity $\bar{C}_{\text{OFDM}}$, in bps/Hz, is calculated as the sum over all rN virtual channel capacities C_i, divided by the number of subcarriers N, and corrected with the overhead O_v:

$$\bar{C}_{\text{OFDM,2D}} = \Bigg(\frac{1}{N}\sum_{i=1}^{rN} C_i\Bigg)\Big(1 - O_v\Big) \tag{5.16}$$

However, to compare the subcarrier capacity of 2×2 MIMO_{2D} to uniform 2×2 MIMO and 2×2 MIMO_{1D}, the $2N$ virtual subchannel capacities are recalculated as N subcarrier capacities. Therefore, an eigenvalue decomposition is performed on $\mathbf{H}.\mathbf{H}^H$, producing a diagonal matrix $\mathbf{D}$ of eigenvalues and a full matrix $\mathbf{V}$ whose columns are the corresponding eigenvectors so that $(\mathbf{H}.\mathbf{H}^H).\mathbf{V} = \mathbf{V}.\mathbf{D}$. Note that the column vector $\boldsymbol{\lambda}_{\mathbf{2D}}$, as previously defined, contains the diagonal elements of $\mathbf{D}$ in decreasing order. The matrix $\mathbf{V}$, with dimensions *2N* × *2N*, contains only two non-zero elements per eigenvector (or per column) located on row-index r and row-index *r+1*, for odd row-indexes r. Moreover, for the first N eigenvectors of $\mathbf{V}$, the row-index r is unique with $r \in [1 \dots N-1]$. Yet, for the last N eigenvectors of $\mathbf{V}$, the same unique row-indexes are found, meaning that for only two (out of *2N*) eigenvectors, the non-zeros elements are located at the same row-indexes r and *r+1*.

When, for example, the non-zero elements of eigenvectors v_y and $v_{y'}$, with $v_y \in [1 \dots N]$ and $v_{y'} \in [N+1 \dots 2N]$, are located on the same row-indexes $[r_x, r_x+1]$, the eigenvalues $\mathbf{D}_{v_y,v_y}$ and $\mathbf{D}_{v_{y'},v_{y'}}$ are used to recalculate the capacity on subcarrier k with:

$$k = \frac{r_x + 1}{2}. \tag{5.17}$$

By finding $\mathbf{D}_{v_y,v_y}$ and $\mathbf{D}_{v_{y'},v_{y'}}$ in the sorted column vector $\boldsymbol{\lambda}_{\mathbf{2D}}$, the indexes i and j of the two virtual subchannels corresponding to subcarrier k are found, where index i corresponds to spatial subchannel $r = 1$ and index j corresponds to spatial subchannel $r = 2$. The MIMO_{2D} subcarrier capacity is then calculated using (5.14), yielding:

$$C_{k,\text{2D}} = C_i + C_j. \tag{5.18}$$

This algoritm calculates N subcarrier capacities out of *2N* virtual subchannel capacities for two-dimensional space-frequency waterfilling, allowing to use (5.15) to calculate the MIMO_{2D}-OFDM capacity by replacing C_k by $C_{k,\text{2D}}$, yielding the same MIMO_{2D}-OFDM capacity as (5.16).

5.3.4 Spatial correlation

For each of the 256 frequency-flat subcarriers, the complex correlation ρ between channel coefficients of two physical channels from the MIMO system is calculated. Because of the channel variations over time, in the 197 seconds long dynamic measurement scenario, the complex correlation coefficient ρ is calculated, per subcarrier, within a window corresponding to 1 second of measurements. Taken into account that both firefighters walk at 0.5 m/s, the path loss is expected to be constant within this window and hence the complex correlation coefficient ρ only comprises the shadowing and small-scale fading effects. Moreover, calculations show that the path loss standard deviation is only 1.89 dB within this1s- window, which is very small compared to the full measurement range, equal to 43.99 dB received SNR.

When calculating the correlation between, for example, the Front to Front (F2F) and Front to Back link (F2B) link, a matrix of 256x197 complex correlation coefficients is obtained. Further analysis is performed by first finding the time-average values of $|\rho|$ for each OFDM subcarrier and second by finding the average value over all subcarriers, as in [24]. Table 5.3 shows that the spatial correlation coefficients are below 0.7 which indicates that the channel coefficients on different subcarriers are sufficiently decorrelated. This implies that the MIMO-OFDM channel capacity is expected to increase when applying transmit and/or receive diversity on a subcarrier basis, for the dynamic measurement scenario.

Table 5.3: Amplitude of the correlation coefficient for the dynamic measurement scenario

	F2F	F2B	B2F	B2B
F2F	1	0.27	0.33	0.27
F2B	0.27	1	0.32	0.0.32
B2F	0.33	0.32	1	0.30
B2B	0.27	0.32	0.30	1

Table 5.4 presents the spatial correlation coefficients for the static measurement scenario (Fig 5.3). The correlation among two physical channels is higher than for the dynamic measurement scenario, which indicates that less MIMO-OFDM capacity gain is expected.

Table 5.4: Amplitude of the correlation coefficient for the static measurement scenario

	F2F	F2B	B2F	B2B
F2F	1	0.79	0.86	0.39
F2B	0.79	1	0.83	0.38
B2F	0.86	0.83	1	0.40
B2B	0.39	0.38	0.40	1

5.4 Measurement results

5.4.1 SISO- and MIMO-OFDM capacity

The resulting OFDM capacities, achieved per measurement cycle, are time varying. This behaviour is visualized by means of a Cumulative Distribution Function (CDF), for both the static and dynamic scenario, as seen in Figs 5.6 and 5.7, respectively. Consider the 10% outage capacity $\bar{C}_{\mathrm{OFDM,out,10}}$ being the OFDM capacity guaranteed during 90% of the time [49]. The characteristics also provide an indication of the capacity gain obtained by the different MIMO techniques, visible by a shift to the right of the curves. Capacities of each SISO link vary independently of each other due to the constantly varying mutual orientation and relative position of each firefighter as well as by people moving in the environment, resulting in a time-varying capacity gain. However, the capacity gain of the MIMO systems is only calculated for the 10% outage probability level [21]. We define $\bar{G}_{\text{OFDM,out,10}}$ as the 10% outage capacity gain, calculated by comparing the 10% outage MIMO capacity to the *median* of the corresponding SISO links. To make the chapter more concise, in the sequel we simply call $\bar{C}_{\text{OFDM,out,10}}$ outage capacity and $\bar{G}_{\text{OFDM,out,10}}$ outage capacity gain.

We now define the different MIMO schemes as:

- SIMO-F2F/B: TX front to RX front and back antenna
- SIMO-B2F/B: TX back to RX front and back antenna
- MISO-F/B2F: TX front and back to RX front antenna
- MISO-F/B2B: TX front and back to RX back antenna
- MIMO: TX front and back to RX front and back antenna

For the static scenario, the CDFs of all four SISO links, together with the SIMO-, MISO-, and MIMO-OFDM channels, are shown in Fig. 5.6. Note that, in order to not overload Fig. 5.6, the different CDFs are marked with a number or letter, corresponding to the different SISO and MIMO schemes, described in Table 5.5. The 10% outage capacity and the 10% outage capacity gain given are given in Table 5.6. From Fig. 5.6, it is clearly visible that the SISO-F2F and SISO-F2B links outperform the SISO-B2F and SISO-B2B link because the TX front antenna is pointing towards the receiver whereas the TX back antenna is oriented away from the RX firefighter, leading to smaller SNR and, hence, smaller capacity, in the latter two scenarios. The steep curves of all CDFs indicate only small capacity variations caused by people walking in the corridor and by small body movements of the static TX or RX firefighters.

Table 5.5: All SISO and MIMO schemes with their corresponding graphical marker as a legend for the calculated CDFs

SISO-F2F	①	SIMO-F2F/B	⑤	MIMO	⑨
SISO-F2B	②	SIMO-B2F/B	⑥	MIMO-1D	A
SISO-B2F	③	MISO-F/B2F	⑦	MIMO-2D	B
SISO-B2B	④	MISO-F/B2B	⑧		

As seen in Table 5.6, in the static scenario, SIMO-F2F/B, combining the strongest two SISO links, obviously leads to higher outage capacity than SIMO-B2F/B, combining the weakest two SISO links. In both SIMO scenarios, the outage capacities are higher than the stronger of their two SISO links. For MISO-F/B2F and MISO-F/B2B, combining a strong and weak SISO link, the outage capacities are smaller than SIMO-F2F/B but larger than SIMO-B2F/B. In both MISO scenarios, the outage

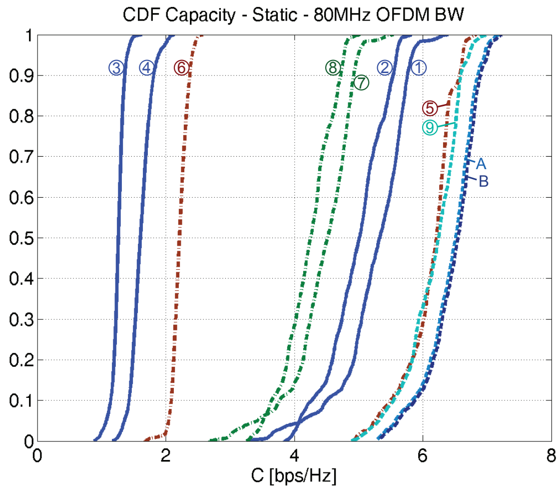

Figure 5.6: CDF of the calculated OFDM capacities, for all SISO and MIMO links, in the static scenario. Note that the CDF of MIMO$_{1D}$, indicated by A, is almost equal to the CDF of MIMO$_{2D}$, indicated by B

Table 5.6: Calculated 10% outage capacity (bps/Hz) and 10% outage capacity gain (bps/Hz), compared to the median of the corresponding SISO links, for both the static and dynamic scenario

	Static scenario		Dynamic scenario	
	$\bar{C}_{\text{OFDM,out,10}}$	$\bar{G}_{\text{OFDM,out,10}}$	$\bar{C}_{\text{OFDM,out,10}}$	$\bar{G}_{\text{OFDM,out,10}}$
SISO-F2F	4.51	-	0.80	-
SISO-F2B	4.27	-	1.04	-
SISO-B2F	1.14	-	1.45	-
SISO-B2B	1.43	-	1.21	-
SIMO-F2F/B	5.50	1.06	1.63	0.63
SIMO-B2F/B	2.09	0.75	2.32	0.84
MISO-F/B2F	3.77	0.86	1.79	0.28
MISO-F/B2B	3.64	0.67	1.77	0.22
MIMO	5.54	2.62	3.67	2.20
MIMO-1D	5.84	2.91	4.06	2.59
MIMO-2D	5.87	2.95	4.09	2.62

capacities are smaller than their stronger SISO link but larger than their weakest SISO link. This is caused by equally distributing the total TX power over the two TX antennas, meaning that the stronger SISO link has to sacrifice half its power to the weaker SISO link, leading to a reduced capacity. Since the capacity gain is calculated with respect to the median capacity of the two corresponding SISO links, the outage capacity gains are comparable for both the SIMO and MISO scenario.

For the uniform MIMO configuration, the outage capacity is higher than for all SISO, SIMO and MISO configurations. Moreover, when applying one- and two dimensional waterfilling, the outage capacity increases by an additional 0.30 bps/Hz and 0.33 bps/Hz, respectively, leading to the highest outage capacity, equal to 5.87 bps/Hz, as well as to the largest outage capacity gain, equal to 2.95 bps/Hz, when applying two-dimensional waterfilling.

When improving from the strongest SIMO (F2F/B) and MISO (F/B2F) configuration to the MIMO setup, the outage capacity gain is increased with 147% and 204% respectively, indicating that the outage capacity gain drastically increases when applying MIMO. Moreover, when channel state information is available at the transmitter, one- and two-dimensional waterfilling increase outage capacity gain by an additional 11.21% and 12.55%.

For the dynamic scenario, the CDFs of the capacity of all four SISO links together with SIMO-, MISO-, and MIMO-OFDM, are shown in Fig. 5.7. The outage capacity and the outage capacity gain are presented in Table 5.6. Note that the four SISO links, indicated by the solid lines, are comparable. Therefore, they are not marked separately. In the dynamic scenario, the less steep CDFs indicate that the OFDM capacity exhibits larger variations, compared to the static scenario, due to the constantly changing distance, mutual orientations and relative positions of both firefighters.

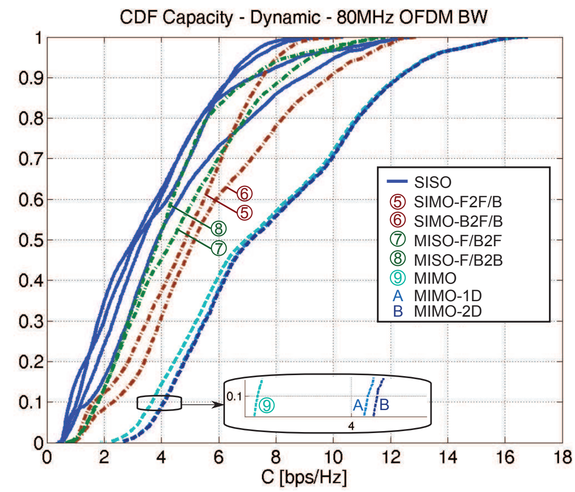

Figure 5.7: CDF of the calculated OFDM capacities, for all SISO and MIMO links, in the dynamic scenario

Since the OFDM capacity between the single SISO links differs less than in the static scenario, as seen in Table 5.6, both SIMO and MISO lead to higher outage capacity than each single SISO link. The capacity gain for MISO is smaller than for SIMO because the power per TX antenna is halved and all SISO links have approximately the same outage capacity. Therefore, the outage capacity gain is larger when combining two links at full TX power (SIMO) than when combining two links at half the TX power (MISO). As in the static scenario, MIMO with two-dimensional waterfilling leads to the highest outage capacity, equal to 4.09 bps/Hz, as well as to the largest outage capacity gain, equal to 2.62 bps/Hz. The outage capacity gain is increased by 162% when comparing the SIMO-B2F/B and MIMO channels and even by 686% when going from MISO-F/B2F to MIMO. Again, one- and two-dimensional waterfilling increase outage capacity gain by an additional 17.76% and 19.25% respectively, compared to the MIMO outage capacity without channel feedback.

For the dynamic measurement scenario, the multiplexing gain is expected to be higher. At first sight, this contradicts the results of Table 5.6. However, for the dynamic measurement scenario, the relative orientation of both rescue workers constantly changes. As a result, all four SISO channels exhibit approximately the same outage capacity. This implies that the 2.20 bps/Hz of outage capacity gain, compared to the *median* of the four SISO links, is a good indication of the potential multiplexing gain. In contrast, for the static measurement scenario, the positions and relative orientation of both rescue workers remain constant. As a result, some links will suffer more from body shadowing than others. The two weak SISO links, being B2F and B2B, which are the most affected by body-shadowing at both ends of the body-to-body channel, drastically decrease the median value of the four SISO links. This increases the outage capacity gain to an overestimated high value, equal to 2.62 bps/Hz. Therefore, we introduce the minimal multiplexing gain, calculated by comparing the outage MIMO capacity to the *strongest* of the corresponding SISO links. This minimal multiplexing gain is equal to 1.03 bps/Hz and 2.22 bps/Hz for the static and dynamic measurement scenarios, respectively. These results correspond to the expectations based on the spatial correlation coefficients presented in Table 5.3 and 5.4.

5.4.2 MIMO-OFDM waterfilling capacity gain

As mathematically described in (5.15), the MIMO-OFDM capacity per measurement cycle is calculated as the average capacity over all N subcarriers. This implies that the waterfilling capacity gain per measurement cycle, defined as $\bar{G}$, is calculated as the average of the subcarrier capacity gains G_k:

$$\bar{G} = \frac{1}{N}\sum_{k=1}^{N} G_k. \tag{5.19}$$

Since the subcarrier capacity gain G_k is limited, as described in the *frequency domain* subsection below, the capacity gain per measurement cycle $\bar{G}$ is also limited when applying one- or two-dimensional waterfilling, compared to uniform MIMO, as discussed in the *time domain* subsection. Define $C_{k_{r=1}}$ and $C_{k_{r=2}}$ as the spatial

SISO subcarrier capacities for uniform MIMO, $C_{k,1\mathrm{D}_{r=1}}$ and $C_{k,1\mathrm{D}_{r=2}}$ as the spatial SISO subcarrier capacities for $\mathrm{MIMO}_{1\mathrm{D}}$. Finally, let $C_{k,2\mathrm{D}_{r=1}}$ and $C_{k,2\mathrm{D}_{r=2}}$ be the spatial SISO subcarrier capacities for $\mathrm{MIMO}_{2\mathrm{D}}$.

Frequency domain

Because of the frequency selectivity of the wireless channel, the MIMO, $\mathrm{MIMO}_{1\mathrm{D}}$ and $\mathrm{MIMO}_{2\mathrm{D}}$ subcarrier capacities vary considerably over all N subcarriers, as seen on Fig. 5.8. Fig. 5.8.a shows the 2×2 uniform MIMO subcarrier capacity C_k, indicated by the thick blue line and calculated as the sum of the corresponding equivalent spatial SISO subchannels capacities, $C_{k_{r=1}}$ and $C_{k_{r=2}}$, as in (5.7). Fig. 5.8.b presents the 2×2 $\mathrm{MIMO}_{1\mathrm{D}}$ subcarrier capacity $C_{k,1\mathrm{D}}$, indicated by the thick blue line and calculated as the sum of $C_{k,1\mathrm{D}_{r=1}}$ and $C_{k,1\mathrm{D}_{r=2}}$ (red curves), as in (5.10). Fig. 5.8.c shows the 2×2 two-dimensional waterfilling $\mathrm{MIMO}_{2\mathrm{D}}$ subcarrier capacity $C_{k,2\mathrm{D}}$, indicated by the thick blue line and calculated as the sum of $C_{k,2\mathrm{D}_{r=1}}$ and $C_{k,2\mathrm{D}_{r=2}}$ (green curves), as in (5.18). The black curves in Figs. 5.8.b and 5.8.c correspond to the spatial SISO subchannels in case of uniform MIMO, extracted from Figure 5.8.a. They are included to compare spatial subchannel capacities in case of uniform MIMO with $\mathrm{MIMO}_{1\mathrm{D}}$ and $\mathrm{MIMO}_{2\mathrm{D}}$, respectively. In all three subfigures, the instantaneous subcarrier capacities are plotted for the first measurement cycle in the static scenario. Note that the rather flat MIMO-OFDM capacity curve for the strongest SISO subchannel $r = 1$, corresponding to the largest eigenvalue, is caused by the logarithmic relationship between the SNR and capacity. Since the effect of relatively small SNR variations on the capacity is small, only small subcarier capacity variations are noticeable for spatial SISO subchannel $r = 1$. The opposite holds when the relative SNR variation is large, leading to the significantly varying subcarrier capacity curve for the weaker SISO subchannel $r = 2$, corresponding to the smallest eigenvalue.

For one-dimensional waterfilling, define the condition number for subcarrier k as:

$$\kappa(k) = \frac{\lambda_{max}}{\lambda_{min}}. \tag{5.20}$$

Table 5.7: One-dimensional MIMO subcarrier capacity gains (over uniform MIMO), $G_{k,1D}$, for different subcarriers, yielding different condition numbers $\kappa(k)$

		$r=1$		$r=2$		
subcarrier	$\kappa(k)$	C_k	$C_{k,1\mathrm{D}}$	C_k	$C_{k,1\mathrm{D}}$	$G_{k,1\mathrm{D}}$
129	113	5.25	6.23	0.41	0	0.57
143	2420	5.70	6.69	0.03	0	0.96
182	12	6.10	6.21	2.68	2.57	0

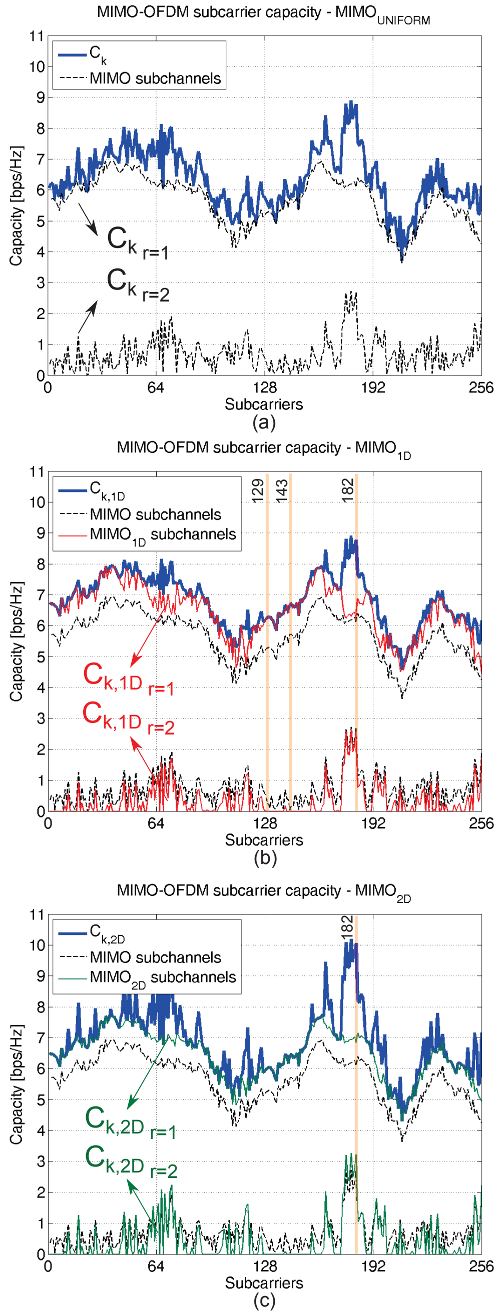

Figure 5.8: (a) 2×2 uniform MIMO subcarrier capacity C_k, (b) MIMO$_{1D}$ subcarrier capacity $C_{k,1D}$ and (c) MIMO$_{2D}$ subcarrier capacity $C_{k,2D}$. Subcarrier capacities are indicated by thick blue lines. The black curves in (b) and (c) correspond to the spatial SISO subchannels capacities in case of uniform MIMO, extracted from Fig. (a)

When $\kappa(k) >> 1$, the eigenvalue of the strongest spatial SISO subchannel is much larger than the eigenvalue of the smallest spatial SISO subchannel. This indicates that the subcarrier power P_k is completely allocated to the stronger of the two equivalent spatial SISO subchannels, doubling the SNR of this stronger SISO subchannel and, hence, leading to a theoretical maximum MIMO subcarrier capacity gain, on $r = 1$, equal to 1 bps/Hz. Yet, the total MIMO subcarrier capacity gain when applying one-dimensional waterfilling, $G_{k,1\mathrm{D}}$, depends on the capacity loss on spatial subchannel $r = 2$, to which less power is allocated. The one-dimensional waterfilling gain, over uniform MIMO, is calculated as

$$G_{k,1\mathrm{D}} = \left(C_{k,1\mathrm{D}_{r=1}} - C_{k_{r=1}}\right) - \left(C_{k,1\mathrm{D}_{r=2}} - C_{k_{r=2}}\right). \tag{5.21}$$

This is further explained in Table 5.7, explaining the varying $\mathrm{MIMO}_{1\mathrm{D}}$ subcarrier capacity gains for different subcarriers by the difference in condition number $\kappa(k)$. Subcarriers 129 and 143 exhibit a very large condition number. Therefore, the subcarrier capacity gains on $r = 1$ equal 0.98 and 0.99 bps/Hz, respectively, but the subcarrier capacity losses on $r = 2$ are equal to 0.41 and 0.03 bps/Hz, respectively. Hence, the total MIMO subcarrier capacity gains when applying one-dimensional waterfilling equal 0.57 bps/Hz for subcarrier 129, and 0.96 bps/Hz for subcarrier 143, strongly approaching the theoretical maximum. In contrast, when $\kappa(k) \rightarrow 1$, the eigenvalues of both spatial SISO subchannels become more equal, indicating more uniform power allocation over both SISO subchannels, and hence, producing no MIMO subcarrier capacity gain $G_{k,1\mathrm{D}}$, as for subcarrier 182.

In case of two-dimensional waterfilling, the subcarrier power is not limited to P_k. This implies that, compared to $\mathrm{MIMO}_{1\mathrm{D}}$, both the subcarrier capacities of $r = 1$ and $r = 2$ can increase, meaning that the MIMO subcarrier capacity gain could exceed 1 bps/Hz. This phenomenon is visible on subcarrier 182, as indicated on Fig. 5.8.c. When comparing MIMO and $\mathrm{MIMO}_{2\mathrm{D}}$, the capacity of the strongest spatial subchannel $r = 1$ rose from 6.10 bps/Hz to 6.85 bps/Hz while the capacity of the weakest spatial subchannel $r = 2$ is also increased from 2.68 bps/Hz to 3.21 bps/Hz, leading to a total MIMO subcarrier capacity gain $G_{k,2\mathrm{D}}$ equal to 1.28 bps/Hz. This additional power allocation to the stronger subcarriers results in less power allocated to other, weaker subcarriers. This could result in subcarrier capacity loss (instead of gain) when comparing MIMO and $\mathrm{MIMO}_{2\mathrm{D}}$. However, the two-dimensional space-frequency waterfilling algorithm optimizes the power allocation to ensure that the total $\mathrm{MIMO}_{2\mathrm{D}}$-OFDM capacity, calculated as the mean over all N subcarrier capacities, is larger than both the uniform MIMO-OFDM and $\mathrm{MIMO}_{1\mathrm{D}}$-OFDM capacities, as proven below.

Time domain

Since the calculated MIMO-OFDM capacity is time-varying, also the capacity gains (per measurement cycle) for $\mathrm{MIMO}_{1\mathrm{D}}$ or $\mathrm{MIMO}_{2\mathrm{D}}$ vary over time, as shown in

Fig. 5.9 for the dynamic scenario in interval AC. Fig. 5.9 indicates that, on the one hand, both the one- and two-dimensional waterfilling gains depend on the capacity already achieved by uniform MIMO, indicated by the solid blue line in Fig. 5.9. The lower the uniform MIMO-OFDM capacity, the higher the potential waterfilling gains, indicated by the two dashed lines on Fig. 5.9.

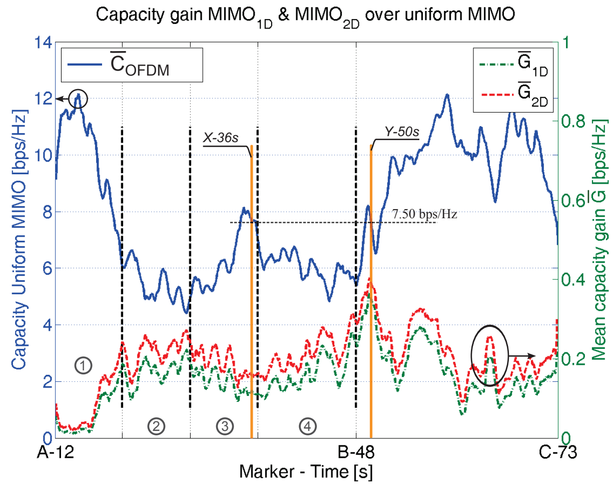

Figure 5.9: Time-domain behaviour of 2×2 *MIMO*$_{1D}$ *and* 2×2 *MIMO*$_{2D}$ *capacity gain, compared to the uniform* 2×2 *MIMO-OFDM capacity* $\bar{C}_{OFDM}$*, as calculated in (5.15), for interval AC in the dynamic scenario.*

On the other hand, for one-dimensional waterfilling, as described before, the subcarrier capacity gain $G_{k,1\mathrm{D}}$ depends on the condition number $\kappa(k)$, indicating that the mean waterfilling capacity gain over all N subcarriers, defined as $\bar{G}_{1\mathrm{D}}$, also depends on the mean condition number over all N subcarriers, defined as $\bar{\kappa}$. This is shown in Table 5.8 for two time instances with the same uniform MIMO-OFDM capacity. As the mean condition number over all N subcarriers, $\bar{\kappa}$, is nine times higher for time instance Y than for time instance X, the power, allocated to the strongest spatial subchannel $r = 1$, is higher for time instance Y. This increases the one-dimensional subcarrier capacity gains $G_{k,1\mathrm{D}}$, increasing the mean one-dimensional waterfilling gain $\bar{G}_{1\mathrm{D}}$, from 0.11 to 0.35, when comparing time instant X with time instant Y.

The two-dimensional waterfilling algorithm allocates equal power to the largest N (of rN) eigenvalues or to the strongest N virtual channels, corresponding to spatial SISO subchannel $r = 1$. The larger the ratio between the mean of the largest N eigenvalues and the mean of the smallest N eigenvalues, defined by ν, the more power the algorithm allocates to the strongest N virtual channels and, hence, the larger the two-dimensional waterfilling gain $\bar{G}_{2\mathrm{D}}$ over uniform MIMO.

Table 5.8 shows that the ratio between the mean of the largest N eigenvalues and the mean of the smallest N eigenvalues, ν, is 45 times higher for time instance Y than for time instance X. Therefore, the equal power allocated to the strongest N virtual channels is higher for time instance Y than for time instance X, leading to increased two-dimensional subcarrier capacity gains $G_{k,2\mathrm{D}}$. This also increases the mean two-dimensional waterfilling gains $\bar{G}_{2\mathrm{D}}$, from 0.16 to 0.39, when comparing time instant X with time instant Y.

Table 5.8: One-and two-dimensional mean waterfilling gains, $\bar{G}_{1D}$ and $\bar{G}_{2D}$, in bps/Hz, for different time instances, having the same uniform MIMO-OFDM capacity, $\bar{C}_{OFDM}$, in bps/Hz

Time	$\bar{C}_{\mathrm{OFDM}}$	$\bar{G}_{1\mathrm{D}}$	$\bar{G}_{2\mathrm{D}}$	$\bar{\kappa}$	ν
X = 36s	7.50	0.11	0.16	3.87	14.77
Y = 50s	7.49	0.35	0.39	34.36	666.95

In Fig. 5.9, the high MIMO-OFDM capacity in interval BC, when both firefighters are walking in the corridor in the positive X-direction (Fig. 5.4), is caused by the LoS link, leading to a strong B2F SISO link. Moreover, as indicated in Fig. 5.5, in interval BC, also the B2B link is strong owing to the limited relative distance between both firefighters. Also for subinterval ① in interval AC (Fig. 5.9), the high MIMO-OFDM capacity is caused by a LoS link between the TX back and RX back antenna, as visible in Fig. 5.5. Oppositely, the smaller MIMO-OFDM capacities in subinterval ② to ④, corresponding to a NLoS scenario, are caused by the absence of a strong LoS link, since one firefighter is located in office 1 while the other firefighter is located in the corridor.

5.5 Conclusion

In this chapter, real-life firefighter rescue operations were replicated by means of a static and dynamic measurement campaign, from which the SISO-, SIMO-, MISO- and MIMO-OFDM capacities are calculated for realistic indoor broadband body-to-body communication channels. By considering the RMS delay spread and 50% correlation bandwidth, derived from the channel impulse responses collected with the Elektrobit channel sounder, it is found that the wideband IEEE 802.11ac and IEEE 802.11n standards are good candidates for indoor body-to-body communication, a purpose for which they were originally not designed. Indoor body-to-body communication is different from regular Wi-Fi links because the channel is highly variable, especially in dynamic scenarios. Moreover, both ends of the body-to-body link experience body-shadowing effects.

When no channel state information is available at the transmitter, data rates equal to 443 Mbps and 294 Mbps are achieved, during 90% of the time, in the static and dynamic scenario, respectively, with an OFDM bandwidth equal to 80 MHz, as possible in 5 GHz Wi-Fi. These data rates, obtained at a transmit power equal to 1.5 mW, are definitely sufficient, even with a code rate of 1/2, to ensure efficient communication of crucial information between firefighters. When channel state information is available at both the transmitter and receiver, allowing waterfilling MIMO-OFDM by allocating more power to stronger channels, only a relatively small 24 Mbps and 26.4 Mbps extra data rate are achieved, during 90% of the time in the static scenario, for one- and two-dimensional waterfilling respectively. Also in the dynamic scenario, only an extra 31.2 Mbps and 33.6 Mbps data rate are obtained when applying one-or two dimensional waterfilling respectively. This implies that implementing channel feedback, which increases system complexity, is not essential to guarantee efficient communication of live sensor data, pictures or videos between two firefighters of the Rapid Intervention Team. Moreover, by implementing 2×2 MIMO, even without waterfilling and its channel feedback requirements, the 10% outage MIMO capacity gain drastically increases, with a minimum of 147%, over SIMO and MISO, in both the static and dynamic scenario.

Considering the smaller bandwidth in the 2.45 GHz ISM band, equal to 20 MHz, data rates of 111 Mbps and 73 Mbps are achieved in the static and dynamic scenario, respectively, for simple 2× 2 MIMO without channel feedback. This implies that, even for lower bandwidths, the obtained data rates are definitely sufficient for transferring live sensor data, pictures and videos, between static or simultaneously moving firefighters, with only two high-performance on-body antennas. Moreover, because of the limited battery capacity of the on-body devices, an energy-efficient 2 × 2 MIMO system may be more suitable for body-to-body communication than higher-order MIMO systems, which provide higher data rates at the cost of larger power consumption.

Two general conclusions can be drawn for real-life, indoor rescue operations where a Rapid Intervention Team is performing the primary search, looking for any victims:

- High data rates are achieved with only limited transmit power and a limited number of on-body antennas when a wideband channel is available.
- It is not beneficial to implement (complex) waterfilling algorithms in wideband indoor body-to-body channels.

Acknowledgment

The authors would like to acknowledge IAP BESTCOM and UCL for providing the Elektrobit channel sounder and the measurement locations.

References

[1] N. Brushlinsky, J. Hall, S. Sokolov, and P. Wagner, *World Fire Statistics*. International Association of Fire and Resue Services, CTIF, 2014, vol. 19.

[2] "Firefighter fatalities in the United States in 2012", U.S. Department of Homeland Security, Federal Emergency Management Agency, U.S. Fire Administration, National Fire Data Center and The National Fallen Firefighters Foundation, Report, Aug. 2013.

[3] D. McGrail, "Firefighting operations in high-rise and standpipe-equipped buildings", in. PennWell Books, 2007, ch. 16.

[4] "Electromagnetic compatibility and Radio spectrum Matters (ERM); Wideband transmission systems; Data transmission equipment operating in the 2,4 GHz ISM band and using wide band modulation techniques", Tech. Rep.

[5] "FCC increases 5GHz spectrum for Wi-Fi, other unlicensed uses", Federal Communications Commission, Tech. Rep., 2014.

[6] "802.11ac", IEEE Standard for Information technology - Telecommunications and information exchange between systems - Local and metropolitan area networks - Specific requirements - Part 11: Wireless LAN Medium Access Control (MAC) and Physical Layer (PHY) Specifications - Amendment 4: Enhancements for Very High Throughput for Operation in Bands below 6 GHz, Tech. Rep., 2013.

[7] "802.11n", IEEE Standard for Information technology - Local, metropolitan area networks - Specific requirements - Part 11: Wireless LAN Medium Access Control (MAC), and Physical Layer (PHY) Specifications - Amendment 5: Enhancements for Higher Througput, Tech. Rep., 2009.

[8] "WiMAX Advanced: Deployment scenarios based on input from WiMAX operators and vendors", WiMAX Forum Proprietary, Tech. Rep., 2014.

[9] S. Cotton, W. Scanlon, and J. Guy, "The Kappa-Mu distribution applied to the analysis of fading in body to body communication channels for fire and rescue personnel", *Antennas Wireless Propagation Letters (AWPL)*, vol. 7, pp. 66–69, 2008.

[10] "Smart@fire project", European Commission (FP7), Innovation Agency (IWT), the Belgian Federal Home Aff airs Ministry (IBZ) and the French SDIS Fire Department Bouches-du-Rhöner, Project, 2012-2015.

[11] R. Cavallari, F. Martelli, R. Rosini, C. Buratti, and R. Verdone, "A survey on wireless body area networks: Technologies and design challenges", *IEEE Communications Surveys & Tutorials*, vol. 16, no. 3, pp. 1635–1657, 2014.

[12] P. Hall and Y. Hao, *Antennas and Propagation for Body-Centric Wireless Communications. Second Edition*. Artech House, 2012.

[13] E. Reusens, W. Joseph, B. Latre, B. Braem, G. Vermeeren, E. Tanghe, L. Martens, I. Moerman, and C. Blondia, "Characterization of on-body communication channel and energy efficient topology design for wireless body area networks", *IEEE Transactions on Information Technology in Biomedicine*, vol. 13, no. 6, pp. 933–945, Nov. 2009.

[14] P. Vanveerdeghem, P. Van Torre, C. Stevens, J. Knockaert, and H. Rogier, "Synchronous wearable wireless body sensor network composed of autonomous textile nodes", *Sensors*, vol. 14, no. 10, pp. 18 583–18 610, Oct. 2014.

[15] K. Ghanem, I. Khan, P. Hall, and L. Hanzo, "MIMO stochastic model and capacity evaluation of on-body channels", *IEEE Transactions on Antennas and Propagation*, vol. 60, no. 6, pp. 2980–2986, Jun. 2012.

[16] I. Khan, P. Hall, A. Serra, A. Guraliuc, and P. Nepa, "Diversity performance analysis for on-body communication channels at 2.45 GHz", *IEEE Transactions on Antennas and Propagation*, vol. 57, no. 4, pp. 956–963, Apr. 2009.

[17] I. Khan and P. Hall, "Experimental evaluation of MIMO capacity and correlation for narrowband body-centric wireless channels", *IEEE Transactions on Antennas and Propagation*, vol. 58, no. 1, pp. 195–202, Jan. 2010.

[18] C. Ahn, B. Ahn, S. Kim, and J. Choi, "Experimental outage capacity analysis for off-body wireless body area network channel with transmit diversity", *IEEE Transactions on Consumer Electronics*, vol. 58, no. 2, pp. 274–277, May 2012.

[19] L. Vallozzi, P. Van Torre, C. Hertleer, H. Rogier, M. Moeneclaey, and J. Verhaevert, "Wireless communication for firefighters using dual-polarized textile antennas integrated in their garment", *IEEE Transactions on Antennas and Propagation*, vol. 58, no. 4, pp. 1357–1368, Apr. 2010.

[20] P. Van Torre, L. Vallozzi, H. Rogier, and J. Verhaevert, "Diversity textile antenna systems for firefighters", in *Proceedings of the 4th European Conference on Antennas and Propagation (EuCAP)*, Barcelona, Spain: IEEE, Apr. 2010, pp. 1–5.

[21] P. Van Torre, L. Vallozzi, C. Hertleer, H. Rogier, M. Moeneclaey, and J. Verhaevert, "Indoor off-body wireless MIMO communication with dual polarized textile antennas", *IEEE Transactions on Antennas and Propagation*, vol. 59, no. 2, pp. 631–642, Feb. 2011.

[22] P. Van Torre, L. Vallozzi, H. Rogier, M. Moeneclaey, and J. Verhaevert, "Reliable mimo communication between firefighters equipped with wearable antennas and a base station using space-time codes", in *Proceedings of the 5th European Conference on Antennas and Propagation (EUCAP)*, Rome, Italy: IEEE, Apr. 2011, pp. 2690–2694.

[23] D. Neirynck, C. Williams, A. Nix, and M. Beach, "Exploiting multiple-input multiple-output in the personal sphere", *IET Microwaves, Antennas & Propagation*, vol. 1, no. 6, pp. 1170–1176, 2007.

[24] H. Suzuki, T. Tran, and I. Collings, "Characteristics of MIMO-OFDM channels in indoor environments", *EURASIP Journal on Wireless Communications and Networking*, vol. 2007, no. 1, pp. 1–9, Dec. 2006.

[25] R. Piechocki, P. Fletcher, A. Nix, N. Canagarajah, and J. McGeehan, "A measurement based feasibility study of space-frequency MIMO detection and decoding techniques for next generation wireless LANs", in *Proceedings of International Conference on Consumer Electronics*, Los Angeles, CA, USA, Jun. 2002, pp. 368–369.

[26] K. Yu, M. Bengtsson, B. Ottersten, D. McNamara, P. Karlsson, and M. Beach, "Modeling of wide band MIMO radio channels based on NLoS indoor measurements", *IEEE Transactions on Vehicular Communications*, vol. 53, no. 3, pp. 655–665, May 2004.

[27] R. Rao, S. Lang, and B. Daneshrad, "Indoor field measurements with a configurable multi-antenna testbed", in *Proceedings of IEEE Global Telecommunications Conference (GLOBECOM)*, vol. 6, Dallas, US: IEEE, Dec. 2004.

[28] J. Gupta and K. Ziri-Castro, "Body-shadowing effects in indoor MIMO-OFDM channel capacity", in *Proceedings of the Australasian Telecommunications Networks and Applications Conference (ATNAC)*, Canberra, Australia: IEEE, Nov. 2009, pp. 1–9.

[29] A. Gupta, A. Forenza, and R. Heath, "Rapid MIMO-OFDM software defined radio system prototyping", in *Proceedings of IEEE Workshop on Signal Processing Systems Design and Implementation*, Austin, Texas: IEEE, Oct. 2004, pp. 182–187.

[30] P. Kafle, A. Sesay, and J. McRory, "Capacity of MIMO-OFDM systems in spatially correlated indoor fading channels", in *Proceedings of the 60th Vehicular Technology Conference (VTC)*, vol. 1, Los Angeles, US: IEEE, Sep. 2004, pp. 129–133.

[31] M. Sudjai, L. Tran, and F. Safaei, "Performance analysis of STFC MB-OFDM UWB in WBAN channels", in *Proceedings of the 23rd IEEE Workshop on Personal Indoor and Mobile Radio Communications (PIMRC)*, Sydney, Australia: IEEE, Sep. 2012, pp. 1710–1715.

[32] Q. Abbasi, A. Sani, A. Alomainy, and Y. Hao, "On-body radio channel characterization and system-level modeling for multiband OFDM ultra-wideband body-centric wireless network", *IEEE Transactions on Microwave Theory Techniques*, vol. 58, no. 12, pp. 3485–3492, Dec. 2010.

[33] S. Cotton and W. Scanlon, "Channel characterization for single- and multiple-antenna wearable systems used for indoor body-to-body communications", *IEEE Transactions on Antennas and Propagation*, vol. 57, no. 4, pp. 980–990, Apr. 2009.

[34] R. Rosini, R. Verdone, and R. D'Errico, "Body-to-body indoor channel modeling at 2.45 GHz", *IEEE Transactions on Antennas and Propagation*, vol. 62, no. 11, pp. 5807–5819, Nov. 2014.

[35] Q. Wang, K. Masami, and J. Wang, "Channel modeling and BER performance for wearable and implant UWB body area links on chest", in *Proceedings of the International Conference on Ultra-Wideband (ICUWB)*, Vancouver, Canada: IEEE, Sep. 2009, pp. 316–320.

[36] K. Ghanem, "Effect of channel correlation and path loss on average channel capacity of body-to-body systems", *IEEE Transactions on Antennas and Propagation*, vol. 61, no. 12, pp. 6260–6265, Dec. 2013.

[37] P. Van Torre, L. Vallozzi, C. Hertleer, H. Rogier, M. Moeneclaey, and J. Verhaevert, "Dynamic link performance analysis of a rescue worker's off-body communication system using integrated textile antennas", *IET Science, Measurement Technology*, vol. 4, no. 2, pp. 41–52, Mar. 2010.

[38] S. Lemey and H. Rogier, "SIW textile antennas as a novel technology for UWB RFID tags", in *Proceedings of RFID Technology and Applications Conference (RFID-TA)*, Tampere, Finland: IEEE, Sep. 2014, pp. 256–260.

[39] G. Corbet, "Fire engineering's handbook for firefighter I and II", in. Pennwell, 2009, ch. 14, ISBN: 978-1-59-370135-2.

[40] S. van Roy, F. Quitin, L. Liu, C. Oestges, F. Horlin, J. Dricot, and P. De Doncker, "Dynamic channel modeling for multi-sensor body area networks", *IEEE Transactions on Antennas and Propagation*, vol. 61, no. 4, pp. 2200–2208, Apr. 2013.

[41] N. Czink, A. Ariza, K. Haneda, M. Jacob, J. Kåredal, M. Käske, J. Medbo, J. Poutanen, J. Salmi, G. Steinböck, and K. Witrisal, *Pervasive Mobile and Ambient Wireless Communications, Chapter2: Channel Measurements*. Springer, 2012, pp. 5–65.

[42] B. Ahmed, J. Masa Campos, and J. Lalueza Mayordomo, "Propagation path loss and materials insertion loss in indoor environment at WiMAX band of 3.3 to 3.6 GHz", *Wireless Personal Communications*, vol. 66, no. 2, pp. 251–260, 2012.

[43] J. Leibovitz. (April, 2015). Breaking down barriers to innovation in the 3.5 GHz band, [Online]. Available: `https://www.fcc.gov/blog/breaking-down-barriers-innovation-35-ghz-band`.

[44] E. Zhou, X. Zhang, H. Zhao, and W. Wang, "Synchronization algorithms for MIMO OFDM systems", in *IEEE Wireless Communications and Networking Conference*, vol. 1, Mar. 2005, pp. 18–22.

[45] A. Goldsmith, *Wireless Communications*. Cambridge University Press, 2005.

[46] B. Maharaj, J. Wallace, L. Linde, and M. Jensen, "Frequency scaling of spatial correlation from co-located 2.4 and 5.2 GHz wideband indoor MIMO channel measurements", *Electronics Letters*, vol. 41, no. 6, pp. 336–337, Mar. 2005.

[47] G. Janssen, P. Stigter, and R. Prasad, "Wideband indoor channel measurements and BER analysis of frequency selective multipath channels at 2.4, 4.75, and 11.5 GHz", *IEEE Transactions on Communications*, vol. 44, no. 10, pp. 1272–1288, Oct. 1996.

[48] T. Deckert, "Orthogonal Frequency Division Multiplexing Based Medium Access Under Rate Constraints", in. Vogt, 2007, ch. 4, ISBN: 978-3-93-886008-3.

[49] A. Paulraj, R. Nabar, and D. Gore, *Introduction to Space-Time Wireless Communications*. Cambridge University Press, 2003, ISBN: 978-0-52-182615-0.

[50] T. Cover and J. Thomas, *Elements of Information Theory (Wiley Series in Telecommunications and Signal Processing)*. Wiley-Interscience, 1991.

[51] Y. Jiang, M. Shen, and Y. Zhou, "Two-dimensional water-filling power allocation algorithm for MIMO-OFDM systems", English, *Science China Information Sciences*, vol. 53, no. 6, pp. 1242–1250, 2010.

[52] P. Almers, F. Tufvesson, O. Edfors, and A. Molisch, "Measured capacity gain using water filling in frequency selective MIMO channels", in *The 13th IEEE International Symposium on Personal, Indoor and Mobile Radio Communications*, vol. 3, Lisboa, Portugal: IEEE, Sep. 2002, pp. 1347 –1351.

[53] Y.-Q. Jiang, "Accurate capacity analysis for MIMO-OFDM systems considering correlation between subcarriers", in *Proceedings of the IEEE 12th International Conference on Communication Technology*, IEEE, Nov. 2010.

[54] Y. Liang, R. Zhang, and J. Cioffi, "Transmit optimization for MIMO-OFDM with delay-constrained and no-delay-constrained traffic", *IEEE Transactions on Signal Processing*, vol. 54, no. 8, pp. 3190–3199, Aug. 2006.

6

Adaptive Subcarrier Modulation for Indoor Public Safety Networks

Thijs Castel, Sam Lemey, Sam Agneessens, Patrick Van Torre, Hendrik Rogier and Claude Oestges

Presented at the 10th European Conference on Antennas and Propagation

★ ★ ★

In this chapter, we present the Bit Error Rate characteristics for an indoor, wideband body-to-body channel between two firefighters when using IEEE 802.11 ac, which is proven a very suitable standard for future, wideband public safety networks. Moreover, the BER and throughput characteristics, when applying both transmission blocking, fixed and adaptive, subcarrier modulation are presented. These characteristics show an increased throughput when applying adaptive subcarrier modulation. We have conducted a wideband, indoor channel sounder campaign at 3.6 GHz with 120 MHz useful bandwidth, simulating real-life rescue operations performed by two simultaneously moving members of the Rapid Intervention Team. Both firefighters were equipped with low-profile, lightweight and energy-efficient Ultra-Wideband Cavity-Backed slot antennas in Substrate Integrated Waveguide technology, unobtrusively deployed inside the front and back sections of their jackets, providing 2×2 *MIMO capability.*

6.1 Introduction

Future Public Safety Networks, which support communication between on-duty firefighters, are expected to evolve from narrowband towards wideband Wireless Body Area Networks (WBANs) [1], [2]. By applying Orthogonal Frequency Division Multiplexing (OFDM), these wideband, frequency-selective channels can be subdivided into multiple frequency-flat, orthogonal subcarriers, increasing the total throughput compared to state-of-the-art narrowband public safety networks. Moreover, the highest possible modulation order, which still guarantees a sufficiently low Bit Error Rate (BER), may be applied per frequency-flat subcarrier. This strategy increases the throughput on each subcarrier, and hence, maximizes the total throughput. This high throughput, combined with a low BER, allows multimedia broadcast and efficient communication of real-time on-body sensor data between on-duty firefighters. Moreover, the rescue workers' situational awareness increases whereas the response time of operation decreases, which is a major advantage in indoor public safety networks where minutes, or even seconds count.

Therefore, a wideband indoor body-to-body channel sounder campaign, replicating real-life rescue operations performed by the Rapid Intervention Team (RIT), has been carried out in an office environment. Both members of the RIT, typically operating in each others vicinity, were equipped with two low-profile, lightweight Ultra-Wideband (UWB) textile antennas [3], unobtrusively integrated in the front and back sections of their firefighter jackets, providing a 2×2 MIMO link.

Considering that the IEEE 802.11 ac standard [4] is proven very suitable for indoor body-to-body channels, we analyze the BER performance of the four modulations supported by this wideband standard, being 4-, 16-, 64- and 256 Quadrature Amplitude Modulation (QAM). Moreover, we prove that the 2×2 MIMO wideband, body-to-body channel can be subdivided into two independent, quasi-uncorrelated spatial subchannels which simultaneously transmit data, providing multiplexing, and, hence, throughput gain. The throughput of these two spatial subchannels is further optimized by fixed or adaptive subcarrier modulation with transmission blocking [5]. This optimization algorithm blocks transmission on subcarriers leading to a BER higher than the pre-set BER threshold while assigning the same, or an adaptively changing, modulation to the other, active subcarriers that guarantee a BER smaller than or equal to the pre-set BER threshold.

A simple adaptive modulation technique for individual subcarriers was already proposed in 1996 by Czylwik [6], showing that the required power can be dramatically reduced when applying adaptive, instead of fixed, subcarrier modulation. Through the years, more complex adaptive modulation schemes were proposed, focusing on trade-off between performance and throughput [7], maximizing spectral efficiency [8] or minimizing transmission energy [9]. However, only [10] proposes an adaptive scheme for the WBAN physical layer, concentrating on off-body communication. Increasing BER performance and decreasing power consumption are demonstrated. This chapter proposes, for the first time in literature, an analysis of fixed and adaptive subcarrier modulation with transmission blocking for indoor, wideband body-to-body channels. The scheme maximizes the potential throughput and, hence, data rate in future wideband public safety networks.

6.2 Measurement setup

A real-life rescue operation, performed by the Rapid Intervention Team looking for potential victims, was replicated by mobile measurements during which both firefighters were simultaneously moving around on the same floor of an office block, as shown in Fig. 6.1. Both the TX and RX firefighters were equipped with two low-profile, lightweight and flexible Ultra-Wideband cavity-backed slot antennas in Substrate Integrated Waveguide (SIW) technology [3]. These antennas provide stable radiation characteristics when placed on different on-body locations. Moreover, they are unobtrusively integrated inside the front and back sections of the firefighter jackets, as shown in Fig. 6.1, implementing 2×2 MIMO. When both firefighters enter a building, the RX firefighter, whose trajectory is marked by the short dashed line on Fig. 6.1, starts scanning the offices whereas the TX firefighter, whose trajectory is marked by the longer dashed line, is simultaneously scanning the hallway, while he remains close to the RX firefighter. The markers A, B and C, placed along both firefighter trajectories, indicate where the firefighters are located at the same time instant during the one-minute-long measurement, collecting 4650 measurement cycles for all four body-to-body links. Measurements were performed using the Elektrobit channel sounder at 3.6 GHz center frequency with 120 MHz useful bandwidth. The TX power was chosen equal to 20 dBm to obtain reliable wideband, body-to-body channel measurements.

6.3 MIMO-OFDM

6.3.1 Compatibility with the IEEE 802.11 ac standard

By means of the high-resolution power delay profiles, directly provided by the Elektrobit channel sounder, the *maximum* RMS delay spread during 90% of the time, defined as $\tau_{RMS,90}$ is found for the Front to Back (F2B) link. We obtain $\tau_{RMS,90}$ equal to 45.80 ns. When employing OFDM, the wideband, frequency-selective, body-to-body channel is subdivided into N lower data rate, orthogonal subcarriers. When focusing on the time domain, a Cyclic Prefix (CP) is added in between two consecutive OFDM symbols on one subcarrier to avoid Inter Symbol Interference (ISI). The minimal CP length should be larger than, or equal to, 3 times the maximal RMS delay spread [11]. The calculated OFDM parameter is compatible with the IEEE 802.11 ac standard, which sets the minimal cyclic prefix length equal to 400 ns seconds, being larger than 137.4 ns. For further calculations,

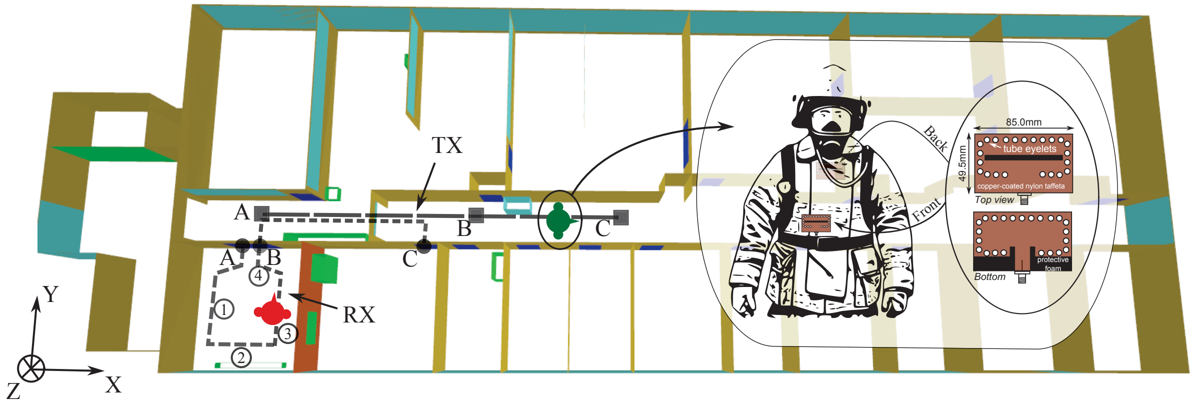

Figure 6.1: Simplified indoor office model with the wideband body-to-body measurement scenario together with the front and back locations of the two integrated UWB SIW textile antennas, for both the TX and RX firefighter

the wideband indoor body-to-body channel is subdivided into 256 frequency-flat subcarriers, corresponding to a total OFDM bandwidth equal to 80 MHz.

6.3.2 Eigenvalue Decomposition

When employing MIMO-OFDM, the MIMO channel can be subdivided into r equivalent SISO spatial subchannels, with $r = \min(N_{TX}, N_{RX})$. The received Signal to Noise Ratio (SNR) of these SISO spatial subchannels is calculated via the eigenvalue decomposition of $\mathbf{H_k}.\mathbf{H_k}^H$, with $\mathbf{H_k}$ the channel matrix of subcarrier k. This leads to a column vector of eigenvalues $\boldsymbol{\lambda}_\mathbf{k} = [\lambda_{1,k}\,\lambda_{2,k}\,...\,\lambda_{r,k}]^T$. The received SNR on subcarrier k for spatial subchannel i is then calculated as:

$$\mathrm{SNR}_{i,k} = \frac{P_k}{N_{TX}.\sigma^2} \cdot \lambda_{i,k}, \tag{6.1}$$

with P_k the transmit power allocated to subcarrier k, σ^2 the noise power and N_{TX} the number of transmit antennas. The eigenvalue decomposition, dependent on the spatial correlation between the links from any transmit to any receive antenna, gives an indication of the possible multiplexing gain, per subcarrier, when applying MIMO-OFDM. This implies that the spatial multiplexing gain per subcarrier, when applying 2×2 MIMO, is largest if the two eigenvalues are equal, corresponding to fully uncorrelated, equal-gain, spatial channels, and hence fully exploiting parallelism. When using the method described in [12], the spatial correlation between the F2F and B2B link is found equal to 0.17. This indicates that the channel coefficients are sufficiently decorrelated to ensure spatial multiplexing, and hence, throughput gain per subcarrier when subdividing the 2×2 MIMO-OFDM channel into two independent, quasi-uncorrelated spatial subchannels.

6.3.3 Bit Error Rate

Define M the number of constellation points for a M-square constellation and the Q-function such that, when employing Gray-mapping, the Bit Error Rate of subcarrier k for spatial subchannel i is calculated as:

$$\mathrm{BER}_{i,k} = \frac{N_b}{\log_2(M)} Q\left(\sqrt{\frac{d_{min}^2}{2} \cdot \mathrm{SNR}_{i,k}}\right), \tag{6.2}$$

with:

$$N_b = \frac{4\left(\sqrt{M} - 1\right)}{\sqrt{M}}, \tag{6.3}$$

$$d_{min}^2 = \frac{6}{M-1}. \tag{6.4}$$

Define L the number of measurement cycles, r the number of spatial subchannels and N the number of frequency-flat subcarriers such that the mean received SNR and mean BER are calculated as:

$$\overline{\mathrm{SNR}} = \frac{1}{L}\sum_{l=1}^{L}\left(\frac{1}{r}\sum_{i=1}^{r}\left(\frac{1}{N}\sum_{k=1}^{N}\mathrm{SNR}_{l,i,k}\right)\right), \tag{6.5}$$

$$\overline{\mathrm{BER}} = \frac{1}{L}\sum_{l=1}^{L}\left(\frac{1}{r}\sum_{i=1}^{r}\left(\frac{1}{N}\sum_{k=1}^{N}\mathrm{BER}_{l,i,k}\right)\right). \tag{6.6}$$

Fig. 6.2 presents the BER characteristics of the different modulations supported by the IEEE 802.11 ac standard when employing uniform power allocation. Due to body shadowing effects, 4QAM performs worse than the simulated 4QAM curve for Rayleigh fading and diversity order 1. Also note that for the same $\overline{\mathrm{SNR}}$, the higher order modulations lead to higher $\overline{\mathrm{BER}}$ due to the reduced noise margin.

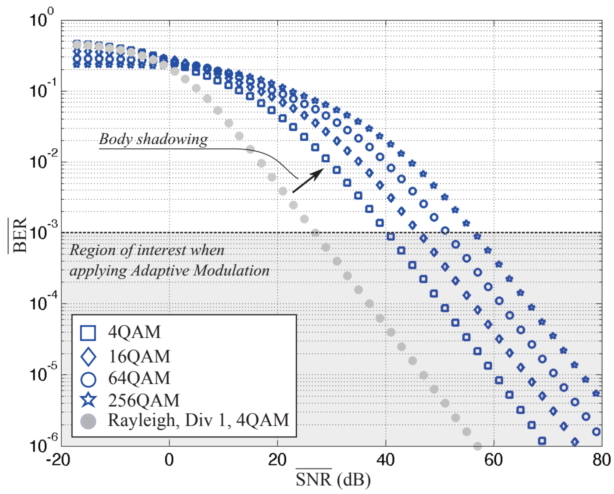

Figure 6.2: Mean BER performance for two spatial subchannels, of all four modulations supported by the IEEE 802.11ac standard

6.4 Transmission blocking modulation

6.4.1 Transmission blocking fixed subcarrier modulation

In this section, we analyze the performance of a wireless body-to-body system which uses perfect Channel State Information (CSI) to ensure a $\overline{\text{BER}} \leq \text{BER}_{\text{thresh}}$. By means of channel feedback, transmission blocking is applied on subcarriers which experience a SNR < $\text{SNR}_{\text{thresh}}$, leading to a BER > $\text{BER}_{\text{thresh}}$. These non-used subcarriers are "*turned of*", without subcarrier power reallocation, so that the SNR and BER on these non-used subcarriers are not defined whereas the throughput is set to 0 bits/symbol. In contrast, all subcarriers who experience a SNR ≥ $\text{SNR}_{\text{thresh}}$ leading to BER ≤ $\text{BER}_{\text{thresh}}$, are assigned the same subcarrier modulation leading to a subcarrier throughput equal to $\log_2(M)$ bits/symbol. The SNR threshold, defined as the minimum subcarrier SNR which still guarantees BER ≤ $\text{BER}_{\text{thresh}}$, on that specific subcarrier, is calculated as:

$$\text{SNR}_{\text{thresh}} = \frac{Q^{-1}\left(\frac{\text{BER}_{\text{thresh}}.\log_2(M)}{N_b}\right)^2}{\frac{d_{min}^2}{2}}. \tag{6.7}$$

For example, for a BER threshold of 1e-3, the subcarrier modulation may be increased from 4-QAM to either 16-, 64- or 256-QAM, compatible with the 802.11ac standard, when E_b/N_0 per subcarrier is larger than 10.52 dB, 14.68 dB or 19.39 dB, respectively. However, when E_b/N_0 is lower then 6.78 dB, tranmission blocking is applied. The E_b/N_0-values are obtained from the theoretical BER characteristics for AWGN, since adaptive modulation is applied on every time-invariant measurement cycle.

The concept is graphically explained in Fig. 6.3. For spatial subchannel 1, when using transmission blocking 4QAM subcarrier modulation, four subcarriers are unused because their subcarrier SNR is lower than $\text{SNR}_{\text{thresh}}$(4QAM), as yellow-marked. This implies that, for further calculations, the SNR and BER on these four unused subcarriers are not taken into account and that the throughput on these subcarriers is equal to 0 bits/symbol. Additionally, the throughput on all active subcarriers, marked with purple, is equal to 2 bits/symbol. Logically, when employing transmission blocking 16QAM subcarrier modulation, leading to a higher SNR threshold equal to $\text{SNR}_{\text{thresh}}$(16QAM), less subcarriers are used for the same transmit power, as marked in blue for both spatial subchannels. Moreover, for transmission blocking 64 -and 256QAM subcarrier modulation, only six and two subcarriers are used for spatial subchannel 1, respectively, and no subcarriers are used for spatial subchannel 2.

Also note the difference between a quasi-frequency-flat channel, as spatial subchannel 2, and a frequency-selective wideband channel, as spatial subchannel

1, typically occuring due to body-shadowing effects. For the *quasi-frequency-flat* wideband channel, only a small increase in SNR, visualized by the dotted blue line, could bring all subcarriers above, for example, $\mathrm{SNR}_{\mathrm{thresh}}$(16QAM). When applying the same increase in SNR for the *frequency-selective* wideband channel, some subcarriers, which experience deep fading dips, remain under $\mathrm{SNR}_{\mathrm{thresh}}$(16QAM). This implies that less subcarriers are used and, hence, that the mean throughput, defined as $\overline{\mathrm{thr}}$ and calculated by means of Formula (6.8), increases slower with increasing mean SNR.

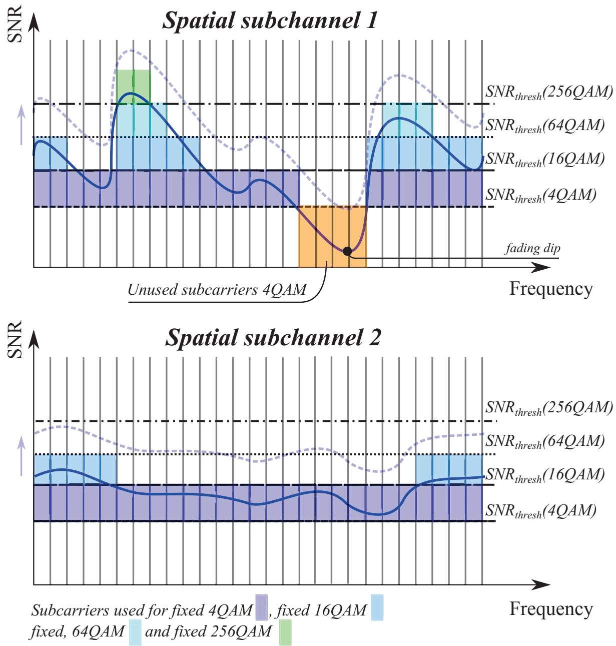

Figure 6.3: Concept of transmission blocking fixed subcarrier modulation

$$\overline{\mathrm{thr}} = \frac{1}{L}\sum_{l=1}^{L}\left(\frac{1}{r}\sum_{i=1}^{r}\left(\frac{1}{N}\sum_{k=1}^{N}\mathrm{thr}_{l,i,k}\right)\right) \tag{6.8}$$

6.4.2 Transmission blocking adaptive subcarrier modulation

When applying transmission blocking adaptive subcarrier modulation, the modulation per subcarrier is not fixed but changes in an adaptive manner whether or not the subcarrier SNR is above the $\mathrm{SNR}_{\mathrm{thr}}$. More specifically, the highest possible modulation order, still guaranteeing a BER $\leq \mathrm{BER}_{\mathrm{thresh}}$, is chosen per subcarrier. This concept is graphically explained in Fig. 6.4 which shows the different subcarrier modulations, depending on the subcarriers SNR's. As an example, for spatial subchannel 1, the subcarrier SNR is above the $\mathrm{SNR}_{\mathrm{thresh}}$(256QAM) for two subcarriers, which implies that the throughput on these subcarriers is equal to 8 bits/symbol, while the BER $\leq \mathrm{BER}_{\mathrm{thresh}}$. Also note that, when SNR $< \mathrm{SNR}_{\mathrm{thresh}}$(4QAM), the subcarriers are not used. For spatial subchannel 2, the subcarrier SNR is above $\mathrm{SNR}_{\mathrm{thresh}}$(16QAM) for nine subcarriers which implies that the throughput on these subcarriers is 4 bits/symbol, while the BER $\leq \mathrm{BER}_{\mathrm{thresh}}$.

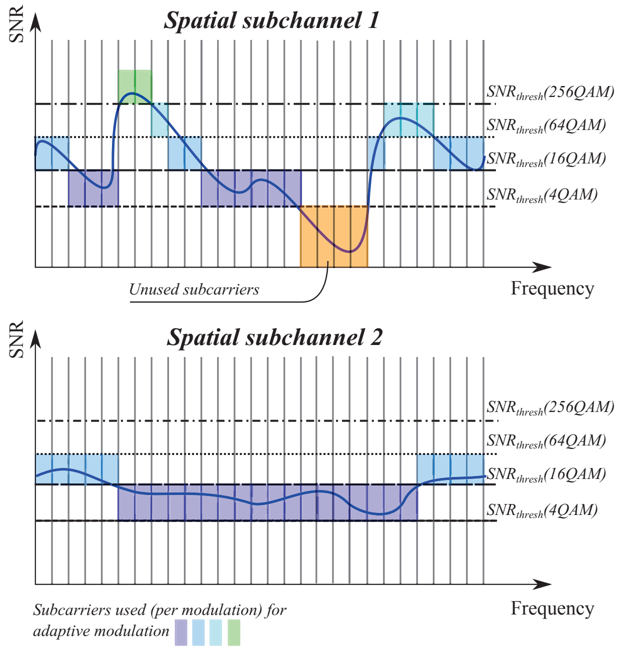

Figure 6.4: Concept of transmission blocking adaptive subcarrier modulation

6.5 Results

Fig. 6.5 presents the BER performance of the four modulations, supported by IEEE 802.11ac, when applying transmission blocking fixed subcarrier modulation, indicated by the different blue markers, with $\mathrm{BER}_{\mathrm{thresh}}$ equal to 10^{-3}. Additionally, the BER performance for the transmission blocking adaptive subcarrier modulation with $\mathrm{BER}_{\mathrm{thresh}}$ equal to 10^{-3}, is visualized by the pink markers. Beyond point A, the SNR of all subcarriers belonging to the strongest, quasi-frequency-flat channel is above $\mathrm{SNR}_{\mathrm{thresh}}$(4QAM). Moreover, the strongest subcarriers of the weakest, frequency-selective spatial subchannel start exceeding $\mathrm{SNR}_{\mathrm{thresh}}$(4QAM) and, hence, start contributing to the $\overline{\mathrm{BER}}$ and $\overline{\mathrm{SNR}}$. However, the SNR of these strongest subcarriers is only a few dB above $\mathrm{SNR}_{\mathrm{thresh}}$(4QAM), which leads to a relatively high BER, still below $\mathrm{BER}_{\mathrm{thresh}}$, causing the flattening of the BER curve. At point B, almost all subcarriers on both spatial subchannels are 4QAM modulated. The effect of transmission blocking adaptive subcarrier modulation is clearly visualized by the pink markers. Between point C and D, the subcarrier modulation switches from 4QAM to 256QAM owing to increasing $\overline{\mathrm{SNR}}$. In this interval, the throughput increases, within the same order of BER magnitude, by switching to higher order modulations. At point C, the majority of subcarriers are still 4QAM modulated whereas at point D, the majority of the subcarrier are 256QAM modulated.

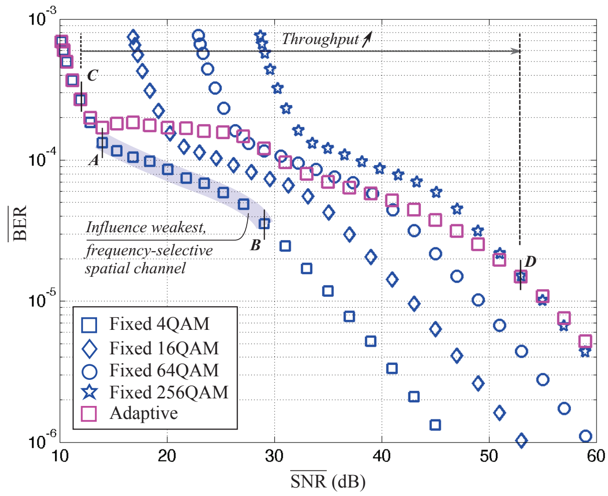

Figure 6.5: Mean BER performance for all four modulations, supported by IEEE 802.11 ac, when applying transmission blocking fixed subcarrier modulation and mean BER performance when applying transmission blocking adaptive subcarrier modulation for a BER $\leq 10^{-3}$

Fig. 6.6 shows that the mean throughput, when applying transmission blocking adaptive subcarrier modulation is always higher than, or equal to, the scenario where transmission blocking fixed subcarrier modulation is applied. For low $\overline{\mathrm{SNR}}$, the adaptive modulation performs the same as fixed 4QAM because no subcarrier SNR is above $\mathrm{SNR}_{\mathrm{thresh}}$(16QAM) and, hence, all active subcarriers are 4QAM modulated. Moreover, the adaptive modulation performs better than fixed 16-, 64- and 256QAM because, for these higher order modulations, the subcarrier SNR do not exceed the corresponding threshold to ensure BER $\leq \mathrm{BER}_{\mathrm{thresh}}$. This implies that transmission on all subcarriers is blocked, leading to a mean throughput equal to 0 bits/symbol. When increasing $\overline{\mathrm{SNR}}$, some subcarriers, which are fixed to 4QAM for transmission blocking fixed subcarrier modulation, switch to 16QAM for transmission blocking adaptive subcarrier modulation, which leads to a higher $\overline{\mathrm{thr}}$ for adaptive subcarrier modulation. When focussing on fixed 256QAM, the throughput of adaptive subcarrier modulation is higher, for $\overline{\mathrm{SNR}} \leq 60$ dB, because much more subcarriers are used with a lower modulation order, leading to a higher $\overline{\mathrm{thr}}$.

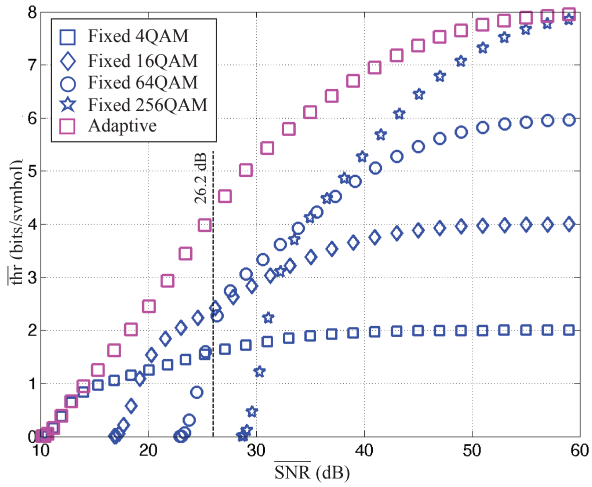

Figure 6.6: Mean throughput for all four modulations, supported by IEEE 802.11 ac, when applying transmission blocking fixed subcarrier modulation and mean throughput when applying transmission blocking adaptive subcarrier modulation for a BER $\leq 10^{-3}$

From a practical point of view, when the transmit power of the 2×2 MIMO-OFDM system is equal to only 1.5 mW, the received SNR on all four SISO links is high enough to ensure reliable timing synchronization and frequency offset estimation. This leads to a received mean SNR equal to 26.2 dB, corresponding to the mean throughputs presented in Table 6.1. The total bitrate R_b, in bps, for the a MIMO-OFDM system with transmission blocking is calculated as:

$$R_b = r.N.\frac{\overline{\text{thr}}}{T_s}. \tag{6.9}$$

Table 6.1 also presents the bitrate, for $\text{BER}_{\text{thresh}}$ equal to 10^{-3}, when assuming 2×2 MIMO-OFDM with 80 MHz OFDM bandwidth, leading to $\text{r} = 2$ spatial subchannels and $\text{N} = 256$ subcarriers. Moreover, the IEEE 802.11ac standard defines T_s equal to 3.6 μs. Table 6.1 clearly shows that the mean throughput, and hence, the total bitrate can drastically increase when employing adaptive subcarrier modulation. The minimal bitrate increase is equal to 261 Mbps when comparing fixed 64QAM ($R_b = 343$ Mbps) with adaptive subcarrier modulation ($R_b = 604$ Mbps).

Table 6.1: mean throughput, in bits/symbol, and corresponding bitrate, in Mbps, when using 1.5 mW transmit power

	4QAM	16QAM	64QAM	256QAM	Adaptive
$\overline{\text{thr}}$	1.59	2.41	2.17	0	4.25
R_b	226	343	309	0	604

6.6 Conclusion

This chapter shows that the throughput and, hence, data rate of a wideband indoor body-to-body channel is drastically increased when using transmission blocking adaptive subcarrier modulation compared to transmission blocking fixed subcarrier modulation. This allows on-duty firefighters to broadcast multimedia and real-time, on-body sensor data which increases their safety when operating in wideband public safety networks.

Acknowledgment

The authors would like to thank IAP BESTCOM and UCL for providing the Elektrobit channel sounder and measurement locations.

References

[1] "LTE-Advanced Evolution in Releases 12 - 14", Nokia Solutions and Networks white paper, Tech. Rep., 2015.

[2] "Public safety mobile broadband", Ericsson white paper, Tech. Rep., 2014.

[3] S. Lemey and H. Rogier, "SIW textile antennas as a novel technology for UWB RFID tags", in *Proceedings of RFID Technology and Applications Conference (RFID-TA)*, Tampere, Finland: IEEE, Sep. 2014, pp. 256–260.

[4] "802.11ac", IEEE Standard for Information technology - Telecommunications and information exchange between systems - Local and metropolitan area networks - Specific requirements - Part 11: Wireless LAN Medium Access Control (MAC) and Physical Layer (PHY) Specifications - Amendment 4: Enhancements for Very High Throughput for Operation in Bands below 6 GHz, Tech. Rep., 2013.

[5] J. Faezah and K. Sabira, "Adaptive modulation for OFDM systems", *International Journal of Communication Networks and Information Security (IJCNIS)*, vol. 1, no. 2, pp. 6260–6265, Aug. 2009.

[6] A. Czylwik, "Adaptive OFDM for wideband radio channels", in *Global Telecommunications Conference Communications (GLOBECOM)*, vol. 1, Nov. 1996, pp. 713–718.

[7] T. Keller and L. Hanzo, "Adaptive modulation techniques for duplex OFDM transmission", *IEEE Transactions on Vehicular Technology*, vol. 49, no. 5, pp. 1893–1906, Sep. 2000.

[8] S. Chung and A. Goldsmith, "Degrees of freedom in adaptive modulation: a unified view", in *53rd Vehicular Technology Conference (VTC)*, vol. 2, May 2001, pp. 1267–1271.

[9] J. Garzas, C. Calzon, and A. Armada, "An energy-efficient adaptive modulation suitable for wireless sensor networks with SER and throughput constraints", *EURASIP Journal on Wireless Communications and Networking*, no. 1, pp. 1–7, 2007.

[10] M. Sudjai, L. Tran, and F. Safaei, "Adaptive space-time-frequency-coded UWB system for wireless body area network", *EURASIP Journal on Wireless Communications and Networking*, no. 1, p. 36, 2015.

[11] A. Goldsmith, *Wireless Communications*. Cambridge University Press, 2005.

[12] H. Suzuki, T. Tran, and I. Collings, "Characteristics of MIMO-OFDM channels in indoor environments", *EURASIP Journal on Wireless Communications and Networking*, vol. 2007, no. 1, pp. 1–9, Dec. 2006.

7
Four-element Ultra-Wideband Textile Cross Array for Dual Spatial and Dual Polarization Diversity

Thijs Castel, Sam Lemey, Patrick Van Torre, Claude Oestges and Hendrik Rogier

Submitted for publication in IEEE Antennas and Wireless Propagation Letters

★ ★ ★

The emergence of miniaturized flexible electronics enables on-duty first responders to collect biometrical and environmental data through multiple on-body sensors, integrated into their clothing. However, gathering these life-saving data would be useless if they cannot set up reliable, preferably high-data rate, wireless communication links between the sensors and a remote base station. Therefore, we have developed a four-element Ultra-Wideband textile cross array, that combines dual-spatial and dual-polarization diversity, and is easily deployable in a first responder's garment. The impedance bandwidth of the array equals 1.43 GHz, while mutual coupling between its elements remains below -25 dB. For a maximal bit error rate of 1e-4, the array realizes a diversity gain of at least 24.81 dB. When applying Adaptive Subcarrier modulation, the mean throughput per OFDM subcarrier increases by an extra bit/symbol when comparing fourth to second order diversity.

7.1 Introduction

Highly reliable communication in indoor environments is vital for first responders' safety. Indeed, ensuring safe working conditions by remotely monitoring their biometrical and sensor data decreases response time and the number of casualties. Transmit and/or receiver diversity by wearable on-body antenna arrays [1], [2] drastically improves link reliability in Wireless Body Area Networks (WBANs) [3], while wideband systems provide the data rates needed to wirelessly communicate pictures and/or videos. Ref. [4] describes Ultra-Wideband spatial and polarization diversity for two-element arrays on a rigid substrate. Furthermore, [5] presents a four-element dual-spatial, dual-polarization broadband slot-coupled patch array on an FR-4 substrate, with only 15 dB isolation between the antenna elements, while [6] and [7] describe Substrate-Integrated Waveguide (SIW) cavity-backed arrays with a single feed line, hence, without applying diversity. In [8], 20.8 mm high metamaterial mushrooms walls increase isolation between neighbouring elements in a MIMO antenna system. Yet, this solution is not applicable for low-profile on-body antenna arrays. Refs. [9] and [2] propose antenna diversity for off-body communication channels at 2.45 GHz and 60 GHz, respectively. Up to now, receiver diversity in body-to-body scenarios is implemented by several, physically separated on-body antennas [10], [11]. However, avoiding multiple fragile RF cables in a first responder's jacket, by deploying a single antenna array, improves robustness and avoids EMC issues. Moreover, all active transceiver and signal processing electronics may be stacked on a feed plane below its ground plane, yielding a compact active antenna module.

Therefore, we propose a novel Ultra-Wideband four-element SIW textile antenna array that exploits dual-spatial and dual-polarization diversity and operates in the low duty cycle restricted [3.4-4.8] GHz band [12], while being unobtrusively and invisibly integrated into the back section of a first responder's jacket. Besides increased reliability through diversity gain, the array realizes additional throughput gain per Orthogonal Frequency Division Multiplexing (OFDM) subcarrier through Adaptive Subcarrier modulation. Moreover, for the first time in literature, the antenna array performance is validated by using it to set up wideband, dynamic SIMO body-to-body links in an indoor office scenario. Section 7.2 describes the antenna array design while Section 7.3 presents simulation and measurements results, together with the indoor measurement scenario and the calculated bit error rate (BER) characteristics.

7.2 Antenna array design

Body-worn applications in the public safety segment impose stringent design requirements to textile antennas, which must be unobtrusively integrated into the first responders' outfits, without hindering their movements nor adding weight.

Good radiation characteristics and impedance matching are essential, even for a textile antenna in close proximity of the human body. This performance must be maintained when operating in harsh environments, to prevent life-threatening situations. SIW cavity-backed slot (CBS) antennas address these specific design challenges [13]. In this chapter, the ultra-wideband SIW antenna in [14] serves as the basic building block for the novel four-element antenna array shown in Fig 7.1. To obtain high radiation efficiency over an ultra-wide impedance bandwidth, in each antenna element a non-resonant rectangular slot splits the rectangular SIW cavity into subcavities A and B. By careful selection of the cavity and slot dimensions, a 50 Ω grounded coplanar waveguide (GCPW) feed line excites two hybrid modes at neighbouring frequencies. Impedance bandwidth enhancement [15] is obtained by merging both modes.

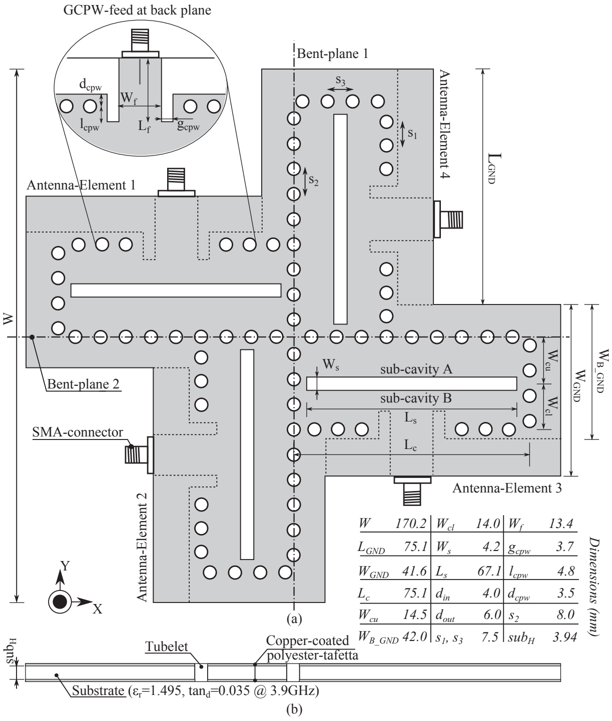

W	170.2	W_{cl}	14.0	W_f	13.4
L_{GND}	75.1	W_s	4.2	g_{cpw}	3.7
W_{GND}	41.6	L_s	67.1	l_{cpw}	4.8
L_c	75.1	d_{in}	4.0	d_{cpw}	3.5
W_{cu}	14.5	d_{out}	6.0	s_2	8.0
W_{B_GND}	42.0	s_1, s_3	7.5	sub_H	3.94

Figure 7.1: Four-element textile antenna array. (a) Front view with enlarged inset for the feed section. (b) Cross-section.

Fig. 7.1 shows four of these linearly-polarized UWB SIW CBS antenna elements (AEs), arranged such that the array exhibits fourfold rotational symmetry. Then, subsequent AEs are orthogonally polarized, while equi-polarized AEs (1&3, and 2&4) are separated by a distance of 75.1 mm, being larger than half the wavelength of the smallest operating frequency. In this way, this specific geometry optimally exploits both spatial and polarization diversity by minimizing correlation between receive signals. In addition, cavity sidewalls are shared, while guaranteeing sufficiently low mutual coupling by optimizing the tubelet-spacing s_3 (Fig. 7.1). A closed-cell expanded-rubber protective foam, typically applied as a protective layer in first responder jackets, is adopted as antenna substrate (ϵ_r=1.495, tanδ=0.035 @ 3.9GHz), whereas the slot and feed layer are implemented in copper-coated Tafetta fabric (surface resistivity 0.18 Ω/sq). Both conductive fabric layers are glued to the substrate by thermally-activated adhesive sheets, after which brass tubular eyelets are inserted to implement the cavities' sidewalls. This specific combination yields a flexible, low-profile and conformal broadband design that facilitates unobtrusive integration. An extensive computer-aided optimization process, carried out in CST Microwave Studio, yields the antenna dimensions (Fig. 7.1) that provide maximal impedance bandwidth ($|S_{11}|$ < -10 dB w.r.t. 50 Ω) within the-low-duty-cycle restricted [3.4-4.8] GHz band, while keeping mutual coupling between elements below -25 dB.

7.3 Measurement results

7.3.1 Antenna array performance

First, the array's performance is validated in an anechoic chamber, by measuring its S-parameters from 3.0 GHz to 5.0 GHz (Fig. 7.2) and its radiation pattern at 3.9 GHz (Fig. 7.3). Given the fourfold rotational symmetry, Fig. 7.2 only depicts the array's $|S_{11}|$, as a measure for an element's impedance matching, and its $|S_{21}|$ and $|S_{31}|$, representing the mutual coupling between elements. A very good agreement between simulations and free-space performance is obtained in Fig. 7.2, with a matching to $Z_0 = 50\ \Omega$ from 3.26 GHz to 4.7 GHz, hence a -10 dB impedance bandwidth of 1.43 GHz, and a very high isolation (> 28.4 dB) between antenna elements.

Furthermore, Fig. 7.3 reveals a stand-alone maximum gain of 4.0 dBi and a front-to-back ratio (FTBR) of 9.6 dB, at 3.9 GHz. In addition, measurements yielded a difference of 12.16 dB between co-polar and cross-polar components along broadside (positive z-direction). Given the fact that the AEs are linearly polarized and that subsequent AEs are orthogonal, providing fourfold rotational symmetry (Section 7.2), we conclude that subsequent AEs achieve polarization diversity. As the array will be worn in close proximity of the human body, its performance was also tested when deployed on the back of a male test person (l=1.79m, w=71kg) as described in Section 7.3.2. Then, Fig. 7.2 reveals only slight changes in the measured S-parameters, whereas Fig 7.3 shows a similar maximum gain of 4.6 dBi and an increase in FTBR to 23.6 dB. Finally, the array's S-parameters were also measured when bent with a radius of 14.2 cm along bent-plane 1 and bent-plane 2 (Fig.7.1), as expected in realistic scenarios. The array maintains its excellent performance under these conditions (Fig.7.2). Note that, in all considered deployment scenar-

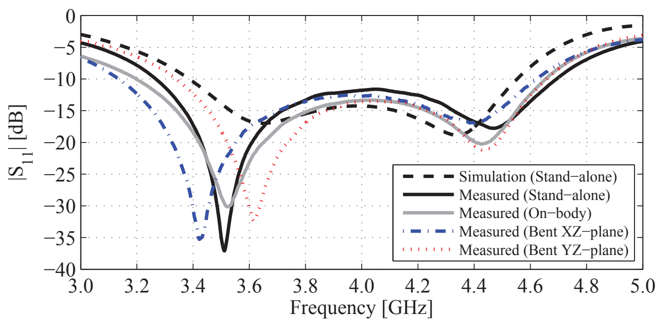

(a)

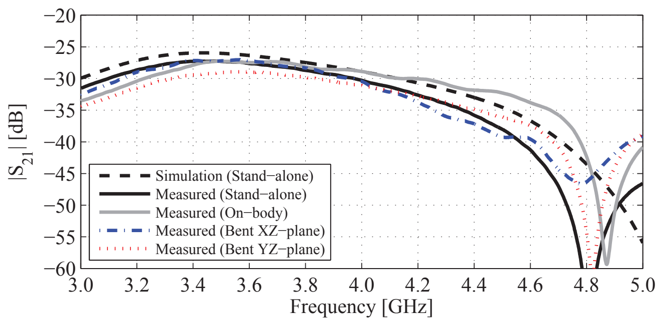

(b)

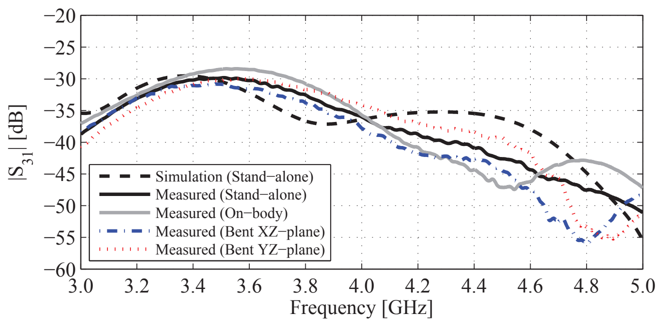

(c)

Figure 7.2: S-parameters of the four-element antenna array under different conditions. (a) Input impedance matching. (b) Mutual coupling between subsequent antenna elements. (c) Mutual coupling between equipolarized antenna elements.

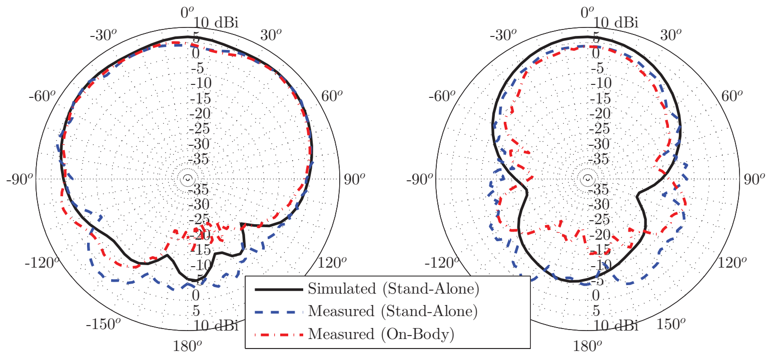

(a) (b)

Figure 7.3: Measured and simulated stand-alone radiation pattern together with the on-body radiation pattern in the E-plane (a) and the H-plane (b), at 3.9 GHz

ios, the measured return loss exceeds 5 dB in the complete low duty cycle restricted [3.4-4.8] GHz band. This makes our UWB antenna an ideal candidate to be worn by a first responder. Moreover, the mean effective gain (MEG), calculated for the indoor multipath environment described in [16], equals -2.8 dBi for AEs 1&3 and -3.4 dBi for AEs 2&4, at 3.9 GHz, which indicates good diversity performance.

7.3.2 Body-to-Body Measurement Scenario

Wideband body-to-body measurements, replicating real-life rescue operations, were performed in an indoor office scenario using the ULB-UCL elektrobit channel sounder with 100 mW TX power, at 3.6 GHz center frequency with 120 MHz useful bandwidth. While the first responder at TX side, equipped with a single SIW textile antenna in the front section of his jacket, scans the hallway, the first responder at RX side, equipped with the novel cross array in the back section of his jacket, scans the offices. There was no Line of Sight (LoS) link between the TX front antenna and the RX cross array at any time, corresponding to a true indoor Non Line of Sight (NLoS) scenario. Measurements were repeated twice for both a vertically and horizontally polarized TX antenna, yielding a total of 60.000 measurement cycles.

7.3.3 Correlation Analysis

For further calculations, the frequency-selective wideband channel is subdivided in 256 frequency-flat subcarriers with a bandwidth of 312.5 kHz, as in the 802.11ac standard [17]. For each of the 256 frequency-flat subcarriers, the complex correlation coefficient ρ between channel samples of two physical channels from the 1×4 SIMO system is calculated. Four separate measurements, each lasting for 197 seconds and gathering 15.000 complex channel samples, are combined. The correlation ρ is calculated based on an array of *60.000 time samples × 256 subcarriers × 4 SISO links*. Because of the time-varying channel, the complex correlation coefficient is evaluated per subcarrier within a measurement window of 1 s. Since both firefighters walk at 0.5 m/s, the path loss remains constant within this window. Hence, the complex correlation coefficient ρ only comprises body shadowing and small-scale fading. To calculate correlation between, for example, signals from AE1 and AE2, a matrix of 60.000×256 complex correlation coefficients is first time-averaged for each OFDM subcarrier, after the mean value is computed over all 256 subcarriers [18].

Table 7.1: Amplitude of the correlation coefficient

	1	2	3	4
1	1	0.41	0.46	0.31
2	0.41	1	0.40	0.31
3	0.46	0.40	1	0.30
4	0.31	0.31	0.30	1

Table 7.1 shows that the correlation coefficients remain well below 0.7. Therefore, the four SISO channels are sufficiently decorrelated to ensure that the SIMO-OFDM channel reliability increases when applying receive diversity on subcarrier basis.

7.3.4 Bit Error Rate

Let P_k be the transmit power allocated to subcarrier k, σ^2 the noise power and $\mathbf{H}_{i,k}$ the channel matrix of subcarrier k from cycle i. Assume constant TX power with constant power spectral density, while the channel is unknown to the transmitter but perfectly known by the receiver. The Signal to Noise Ratio of subcarrier k at cycle i, $\mathrm{SNR}_{i,k}$, is then calculated as $P_k/\sigma^2 \cdot H_{i,k}H_{i,k}^H$ for all four SISO links. Furthermore, when applying Maximal Ratio Combining (MRC) per OFDM subcarrier, the subcarrier SNR (during cycle i) is calculated as the sum over $\mathrm{SNR}_{i,k}$ for the corresponding (two or four) AEs. 1×2 *Spatial diversity* combines two equally-polarized AEs, such as AE1&3 or AE2&4 (Fig. 7.1), whereas 1×2 *polarization diversity* combines two orthogonally-polarized AEs, such as AE1&2, AE2&3, AE3&4 or AE4&1. When applying 1×4 *spatial-polarization diversity*, all four AEs are combined simultaneously. The corresponding BER of subcarrier k at cycle i, for 4-QAM modulation, is calculated as $Q\left(\sqrt{\mathrm{SNR}_{i,k}}\right)$. The mean SNR and mean BER are then found as $1/L\sum_{i=1}^{L}\left(1/N\sum_{k=1}^{N}\mathrm{SNR}_{i,k}\right)$ and $1/L\sum_{i=1}^{L}\left(1/N\sum_{k=1}^{N}\mathrm{BER}_{i,k}\right)$, respectively. The mean SNR is further used to calculate the corresponding $\mathrm{E}_b/\mathrm{N}_0$

per RX antenna as $(1/N_{RX}).(1/\log_2 M).\overline{\mathrm{SNR}}$ with N_{RX} the number of AEs and M the number of constellation points.

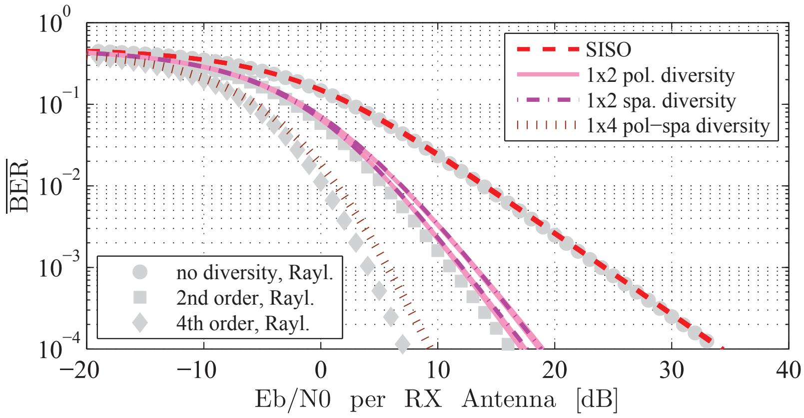

Figure 7.4: Measured BER characteristics for uncoded 4-QAM modulation with equal channel gains (after path loss removal)

Fig. 7.4 shows that 1×4 spatial-polarization diversity is more reliable than 1×2 spatial diversity or 1×2 polarization diversity. For example, for a BER upper limit of 1e-4, the minimal required E_b/N_0 per RX antenna equals 9.36 dB, 17.16 dB, 17.63 dB or even 34.17 dB for 1×4 spatial-polarization, 1×2 polarization, 1×2 spatial and no diversity, respectively. Hence, when applying dual-spatial, dual-polarization diversity for the 1×4 SIMO setup, the required E_b/N_0 per RX antenna is, at least, 24.81 dB lower than for the reference SISO case [19], at the same maximal BER of 1e-4. Due to additional body shadowing, the channels perform slightly worse than (simulated) Rayleigh fading. Note that the x-axis represents E_b/N_0 per RX antenna, to include both the effects of diversity and array gain.

7.3.5 Throughput

When channel state information is available at the transmitter, frequency selectivity can be exploited through Adaptive Subcarrier modulation, which increases the subcarrier throughput for a given BER threshold. For example, for a BER threshold of 1e-4, the subcarrier modulation may be increased from 4QAM to either 16-, 64- or 256-QAM, compatible with the 802.11ac standard, when E_b/N_0 per subcarrier is larger than 12.19 dB, 16.49 dB or 21.18 dB, respectively. These E_b/N_0-values are obtained from the theoretical BER characteristics for additive white Gaussian noise, since the subcarriers experience frequency-flat fading. The mean throughput is calculated as the mean over N subcarriers and L measurement cycles.

Fig. 7.5 shows that 1×4 spatial-polarization diversity increases (mean) throughput compared to second-order diversity, when E_b/N_0 per RX antenna is between

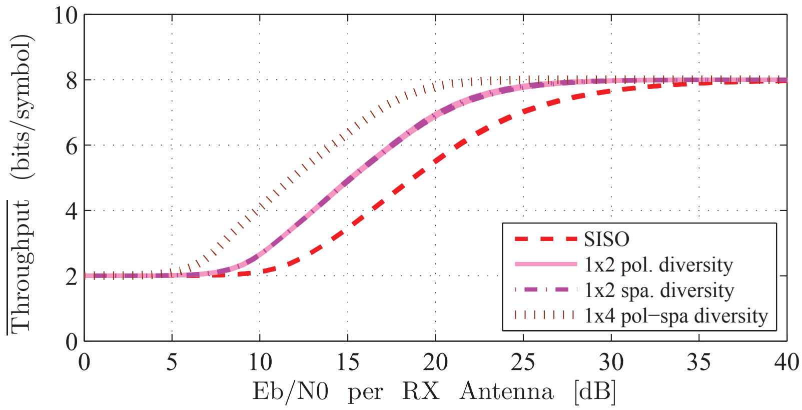

Figure 7.5: Neasured mean throughput when applying Adaptive Subcarrier Modulation for BER ≤ 1e-4 (after path loss removal)

5 dB and 30 dB. In this specific range, the modulation order of some subcarriers may be increased for 1×4 spatial-polarization diversity versus 1×2 polarization-, 1×2 spatial- and no diversity. Moreover, when assuming a received E_b/N_0 equal to 10 dB, which is sufficient for reliable timing and frequency offset estimation on each receiver branch, the BER is above 1e-3 for 1×2 spatial or polarization diversity (Fig. 7.4). However, for 1×4 spatial-polarization diversity, the corresponding BER remains below the pre-set 1e-4 upper BER. This motivates the need for a fourth-order receiver diversity system to guarantee reliable communication at lower E_b/N_0 values. Moreover, by applying Adaptive Subcarrier modulation, an extra bit/symbol can be transmitted for 1×4 spa.-pol. diversity compared to second order diversity, when E_b/N_0 equals 10 dB.

7.4 Conclusion

A new, compact four-element textile cross array that exploits dual-spatial and dual-polarization receiver diversity was proposed. 1×4 spatial-polarization diversity guarantees a minimum diversity gain of 24.81 dB, when assuming a maximal BER of 1e-4. Additionally, when comparing fourth- to second order diversity, the mean throughput per subcarrier was increased by an extra bit/symbol through Adaptive Subcarrier modulation. This makes the novel antenna array topology suitable for highly reliable, high-data rate body-to-body communication between first responders in indoor office environments.

Acknowledgment

The authors thank IAP BESTCOM and UCL for providing the Elektrobit channel sounder and measurement locations.

References

[1] M. Lucia Scarpello, L. Vallozzi, H. Rogier, and D. Vande Ginste, "High-gain textile antenna array system for off-body communication", *International Journal of Antennas and Propagation*, vol. 2012, p. 12, 2012.

[2] N. Chahat, M. Zhadobov, S. Muhammad, L. Le Coq, and R. Sauleau, "60 GHz textile antenna array for body-centric communications", *IEEE Transactions on Antennas and Propagation*, vol. 61, no. 4, pp. 1816–1824, Apr. 2013.

[3] A. Serra, I. Khan, P. Nepa, G. Manara, and P. Hall, "Dual-polarization and dual-pattern planar antenna for diversity in body-centric communications", in *Antennas and Propagation Society International Symposium, 2008. AP-S 2008. IEEE*, Jul. 2008, pp. 1–4.

[4] M. Koohestani, A. Hussain, A. Moreira, and A. Skrivervik, "Diversity gain influenced by polarization and spatial diversity techniques in ultrawideband", *Access, IEEE*, vol. 3, pp. 281–286, 2015.

[5] I. Yeom, H. Kim, J. Jung, and C. Jung, "Analysis of spatial/polarization diversity using a broadband slot-coupled patch antenna for the WLAN 802.11A/B/G/N access point", *Microwave and Optical Technology Letters*, vol. 57, no. 5, pp. 1042–1048, 2015.

[6] D. Guan, Z. Qian, Y. Zhang, and Y. Cai, "Novel SIW cavity-backed antenna array without using individual feeding network", *Antennas and Wireless Propagation Letters, IEEE*, vol. 13, pp. 423–426, 2014.

[7] R. Bayderkhani, K. Forooraghi, and B. Abbasi-Arand, "Gain-enhanced SIW cavity-backed slot antenna with arbitrary levels of inclined polarization", *Antennas and Wireless Propagation Letters, IEEE*, vol. 14, pp. 931–934, 2015.

[8] G. Zhai, Z. N. Chen, and X. Qing, "Enhanced isolation of a closely spaced four-element MIMO antenna system using metamaterial mushroom", *Antennas and Propagation, IEEE Transactions on*, vol. 63, no. 8, pp. 3362–3370, Aug. 2015.

[9] P. Van Torre, M. Lucia Scarpello, L. Vallozzi, *et al.*, "Indoor off-body wireless communication: Static beamforming versus space-time coding", *International Journal of Antennas and Propagation*, vol. 2012, no. 3, p. 13, Mar. 2012.

[10] S. Cotton, W. Scanlon, and A. McKernan, "Improving signal reliability in outdoor body-to-body communications using front and back positioned antenna diversity", in *Antennas and Propagation (EUCAP), 2012 6th European Conference on*, Mar. 2012, pp. 3393–3396.

[11] S. Cotton and W. Scanlon, “Channel characterization for single- and multiple-antenna wearable systems used for indoor body-to-body communications”, *IEEE Transactions on Antennas and Propagation*, vol. 57, no. 4, pp. 980–990, Apr. 2009.

[12] “Specific UWB Applications in the bands 3.4-4.8 GHz and 6.8-8.5 GHz Location Tracking Applications for Emergency Services (LAES), Location Tracking Applications Type 2 (LT2) and Location Tracking and Sensor Applications for Automotive and Transportation Environments (LTA)”, Electronic Communications Committee (ECC), Tech. Rep., Oct. 2011.

[13] S. Agneessens, S. Lemey, T. Vervust, and H. Rogier, “Wearable, small, and robust: The circular quarter-mode textile antenna”, *Antennas and Wireless Propagation Letters, IEEE*, vol. 14, pp. 1482–1485, 2015.

[14] S. Lemey and H. Rogier, “SIW textile antennas as a novel technology for UWB RFID tags”, in *Proceedings of RFID Technology and Applications Conference (RFID-TA)*, Tampere, Finland: IEEE, Sep. 2014, pp. 256–260.

[15] G. Luo, Z. Hu, W. Li, X. Zhang, L. Sun, and J. Zheng, “Bandwidth-enhanced low-profile cavity-backed slot antenna by using hybrid SIW cavity modes”, *Antennas and Propagation, IEEE Transactions on*, vol. 60, no. 4, pp. 1698–1704, Apr. 2012.

[16] K. Ogawa and T. Matsuyoshi, “An analysis of the performance of a handset diversity antenna influenced by head, hand, and shoulder effects at 900 MHz: Part I. effective gain characteristics”, *IEEE Trans. Veh. Technol*, vol. 50, no. 3, pp. 830–844, 2001.

[17] “802.11ac”, IEEE Standard for Information technology - Telecommunications and information exchange between systems - Local and metropolitan area networks - Specific requirements - Part 11: Wireless LAN Medium Access Control (MAC) and Physical Layer (PHY) Specifications - Amendment 4: Enhancements for Very High Throughput for Operation in Bands below 6 GHz, Tech. Rep., 2013.

[18] H. Suzuki, T. Tran, and I. Collings, “Characteristics of MIMO-OFDM channels in indoor environments”, *EURASIP Journal on Wireless Communications and Networking*, vol. 2007, no. 1, pp. 1–9, Dec. 2006.

[19] K. Ogawa and J. Takada, “An analysis of the effective performance of a handset diversity antenna influenced by head, hand, and shoulder effects. a proposal for a diversity antenna gain based on a signal bit error rate and analytical results for the PDC system”, *ELECTRON COMM JPN 2*, vol. 84, no. 6, pp. 10–23, 2001.

Conclusions

General conclusions

In this dissertation, we have presented some practical implementations of multi-antenna systems for body-centric communication networks. Moreover, we have carefully replicated real-life scenarios for both in-body and body-to-body communication channels.

In the first part of this book, we have set up an experimental link between a small dipole antenna, placed inside a human body phantom filled with a muscle mimicking tissue, and an eight-element multi-antenna system, placed on the outside of the human body phantom. By fully exploiting spatial receive diversity, we guarantee a sufficiently high Signal to Noise Ratio to enable live video streaming between the insulated dipole antenna and the wearable multi-antenna system, consisting of six sidewall and two bottom/back antennas. We have focused on high-data rate communication between the dipole, potentially implemented in a wireless endoscopy capsule, and the multi-antenna system, which can be integrated inside a jacket worn by the patient. If the TX power is limited to only 10 mW, all eight receive antennas are required to allow live video streaming. However, when doubling the TX power to 20 mW, equal to the maximum allowed transmit power according to the SAR specifications, only the six sidewall antennas are needed to guarantee live video streaming with a bandwidth of 1 MHz and a bit rate of 3.5 Mbit/s. From a practical point of view, the patient could wear a jacket with only six integrated side antennas, avoiding two uncomfortable antennas at the back section, to guarantee a high-quality in-to-out body link, regardless of the position and orientation of the small dipole antenna in the wireless endoscopy capsule. Moreover, it is very interesting to notice that a video link from an implantable device to a multi-antenna system may be set up with only a single simple dipole antenna inside the implant. This decreases costs, size and complexity of future in-body communication links and increases the battery life of these autonomous devices.

The second part of this book, comprising Chapters 4 up to 7, discusses wideband, body-to-body measurements between two dynamic firefighters in an indoor office scenario. During these measurements, all procedures and techniques performed during a real intervention were carefully reproduced in real time, such that all the effects of body postures, relative orientation and distance between the two members of the Rapid Intervention Team are reflected in the channel data. First, we have developed a simplified indoor office model which is further used to apply a ray tracing algorithm. Owing to the good agreement between measurement and ray tracing results, the simplified indoor office model is proven very accurate and, hence, very useful for dimensioning new communication systems in these environments. Moreover, by considering the RMS delay spread and 50% correlation bandwidth, the LTE, LTE-D2D, 802.11ac and 802.11n standards are proven suitable for future wideband indoor body-to-body networks, a purpose for which they were originally not designed. More in general, it is interesting to note that these standards, designed for communication with a fixed access point such as Wi-Fi, are suitable for indoor body-to-body networks, experiencing more difficult radiowave propagation conditions. Next to the varying fading and body shadowing effects at both ends of the link, also highly variable signal fluctuations are experienced due to the constant reorientation of both members of the Rapid Intervention Team. Chapter 5 presents the calculation of SISO-, SIMO-, MISO- and MIMO-OFDM capacities for realistic indoor broadband body-to-body communication channels, considering maximally two transmit and two receive antennas. With only 1.5 mW transmit power, which is sufficient to guarantee reliable timing synchronization and frequency offset estimation, and no channel-state information at the transmitter, a 2x2 MIMO-OFDM channel capacity equal to 3.67 bps/Hz is guaranteed during 90% of the time. When assuming only 20 MHz OFDM bandwidth, which is the minimal OFDM bandwidth in the 802.11ac standard, this is definitely sufficient, even with a code rate of 1/2, to ensure efficient communication of potentially life-saving information between firefighters. Additionally, when channel state information is available at both the transmitter and receiver, enabling waterfilling MIMO-OFDM by allocating more power to stronger channels, only a relatively small 0.39 bps/Hz and 0.42 bps/Hz extra channel capacity is obtained when applying one- and two-dimensional waterfilling, respectively. This implies that implementing complex channel feedback is not essential to guarantee real-time, efficient communication between two dynamic firefighters in close proximity of each other. Moreover, even at lower bandwidths, when only using two high-performance on-body transmit and receive antennas, the achieved capacity is already sufficiently high for transferring live sensor data, pictures and videos between dynamic firefighters. Additionally, an energy-efficient 2×2 MIMO system may be more suitable for indoor body-to-body communication networks than higher-order MIMO systems, which provide higher data rates at the cost of larger power consumption. In general, when a wideband channel is available, we can conclude that high data rates are achieved with only limited transmit power and a limited number of on-body antennas. Moreover, our numerical results show that it is not beneficial to implement (complex) waterfilling algorithms in wideband indoor body-to-body channels. Chapter 6 presents a subcarrier-based adaptive modulation scheme that could increase the total throughput, given a maximal Bit Error Rate. This technique, known as Adaptive Subcarrier modulation, adapts the modulation order on a subcarrier basis depending on the subcarrier's received Signal to Noise Ratio. This increases the number of bits/symbol that are sent over one subcarrier and, hence, the total throughput. Moreover, the data rate could be further increased when using transmission-blocking adaptive subcarrier modulation compared to transmission-blocking fixed subcarrier modulation. Finally, in Chapter 7, we have shown that our novel four-element wideband antenna array, designed for use in the low duty-cycle restricted [3.4-4.8] GHz band, combines dual spatial and dual polarization diversity. The impedance bandwidth of the array equals 1.43 GHz, while mutual coupling between its elements remains below -25 dB. Additionally, by validating the antenna array's performance through a dynamic 1×4 SIMO body-to-body link, we have shown that the array realizes a diversity gain of at least 7.8 dB, for a maximal bit error rate of 1e-4. Moreover, when applying Adaptive Subcarrier modulation, the mean throughput per OFDM subcarrier increases by an extra bit/symbol when comparing fourth to second-order diversity. This makes the novel antenna array topology suitable for highly reliable, high-data rate body-to-body communication between first responders in indoor office environments.

Future outline

This thesis serves as the basis for future research and development of practical wireless body-centric communication systems. Multiple improvements, extensions and new ideas may be implemented to evolve towards real, autonomous transceivers for, on the one hand, in-body and body-to-body communication systems and, on the other hand, the encryption of wireless body-centric communication networks. Considering in-to-out body communication, the on-body antenna positions and topologies may be optimized to further decrease the required number of receive antennas. This increases patient comfort and total system costs. Moreover, the textile antennas should be unobtrusively integrated inside an actual jacket, worn by the patient, instead of mounted on the human body phantom. Additionally, the simple dipole antenna could be replaced by other, more efficient or smaller, implantable antenna topologies, as already described in the work entitled *Design of an implantable slot dipole conformal flexible antenna for biomedical applications* by Dr. Maria Lucia Scarpello. Taking into account the high-data rate applications for our public safety body-to-body networks, a new adaptive algorithm, combining power reallocation and adaptive subcarrier modulation, could be developed. This new algorithm further increases the throughput and, hence, the data rate in future public safety networks, enabling real-time communication of sensor data, pictures and videos. We could also analyze the performance of a new, simplified, adaptive subcarrier modulation algorithm that adapts the modulation order of multiple subcarriers at once instead of each subcarrier individually. This decreases the amount of link feedback and, hence, the system complexity. Furthermore, to create compact, autonomous on-body transceivers, active electronics and energy harvesters could be implemented on the feed plane of individual on-body antennas or of the wideband antenna array. Future work concerning our new RSS-based encryption algorithm, described in the appendix, involves more in depth-testing and analysis. Moreover, the scenario with a mobile eavesdropper, located on the body of the legitimate parties, should be tested to replicate the worst case scenario.

A

RSS-based Secret Key Generation for Indoor and Outdoor WBANs using On-Body Sensor Nodes

Thijs Castel, Patrick Van Torre and Hendrik Rogier

Based on an article presented at the International Conference on Military Communications and Information Systems and on an article presented at the 10th European Conference on Antennas and Propagation

★ ★ ★

Data security is an important issue in all fields of wireless communication. When encryption is employed, the strength of the key determines the degree of information security. Many encryption algorithms exist, but a high computational complexity is often required to limit the vulnerability to attacks. However, for wireless sensor nodes, a computationally less intensive algorithm is desired, requiring less processing power. In case of body-to-body wireless sensor communication, a highly unobtrusive node can be manufactured by integrating electronic circuitry onto a textile antenna platform. The signal propagation in case of body-to-body communication between walking persons is highly influenced by changing path loss, shadowing by obstacles and the human body, multipath fading, reorientation of the antennas and changes in posture of the walking persons. All these factors contribute to a rapidly fluctuating received signal level when persons are moving around while communicating sensor data. If the transceiver units can switch between transmit and receive modes fast enough, it is possible to communicate in both directions well within the coherence time of the channel, guaranteeing highly correlated RSS values. The channel-state information, available at both sides of the link, is acquired by independent physical measurements. These data are highly correlated and contain significant mutual information owing to the physical properties of the body-to-body radio channel. Moreover, channel-state information acquired by an intruder is substantially decorrelated, as soon as the distance to the intruder is more than a few wavelengths.

Moreover, given that the market of wearables is in so-called hypergrowth mode, more and more of these on-body devices will interact with each other. These body-to-body, device-to-device links should not only provide reliable but also secure communication of personal user data. Therefore, we have analyzed the potential of using the unique reciprocal body-to-body channel between two legitimate parties, to create a high-level security key that is unknown to an eavesdropper. Both randomly moving legitimate parties, typically called Alice and Bob, were equipped with low-power wireless on-body sensor nodes, which collect the Received Signal Strength values. Additionally, the eavesdropper Eve, who is continuously sniffing the body-to-body channel using a third sensor node, collects her own sequence of RSS values, which are expected to be highly decorrelated from the RSS values from both Alice and Bob. Based on a statistical analysis, applied to Received Signal Strength values to verify the correlation, entropy and mutual information, the body-to-body link seems very suitable for RSS-based secret key generation in indoor and outdoor Wireless Body Area Networks. Moreover, this practical and leightweight alternative for secret key generation ensures low on-chip complexity and, hence, low computational power consumption.

A.1 Introduction

In the near future, people will be connected to the internet through multiple wearables which could autonomously communicate personal data towards desired recipients, creating the Internet of People (IoP) [1], [2]. These new Wireless Body Area Networks (WBANs) will go hand in hand with the Internet of Things (IoT) concerning healthcare, fitness monitoring and lifestyle computing [3]. Of course, for users' safety and privacy, data protection is necessary to prevent that intruders could access personal, and hence, sensitive data when wireless data transfer is in progress. Moreover, since power consumption is crucial for on-body devices, the proposed secret key generation algorithm should require low computational complexity with limited memory size and bandwidth [4]. Therefore, the unique characteristics of the underlying reciprocal body-to-body channel between two mobile legitimate parties are exploited to generate joint randomness between both.

We have performed several mobile body-to-body (Alice-to-Bob and vice versa) measurements at indoor and outdoor locations, with a passive stationary eavesdropper (Eve) in the vicinity of both Alice and Bob. The legitimate parties, Alice and Bob, are equipped with low-power wireless nodes, placed upon the human body, to set up autonomous communication towards each other. Moreover, we assume that the passive eavesdropper, represented by a third wireless node, is only capable of calculating the Received Signal Strength (RSS) from intercepted packets sent by Alice or Bob. If Alice transmits a packet towards Bob and Bob retransmits a packet towards Alice within the coherence time of a fast fluctuating wireless body-to-body channel, the RSS at Alice and Bob is expected to be approximately equal owing to reciprocity. In contrast, the RSS at the eavesdropper is expected to be significantly different or decorrelated from the quasi-equal RSS values received by Alice and/or Bob. These unique streams of RSS values at both legitimate parties could further be used to generate a secret key, which is unknown for an intruder. The collected RSS sequences are suitable for secret key generation if the entropy and the Mutual Information (MI) between both legitimate parties are high, whereas the mutual information between a legitimate user and an eavesdropper should be low. For an intruder, this complicates deciphering the secret key and, hence, maximizes data security. Therefore, we have analyzed the correlation, entropy and mutual information of all collected RSS sequences, for three indoor and four outdoor measurement scenarios, indicating the potential to use unique RSS sequences for secret key generation.

To the authors' best knowledge, this is the first work where fully-autonomous low-power nodes were placed upon the human body for RSS-based secret key generation, between two moving legitimate parties in the presence of a stationary eavesdropper, and where the quality of the key was validated based on indoor and outdoor measurements. Despite the fact that this is a relative new research domain, J. Jenssen et al. have already presented interesting work concerning secret key generation based on RSS values, albeit not in a body-centric context. Linked to our work, [5] explores the effectiveness of using highly reconfigurable antennas to generate varying channels which are used to establish secret encryption keys. Additionally, [6] shows that sufficient (and random) movement is necessary to generate high entropy keys between two mobile devices. The chapter is further organized as follows. Section A.2 describes the measurement setup, scenario and location, Section A.3 presents the statistical results and Section A.4 shows the key-generating performance. Finally, in Section A.5, we outline potential future work since this work is only the (fundamental) beginning of RSS-based secret key generation for indoor and outdoor WBANs using on-body sensor nodes.

A.2 Measurement setup

Wireless on-body sensor nodes, composed of a dual-polarized textile patch antenna that serves as a platform for the flexible electronic circuits, were deployed on the bodies of test persons [7]. The on-body sensor nodes placed upon Alice and Bob operated fully-autonomous while Eve's on-body sensor nodes was connected to a laptop, which was used as the central storage for all RSS values of one measurement: RSS from Alice to Bob (RSS_{AB}), RSS from Bob to Alice (RSS_{BA}), RSS from Alice to Eve (RSS_{AE}) and RSS from Bob to Eve (RSS_{BE}). As visualized in Fig. A.1, the dedicated embedded software was programmed as follows:

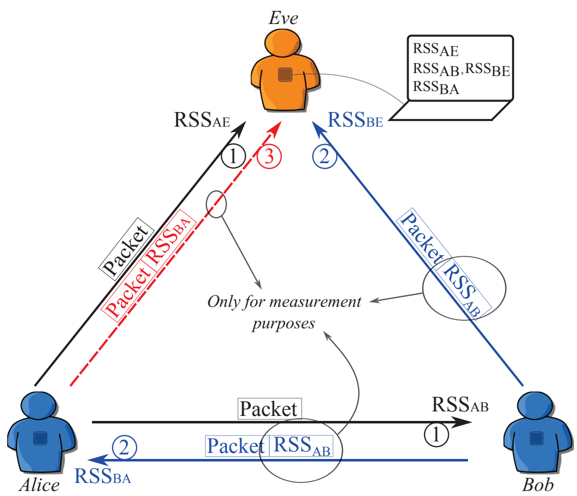

Figure A.1: Measurement principle. The value RSS_{AB} and the transmission from Alice to Eve that includes RSS_{BA} are only included for measurement purposes and not for the actual applications.

1. Alice transmit a packet towards Bob who calculates RSS_{AB}. Moreover, the packet is also received by Eve who calculates (and saves) RSS_{AE}.
2. Bob retransmits a packet towards Alice, who calculates RSS_{BA}, and he includes, only for measurement purposes and not in the actual application, RSS_{AB}. Additionally, the retransmitted packet is received by Eve, who calculates RSS_{BE} and saves both RSS_{BE} and the included RSS_{BA} on the laptop.
3. For measurement purposes only and not in the actual application, Alice retransmit a packet which includes RSS_{BA} towards Eve, who stores this value on the laptop.

In real-life scenarios, Alice and Bob do not (re)transmit packets which include RSS_{AB} or RSS_{BA} because the secret key generation is based on these unique values. However, since only Eve could save the RSS values, this was necessary for measurement purposes.

Three measurement scenarios, with legitimate parties Alice and Bob simultaneously moving around in the presence of a stationary eavesdropper Eve, were performed at an indoor and outdoor location. At the indoor office location, a lot of potential reflectors and scatterers were present in the close vicinity of Alice, Bob and Eve. In contrast, at the urban outdoor location, all three parties were surrounded by high buildings, on the one side, and high townhouses, at the opposite side of the river, as shown in Fig. A.3. Note that no cars where passing by during the outdoor measurements. In the first and second scenario, Alice and Bob, randomly moving around, remained in Line-of-Sight (LoS) of each other, as shown in Fig. A.2. However, in the first scenario, Eve is visible to both Alice and Bob whereas, in the second scenario, Eve is at a NLoS position from Alice and Bob. In the third scenario, Eve is visible to both Alice and Bob, who do not see each other. Furthermore, one additional outdoor measurement, corresponding to scenario 1b (Fig. A.3), was performed with Alice and Bob, being in each other's LoS, randomly moving around at the opposite side of the river with a LoS link towards Eve.

For one measurement scenario, we gathered one set of four RSS values every 100 milliseconds for a total of 15.000 sets of RSS values. If the received RSS value, further digitized in an 8 bit value, was below the detection limit of the on-body sensor, the value was dropped and a new packet was sent by Alice to gather 15.000 reliable sets of RSS values. Note that the round trip time between Alice and Bob was only 5 milliseconds, and hence within the coherence time of the channel, estimated as 6.12 milliseconds when both mobile perons are walking at 0.5 m/s:

$$f_{dM} = \frac{v \cdot f}{c}, \tag{A.1}$$

$$T_{coh} \approx \frac{1}{f_{dM}}, \tag{A.2}$$

with f_{dM} the maximum Doppler frequency shift and c the speed of light.

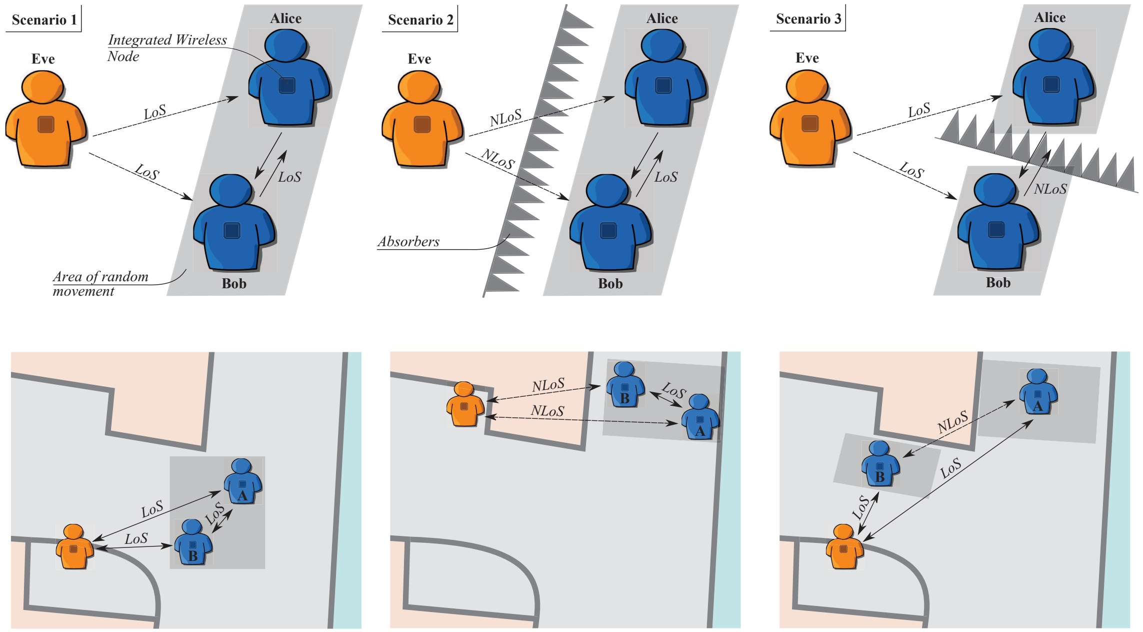

Figure A.2: Measurement scenarios 1, 2 and 3, for both the indoor and outdoor measurement locations. Note that outdoor scenario 1b is depicted in Fig. A.3.

Figure A.3: Outdoor measurement location and measurement scenario 1b. The top left photo, included to provide more insight into the outdoor measurent location, was taken by Alice during measurement scenario 1b. Note that the on-body sensor node is covered by Bob's jacket

A.3 Results

A.3.1 Envelope Correlation

To create a highly-reliable security key from the RSS values, the envelope correlation ρ between $\mathrm{RSS_{AB}}$ and $\mathrm{RSS_{BA}}$ should be high whereas the signal strengths, received by Eve, should be sufficiently decorrelated from $\mathrm{RSS_{AB}}$ and $\mathrm{RSS_{BA}}$.

With $\mathbf{X}$ and $\mathbf{Y}$, being vectors containing 15.000 RSS samples (in dBm), the envelope correlation is calculated as:

$$\rho_{\mathrm{X,Y}} = \frac{E(\mathbf{X}\cdot\mathbf{Y}) - E(\mathbf{X})E(\mathbf{Y})}{\sqrt{\left[E(\mathbf{X}^2) - (E(\mathbf{X}))^2\right]\left[E(\mathbf{Y}^2) - (E(\mathbf{Y}))^2\right]}}. \tag{A.3}$$

As seen in Table A.1, which presents the envelope correlation ρ for all measurement scenarios at both the indoor and outdoor measurement locations, the correlation between AB-BA is significantly higher than the correlation with RSS values received by Eve. This indicates that the received signal strength values may be used to generate a high-level security key. Note that the correlation is calculated on RSS samples in dBm since these values are directly provided by the on-body sensor nodes. Moreover, based on these RSS samples (in dBm), quantization is performed as shown in Section A.4. However, given the fact that correlation is typically performed on linear samples, we should be carefull when drawing general conclusions about the physical body-to-body channel.

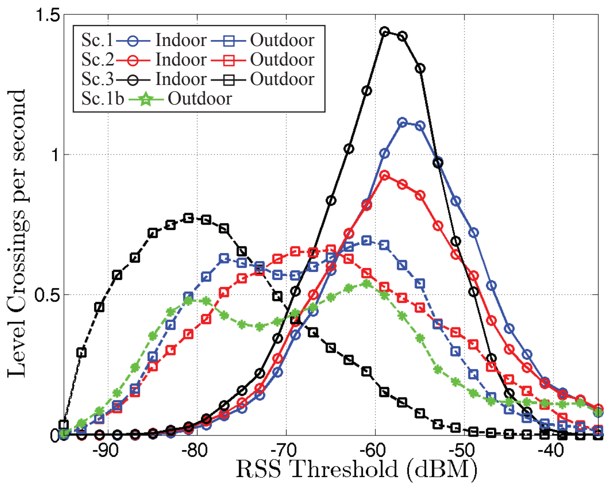

Figure A.4: Level Crossing Rate (LCR) for the Alice-to-Bob link

At the indoor measurement location, a large number of potential reflectors are in the close proximity of Alice and Bob. In contrast, at the outdoor locations, the potential scatterers contributing to the received signal at Alice or Bob are further away from both legitimate parties. This implies that, when both Alice and Bob are simultaneously and randomly moving around, the indoor body-to-body channel could vary faster, compared to the outdoor body-to-body channel. For the Alice-Bob link, this is verified by means of the Level Crossing Rate (LCR), as visualized in Figure A.4. Additionally, the faster varying indoor body-to-body links decrease the coherence time and, hence, increase the probability that RSS_{AB} and RSS_{BA} exhibit, to a small extent, more decorrelation within the round-trip time between Alice and Bob. Moreover, when focusing on the indoor measurements, the correlation between RSS_{AB} and RSS_{BA} is the smallest for scenario 3, because of the faster varying channel, compared to scenarios 1 and 2, as shown in Fig. A.4. Given the NLoS link between Alice and Bob in scenario 3, the correlation with Eve is somewhat higher at both the indoor and outdoor locations, because communication between Alice and Bob only happens via reflectors, which may be in the close vicinity of Eve. Additionally, for outdoor scenarios 1 and 3, the correlation between AB-AE (and BA-AE) is unexpectedly higher than the correlation between AB-BE (and BA-BE). This could be caused by the fact that, during the (non-perfect) random walks, Bob was regularly standing closer to Eve, compared to Alice. This increases correlation between the Alice-Eve link and the Bob-Alice (and vice versa) link. However, the correlation is still significantly lower than the correlation between Alice and Bob. In contrast, this phenomenon is not noticeable for scenario 1b where the distances Eve-Alice and Eve-Bob were approximately equal during the complete measurement.

Table A.1: Envelope correlation

Link	Indoor			Outdoor			
	1	2	3	1	1b	2	3
AB-BA	0.878	0.912	0.704	0.970	0.975	0.968	0.984
BA-AE	0.032	-0.039	0.144	0.269	0.059	-0.042	0.390
BA-BE	0.044	0.034	0.141	0.077	0.099	-0.073	0.152
AB-AE	0.031	-0.037	0.138	0.270	0.062	-0.040	0.391
AB-BE	0.051	0.020	0.124	0.078	0.063	-0.073	0.149
AE-BE	-0.050	-0.024	0.004	-0.063	-0.024	0.039	-0.064

A.3.2 Entropy

The entropy indicates how many bits of the 8 bit RSS value could be used to generate a safe key towards intruders. It is calculated as:

$$\mathrm{H}(\mathbf{X}) = \sum_{i=1}^{N} P(\mathbf{X}_i) \cdot \log_2\Big(P(\mathbf{X}_i)\Big). \tag{A.4}$$

In an ideal situation, all RSS values, within the detection range of the receiver, have equal probability for every consecutive measurement. Theoretically, this corresponds to maximum entropy equal to 8 bits. For the on-body sensors nodes, the detection limit is equal to -95 dBm whereas the saturation limit equals -35 dBm. This sets the maximal entropy equal to $\log_2(60) = 5.90$ bits, when all RSS values would have the same probability. However, since we are performing real-life measurements, the Most Significant Bits (MSBs) of the 8 bit RSS value will vary slower than the Least Significant Bit (LSBs), and are therefore more predictable. This implies that data, secured with these MSBs, is easier to decipher by an eavesdropper. Therefore, the bits that do not vary fast enough over time are not used to generate secret keys. The calculated entropy, presented in Table A.2, shows that H($\mathbf{X}$) $\in$ [4.765, 5.399] bits or H($\mathbf{X}$) $\in$ [5.295, 5.796] bits for the indoor and outdoor location, respectively.

Table A.2: Entropy (bit)

Link	Indoor			Outdoor			
	1	2	3	1	1b	2	3
AB	5.248	5.391	4.765	5.551	5.796	5.633	5.297
BA	5.234	5.399	4.782	5.547	5.790	5.637	5.295

Table A.2 also indicates smaller entropy when Alice and Bob are inside. As described before, at the indoor measurement location, a large number of possible reflectors are in the close proximity of Alice and Bob. Moreover, these reflectors are not only present on few specific locations, as for the outdoor scenario, but over the full 360° range around Alice and Bob. This implies that, during most of the time, many multipath components contribute to the RSS values, at Alice or Bob, which leads to a narrower RSS distribution for the indoor measurement scenario, as visualized in Fig. A.5 for measurement scenario 3. In contrast, the potential reflectors at the outdoor measurement locations are not equally distributed around Alice and Bob. This implies that the RSS values could fluctuate more, heavily depending on the orientation of both Alice and Bob, because the number of arriving multipaths varies over time. This leads to a broader RSS range, as visualized in Fig. A.5, and, hence, a higher entropy.

A.3.3 Mutual Information

Next to the correlation and the entropy, the mutual information is the third statistical parameter which indicates the potential strength of a secret key. The MI depends on the correlation and the entropy and is calculated as:

$$\mathrm{MI}(\mathbf{X},\mathbf{Y}) = \sum_{i=1}^{N}\sum_{j=1}^{N} P(\mathbf{X}_i,\mathbf{Y}_j)\cdot\log_2\left(\frac{P(\mathbf{X}_i,\mathbf{Y}_j)}{P(\mathbf{X}_i)\cdot P(\mathbf{Y}_j)}\right). \tag{A.5}$$

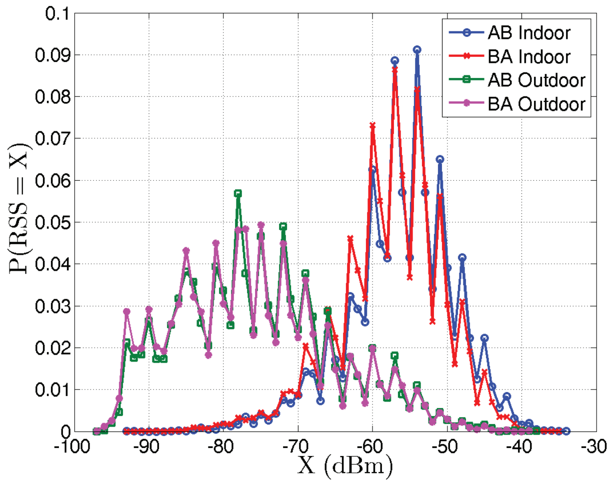

Figure A.5: RSS distribution for scenario 3 at both the indoor and outdoor measurement location

The mutual information indicates how many information bits of the 8 bit RSS_{AB} can be estimated if the 8 bit RSS_{BA} value is known, or vice versa. It measures how the knowledge of RSS_{AB} reduces uncertainity about RSS_{BA}. Similar to the correlation, the mutual information should be high between RSS_{AB} and RSS_{BA} and low between $RSS_{AB,BA}$ and a potential eavesdropper. However, only a high correlation is not sufficient to guarantee high-level secret key. The combination of high correlation and low entropy, as for static body-to-body measurements, results in low MI. In contrast, if both the correlation and entropy are high, the mutual information is high, as for the AB-BA link in outdoor scenario 3, according to Table A.3.

Table A.3: Mutual Information (bit)

Link	Indoor			Outdoor			
	1	2	3	1	1b	2	3
AB-BA	1.398	1.572	0.667	2.386	2.535	2.440	3.053
BA-AE	0.139	0.113	0.108	0.216	0.149	0.096	0.266
BA-BE	0.120	0.110	0.112	0.190	0.172	0.169	0.154
AB-AE	0.133	0.110	0.110	0.214	0.152	0.097	0.261
AB-BE	0.118	0.114	0.108	0.193	0.170	0.173	0.158
AE-BE	0.093	0.700	0.083	0.146	0.084	0.070	0.122

Table A.3 indicates that at least one secret key bit, which will be the same at Alice and Bob, can be generated out of the 8 bit RSS value. However, this will be more difficult for the indoor scenario 3 where Eve is visible for both Alice and Bob, who do not see each other. Because of the fast(er) varying body-to-body channel in this specific scenario, the correlation and, hence, MI between RSS_{AB} and RSS_{BA} is lower.

However, the correlation is expected to be higher if the round-trip time between Alice and Bob could be decreased. The mutual information shared with Eve is, in all scenarios, significantly lower than the mutual information between legitimate parties Alice and Bob. This implies that, even when the MI equals (maximally) 0.266 as in outdoor scenario 3, Eve is not able to estimate one secret bit that is shared by Alice and Bob [8]. Therefore, the unique received RSS sequences at Alice and Bob are proven very suitable for secret key generation for both indoor and outdoor WBANs.

As the RSS values are correlated in time, we employ the mutual information between the RSS sequence and its delayed version as a measure to estimate sufficient independence of subsequent values, as to generate a high-entropy secret key [9]. The mutual information $I(RSS_i, RSS_{i+\tau})$ is displayed in Fig. A.6, and drops below 0.5 bit per sample for a lag of 8 or more samples. We choose to decimate the recorded RSS sequence by a factor 10, leaving 1500 RSS measurements for each scenario.

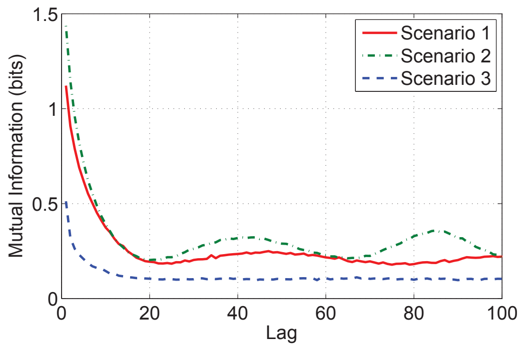

Figure A.6: Mutual Information between RSS and delayed RSS between legitimate parties; $I(RSS_i, RSS_{i+\tau})$ *as a function of* τ

A.4 Key-generating performance

In the remainder, only the indoor measurements are evaluated.

A.4.1 Quantization

Generating keys from the RSS data is a complex issue for which several approaches can be chosen. We choose an RSS quantizer that delivers one key bit per RSS sample, as suggested in [10] and outlined in Fig. A.7.

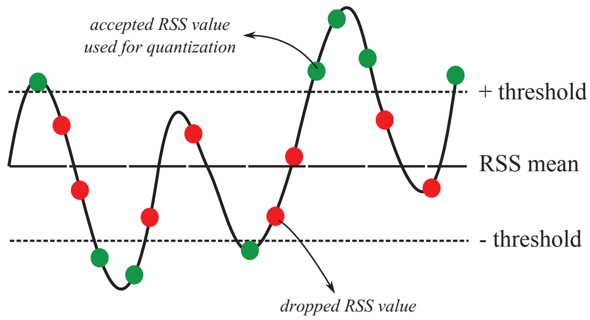

Figure A.7: Quantizer, generating one secret key bit per RSS sample

The quantizer employs the moving average over a number of recent RSS values and if the new value crosses the upper or lower threshold, a 1 or 0 key bit is generated, respectively. This approach provides compensation for asymmetric system parameters, such as small differences in transmit power or receiver noise floor between both legitimate parties.

It is important to note that this type of quantizer drops RSS values that do not cross the threshold, which results in a reduction of the key-generation rate for higher threshold values. In our case the threshold values are expressed in dB.

In a practical application, where Alice generates the reference key and Bob will adjust his key to match her's, Alice will have to inform Bob about which channel samples were skipped, as otherwise their key bit sequences might be shifted with respect to each other. Due to slight propagation channel variations during the measurement, the RSS samples dropped by Alice will indeed not always be the same ones that are also dropped by Bob.

The quantizer delivers binary keys to Alice and Bob, based on the RSS_{BA} and RSS_{AB} sequences, respectively. However, although these binary sequences are highly correlated, they are not identical and a Key Error Rate (KER) can be defined. The key error rate depends on the moving average length as well as on the threshold value.

Fig. A.8 displays the KER as a function of moving average length, without threshold applied. In this case, each value of the decimated RSS series results in a key bit, hence 1500 key bits are generated for each scenario. A minimum occurs for all three scenario's around a moving average length of 7 samples, a value which will be employed for the remaining part of this appendix. Note that for all RSS signals measured by the eavesdropper, the resulting keys all exhibited a $KER \approx 0.5$, confirming the effectiveness of the secret key generation based on the propagation between the legitimate parties.

To illustrate the importance of thresholding, Fig. A.9 displays a scatter plot of the signal levels RSS_{AB} and RSS_{BA}. Without thresholding, each dot represents a secret key bit. Red dots correspond to erroneous bits, where Alice and Bob made different

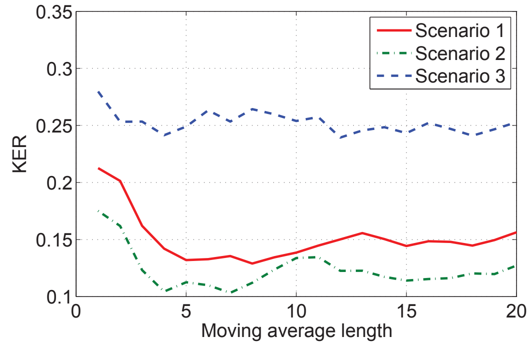

Figure A.8: KER at a threshold of 0 *dB as a function of moving average length*

decisions in the quantization process. The graph clearly illustrates that employing higher thresholds leads to a lower KER, as dots away from the center of the graph are predominantly blue, corresponding to correct key bits.

A higher threshold lowers the KER a the cost of a lower key-generation rate, due to dropped RSS samples. Hence, the threshold should be chosen just high enough to generate an error free key after the error correcting process, further called key reconciliation.

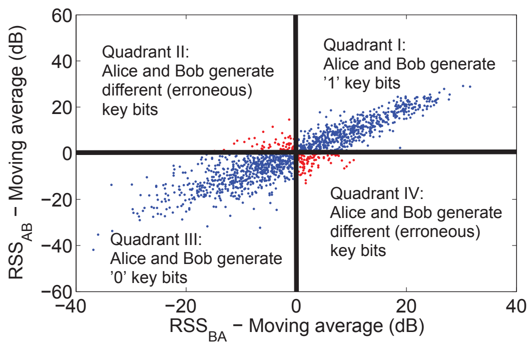

Figure A.9: Correctness of key bits for Scenario 1*. Erroneous bits are concentrated in the center and are (partially) discarded by means of thresholding.*

A.4.2 Key reconciliation

The process of key reconciliation will adjust the keys on both sides of the link, in order to make them match. This process inevitably reveals limited key information over the channel, although this information can also be encrypted using a previously constructed key. A $(15, 11)$-Hamming code is used, with Alice's secret key taken as a reference. Bob's key will be adjusted through forward error correction to match the one of Alice. Alice's key is interleaved to spread errors, which might occur in burst form, over several blocks. The interleaved key is split into 11-bit blocks, 4 check bits are calculated for each block and transmitted to Bob. Bob uses these check bits to correct his own interleaved version of the key.

Revealing 4 check bits, reduces the number of valid 11-bit groups from 2^{11} to 2^7, which should be taken into account. Nevertheless,when choosing an appropriate key length this should not be a problem. Note that keys can be updated regularly, as channel variation is likely to occur during most of the communication time and new key bits are generated continuously.

The KER after reconciliation is displayed in Fig. A.10 and the corresponding key length is shown in Fig. A.11, both as a function of the threshold value employed in the quantizer. An error free key is obtained at a threshold of 5 dB in scenarios 1 and 2, resulting in key lengths of 814 and 891 bits, respectively. For scenario 3, a threshold of 7 dB is required and a much shorter key length of 275 bits results, due to less favorable signal statistics and the higher threshold required consequently.

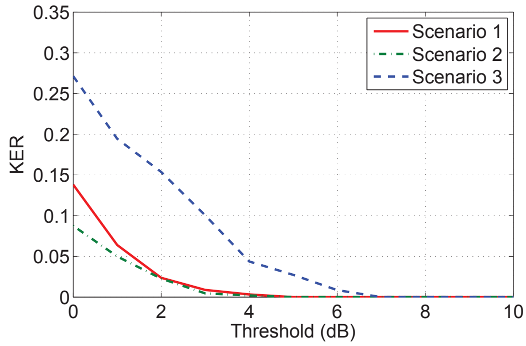

Figure A.10: KER after reconciliation as a function of threshold, for the legitimate parties

Finally, the key generation and reconciliation is also evaluated for the eavesdropper, assuming the eavesdropper has knowledge of the reconciliation algorithm and successfully intercepts all check bits Alice transmits to Bob.

Table A.4: KER after reconciliation for the eavesdropper employing all possible signal combinations

Link, from-to	KER for scenario nr. 1	2	3
BA-AE	0.4727	0.5606	0.2987
BA-BE	0.5152	0.5000	0.3182
AB-AE	0.4628	0.5581	0.3409
AB-BE	0.5011	0.5108	0.3442

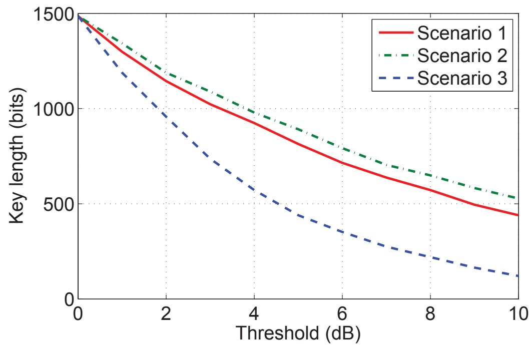

Figure A.11: Key length as a function of threshold, for the legitimate parties

Table A.4 displays the results for keys generated by Eve, for all signal combinations, employing thresholds of 5 dB for scenarios 1 and 2 and a threshold of 7 dB for scenario 3. These thresholds resulted in error free keys for the legitimate parties. Clearly the eavesdropper fails to extract the secret key. In scenarios 1 and 2, Eve's key is totally different. In scenario 3 some information is apparently captured but the key contains too many errors to be of practical use.

A.5 Conclusions

In a first part of the appendix, we have analyzed the correlation, entropy and mutual information of RSS streams, collected using wireless on-body sensor nodes, between two mobile legitimate parties, Alice and Bob, and a stationary eavesdropper, Eve. These statistics, calculated for three indoor and four outdoor measurements, show that stream of RSS values could be used to create joint randomness between two mobile legitimate parties, Alice and Bob. The generated secret key will be (largely) unknown to a stationary intruder, called Eve, owing to the significantly smaller mutual information between the RSS values, received by Alice of Bob, and the RSS values received by Eve. Moreover, the mutual information between Alice and Bob is maximized when both the correlation and entropy are high. From our measurements, higher correlation is obtained for the outdoor measurement scenarios because of the smaller level crossing rate, indicating a larger coherence time. However, correlation in the indoor scenarios is expected to be higher if the round-trip time between Alice and Bob could be decreased. Additionally, due to the non-uniform distribution of potential scatterers in close vicinity of Alice and Bob in the outdoor measurement scenario, the distribution of the RSS values between two legitimate parties is broader, compared to the indoor RSS values for the same measurement scenario. This implies that our outdoor locations could introduce higher entropy, compared to indoor scenarios, which lead to a higher mutual information, assuming high correlation. In the second part of the appendix, practical key generation is performed, employing a computationally low-cost method, easy to implement on the sensor node's microcontroller. The results indicate that error free keys are generated at a rate of approximately one key bit per two seconds for the regular propagation scenarios and at a rate of one bit per six seconds for the worst-case dynamic scenario. Although these key-generating rates are fairly low, strong keys can be generated in a few minutes when legitimate parties are within line-of-sight. A higher rate could be obtained by employing hardware that provides signal strength indication at a higher resolution, although such a performance is not available in current state-of-the-art low-cost wireless transceiver chips.

References

[1] J. Miranda, N. Makitalo, J. Garcia-Alonso, J. Berrocal, T. Mikkonen, C. Canal, and J. Murillo, “From the internet of things to the internet of people”, *Internet Computing, IEEE*, vol. 19, no. 2, pp. 40–47, Mar. 2015.

[2] T. Vilarinho, B. Farshchian, J. Floch, and B. Mathisen, “A communication framework for the internet of people and things based on the concept of activity feeds in social computing”, in *9th International Conference on Intelligent Environments (IE)*, Jul. 2013, pp. 1–8.

[3] J. Wei, “How wearables intersect with the cloud and the internet of things : considerations for the developers of wearables”, *Consumer Electronics Magazine, IEEE*, vol. 3, no. 3, pp. 53–56, Jul. 2014.

[4] G. Tsouri and J. Wilczewski, “Reliable symmetric key generation for body area networks using wireless physical layer security in the presence of an on-body eavesdropper”, in *Proceedings of the 4th International Symposium on Applied Sciences in Biomedical and Communication Technologies (ISABEL)*, Barcelona, Spain, 2011, 153:1–153:6.

[5] R. Mehmood, J. Wallace, and M. Jensen, “Key establishment employing reconfigurable antennas: Impact of antenna complexity”, *Wireless Communications, IEEE Transactions on*, vol. 13, no. 11, pp. 6300–6310, Nov. 2014.

[6] S. Premnath, S. Jana, J. Croft, P. Gowda, M. Clark, S. Kasera, N. Patwari, and S. Krishnamurthy, “Secret key extraction from wireless signal strength in real environments”, *Mobile Computing, IEEE Transactions on*, vol. 12, no. 5, pp. 917–930, May 2013.

[7] P. Vanveerdeghem, P. Van Torre, C. Stevens, J. Knockaert, and H. Rogier, “Synchronous wearable wireless body sensor network composed of autonomous textile nodes”, *Sensors*, vol. 14, no. 10, pp. 18 583–18 610, Oct. 2014.

[8] P. Van Torre, T Castel, and H. Rogier, “Encrypted body-to-body wireless sensor node employing channel-state-based key generation”, in *Submitted for EUCAP 2016*.

[9] C. J. Cellucci, A. M. Albano, and P. E. Rapp, “Statistical validation of mutual information calculations: Comparison of alternative numerical algorithms”, *Physical Review E*, vol. 71, no. 6, p. 066 208, 2005.

[10] S. N. Premnath, S. Jana, J. Croft, P. L. Gowda, M. Clark, S. K. Kasera, N. Patwari, and S. V. Krishnamurthy, “Secret key extraction from wireless signal strength in real environments”, *Mobile Computing, IEEE Transactions on*, vol. 12, no. 5, pp. 917–930, 2013.